

**Co-seismic and co-diking crustal deformation
along subaerial rift zones
detected by satellite synthetic aperture radar:
East Africa, Iceland, and Southwestern Japan**

(衛星 SAR によるリフト帯における地震時・ダイク貫入時の地殻変動観測：
東アフリカ，アイスランド，西南日本)

Yuji Himematsu

Submitted for the degree of Doctor of Philosophy

Department of Natural History Sciences,

Graduate School of Science,

Hokkaido University

March 2019



Contents

要旨	v
Abstract	vii
Acknowledgement	ix
List of Figures	xi
List of Table	xiv
Chapter 1. Introduction	1
1.1 Geodetic measurement for detecting Earth's surface movement	2
1.2 Objective of this thesis	6
1.3 Thesis roadmap	8
Chapter 2. Monitoring crustal deformation using synthetic aperture radar images	13
2.1 Synthetic Aperture Radar (SAR)	14
2.2 Monitoring surface movement using SAR images	18
2.2.1 Interferometric SAR (InSAR)	18
2.2.2 Pixel tracking	27
2.2.3 Time-series analysis	30
Chapter 3. Aseismic strike-slip along graben subsidence associated with the 2007 Natron dike intrusion episode, Tanzania	33
3.1 Introduction	34
3.2 Methods and results	37
3.3 Elastic source model	42

3.4 Discussion	46
Chapter 4. Along-rift horizontal displacement on graben subsidence during the 2005-2010 Afar dike intrusion episode detected by PALSAR-1 data	51
4.1 Introduction	52
4.2 SAR data and processing method	57
4.3 Fault source model	60
4.4 Discussion	64
4.4.1 Aseismic slip consistent with rate-and-state friction law	64
4.4.2 Any relevance to strike-slip earthquakes along divergent plate boundaries?	65
4.4.3 Block-like motion of graben floor as a response to horizontal flow of plume material?	65
Chapter 5. Icecap and crustal deformation associated with the 2014-2015 Bárðarbunga dike intrusion episode inferred from SAR pixel tracking	69
5.1 Introduction	70
5.2 SAR data and processing method	74
5.2.1 Processing method and SAR dataset	74
5.2.2 Observation result during pre- and co-diking period	78
5.2.3 Estimation of subglacial ground deformation	84
5.2.4 Temporal changes of icecap surface change	87
5.3 Elastic modeling	90
5.3.1 Model setting and geometry	90
5.3.2 Distribution of dike opening and fault slip	92
5.4 Discussion	100
5.5 Post-emplacment deformation of Holuhraun lava field	104
Chapter 6. Dynamic slip partitioning associated with the 2016 Kumamoto earthquake sequence, SW Japan	111
6.1 Introduction	112

6.2 Methods and results	114
6.3 Fault source model	119
6.4 Discussion	124
6.5 Post-seismic deformation revealed by PALSAR-2 data	127
Chapter 7. Thesis findings and conclusions	135
Bibliography	141
Appendix A. SAR Dataset in Chapter 5	153

要旨

プレート境界ではひずみが集中しやすいため、地震活動や火山噴火が活発であり、プレート境界における地殻変動は地震や火山噴火の発生メカニズムを解明するために重要な研究対象である。なかでもプレート拡大境界はリフト帯と呼ばれ、新たな地殻の形成や大陸分断の過程を観測できる地域として注目を集めている。しかし中央海嶺に代表されるようにリフト帯の多くは海底に位置しており、陸上では全体の2%以下しか観測できない。新たな地殻の形成や大陸分断の過程を観測できるリフト帯における地殻変動データの蓄積は、リフト帯における地球物理学的現象の解明にとって重要である。本論文では合成開口レーダ (Synthetic Aperture Radar: SAR) が観測した画像データに干渉 SAR (InSAR) と pixel tracking 法を適用することにより、リフト帯における地殻変動を観測した。全地球測位システム (Global Navigation Satellite System: GNSS) を用いた地殻変動観測とは異なり、衛星搭載型 SAR による画像撮像は観測機器を設置する必要はなく、一定間隔で陸域を全球的に撮像できる。また地殻変動のみならず氷河の流動や都市域の地盤沈下といったあらゆる地表変動を数 m の高い空間分解能で、面的に地表変動の描像を明らかにできる点も大きな特徴である。本論文ではリフト帯で発生した4件のイベントに対して適切な解析手法を適用し、これまで報告されていた観測データを質・量ともに凌駕する地殻変動データを用いて、観測結果を再現するモデルを提案し、それらの物理的解釈を提案する。本論文ではリフト帯で発生した3件のダイク貫入イベントと1件の地震イベントに注目した: 1) 2007年 Natron 湖ダイク貫入イベント (タンザニア), 2) 2005-2010年 Afar 盆地ダイク貫入イベント (エチオピア), 3) 2014-2015 Bárðarbunga 火山ダイク貫入イベント (アイスランド), 4) 2016年熊本地震 (西南日本).

東アフリカ地溝帯で発生した2件のダイク貫入イベント (2007年 Natron 湖ダイク貫入イベント, 2005-2010年 Afar 盆地ダイク貫入イベント) では PALSAR-1 データに InSAR とピクセルオフセット法を適用することにより、ダイク貫入に伴う地殻変動の描像を明らかにした。これらの観測結果はグラーベンの沈降領域において拡大軸と平行する方位に水平変位が生じていたことを明らかにした。両イベント時におけるメカニズム解はいずれも横ずれ成分をほぼ含まない正断層型を示しており、これらの走向は拡大軸の方位とおおむね一致していた。このグラーベンの沈降領域における水平変位の再現には正断層ずれに加えて横ずれ成分も必要であることを数値計算によるモデルが示した。したがってグラーベンの沈降領域における水平変位は非地震的に生じたことが示唆された。地質構造の発達やマントル対流と地殻との相互作用によって生じた可能性が考えられる。

アイスランド中東部に位置する Bárðarbunga 火山で発生したダイク貫入イベントは2014年8月に始まり、ダイク貫入に伴って発生した割れ目噴火は2015年2月まで続いた。先行研究による InSAR 解析データは氷帽上で非干渉領域となっており、イベントに伴

う氷帽下地殻変動の描像を明らかにできていなかった。震源分布から推定された本イベントのダイクの貫入経路の約 80%は氷帽下に位置しており、地殻変動データが十分に取得されたとは言い難い。また GNSS による観測も氷帽上では定常的な観測を行っていなかったため、ダイク貫入に伴う地殻変動の全容を把握することは困難であった。本論文では氷河の流動速度検出に採用される Pixel-tracking 法を COSMO-SkyMed と RADARSAT-2 データに適用することにより、ダイク貫入に伴う氷帽表面における変動の検出を試み、これらのデータを用いて氷帽下の地殻変動を推定した。Pixel tracking 法を適用した結果は非雪氷域のみならず、氷帽上においてダイク貫入のおよそ北半分の経路上で顕著な変動を示すシグナルを示した。また適切に重みをかけたイベント前のシグナルをイベント時のシグナルから差し引くことで氷帽下地殻変動の描像を推定した。補正したデータを使用して鉛直開口・断層運動を再現するモデルを推定したところ、非雪氷域のみの地殻変動データを用いてモデルを推定した場合と比較して疑似的な開口・すべり分布を示すことなく、より小さい不確定性をもったモデルを推定することができた。

2016 年熊本地震は南北の引張応力場にある九州地方の別府島原地溝帯で発生した。九州地方は中部九州の直下には地震波低速度領域が卓越しており continental rift であるとする説がある一方、別府島原地溝帯が南西から延びる沖縄トラフの東端と東から延びる中央構造線の西端に位置しており、南海トラフの前弧スリバーが南西進していることから pull apart basin であるという説もある。熊本地震に関して気象庁が示した本震のメカニズム解は南北方向に引張軸を持つ右横ずれ型地震であると同時に、顕著な非ダブルカップル成分も示した。国土地理院による InSAR 解析の速報は地表断層付近において非干渉領域となっており、地殻変動の描像を明らかにできていなかった。本章では PALSAR-2 データに pixel tracking 法を適用することにより、強健な地殻変動シグナルを検出して詳細な地殻変動の描像を明らかにした。それらのデータに基づいて断層モデルを提案して、非ダブルカップル成分との関連性を議論した。本震のメカニズム解は横ずれ成分が卓越していたものの、PALSAR-2 データによる pixel tracking の結果は右横ずれの水平変位に加えて 2m 以上の沈降を明らかにした。この地殻変動の複雑性はメカニズム解に含まれる非ダブルカップル成分に反映されている可能性が高く、観測された地殻変動の描像と推定した断層モデルのすべり分布は地震時における slip partitioning の形成を示唆している。また PALSAR-2 データによる干渉画像の重ね合わせにより明らかになった地震後地殻変動についても報告する。

Abstract

Crustal deformation along the plate boundaries is one of the important research interests for elucidating their mechanisms because earthquake activities and volcanic eruptions usually concentrate along plate boundaries due to high strain rates. Along the divergent plate boundaries which usually call rift zone, we can observe the processes of continental rifting evolution, such as generating new crust and splitting continental crust. Most of the divergent plate boundaries, however, are located beneath the sea, and the onshore rift zones are only less than 2 % of all the rift zones on the Earth.

The accumulation of crustal deformation data along the subaerial rift zones improves our understanding of the rift systems and the geophysical phenomena. The aim of this thesis is to reveal detailed crustal deformation along the subaerial rift zones by processing satellite SAR data, one of the space-based geodetic methods. SAR data can detect surface movement with high spatial resolution without installing on-site observation instruments, like GNSS receivers. This thesis focuses on three dike intrusion episodes and one earthquake event along the subaerial rift zones: 1) the 2007 Natron dike intrusion episode, Tanzania, 2) the 2005-2010 Afar dike intrusion episode, Ethiopia, 3) the 2014-2015 Bárðarbunga dike intrusion episode, Iceland, 4) the 2016 Kumamoto earthquake sequence, Japan.

By applying InSAR and pixel tracking approaches to PALSAR-1 data the horizontal displacements parallel to the rift axis on the graben subsidence were detected during the 2007 Natron and the 2005-2010 Afar dike intrusion episodes which occurred along the East African Rift. The focal mechanisms during each episode indicate normal faulting with few strike-slip components, these strikes nearly coincide with the rift axis direction. Our inversion model confirmed that the optimal elastic models need not only normal faulting but also strike-slip components to reproduce the horizontal displacement on the graben subsidence. Thus the along-rift horizontal displacements on the graben floor were implied to occur by aseismic processes.

The 2014-2015 Bardarbunga dike intrusion episode occurred along the subaerial divergent plate boundary between the Northern American and the Eurasian plates. The overall description of crustal deformation associated with the dike intrusion remains poorly revealed because 80% of dike path located beneath the Vatnajökull icecap which is the largest ice in Europe. Although the conventional InSAR method needs to avoid decorrelation problems for detecting signal above ices and/or glaciers, previous InSAR data could not reveal any signal at the icecap due to the decorrelation problems. In this thesis, we applied pixel tracking approach, which is suitable for detecting the velocity of glacier flow, to satellite SAR data to reveal icecap surface movement associated with the

subglacial dike intrusion. Because the co-diking signals contain the signal of both steady-state of icecap flow and crustal deformation, we corrected the icecap flow signal by subtracting the scaled pre-diking signal from the co-diking signal assuming that the pre-diking signals show only the steady-state of icecap flow signal. The ice-corrected signal implies the description of subglacial crustal deformation. We confirmed that the ice-corrected signal contributed to improve the dike opening/faulting model.

The 2016 Kumamoto earthquake sequence is the series of earthquake, including Mw 7.0 of mainshock, along the Beppu-Shimabara graben system in Kyushu, Japan. One of the characteristics of the event is that the sequence contains two foreshocks greater than Mw6.0 28 hours before the mainshock and four aftershocks greater than 5.5 one week after the mainshock. The focal mechanism of mainshock from the Japan Meteorological Agency shows not only the dominant of strike-slip components with N-S extensional axis but also ineligible non-double couple component. The newsletter from Geospatial Information Authority of Japan has reported that InSAR results indicate data lacking near the surface ruptures due to the decorrelation problems. In this thesis, we applied the cross-correlation-based pixel tracking approach to PALSAR-2 data to avoid the decorrelation problems. Although the focal mechanism of the mainshock dominates strike-slip component, our pixel tracking data indicates not only right-lateral displacement with NE-SW striking but also over 2 m of subsidence at the northern half of displacement field. The complexity of crustal deformation associated with the earthquake sequence can be explained by the non-double couple component in the focal mechanism of mainshock and the slip-partitioning.

Acknowledgement

This dissertation concludes five years of my graduate study at the Department of Natural History Sciences, Hokkaido University. I have received uncountable warm supports from many people and organizations for my graduate school life. First, I would like to show my hearty gratitude to my supervisor Professor Masato Furuya who encouraged and patiently advised me. He also gave me many opportunities to attend academic meetings and workshops for presentations of my research and discussions with many researchers. Professor Kosuke Heki and Professor Youichiro Takada provided inestimable possibilities of Geodesy through their interesting research. I'm always looking up to their positive attitudes with passions for exploring advance of geodetic approaches. I appreciate professors and researchers in the solid seminar for their constructive comments and discussions. Their comments always improve my knowledge and ambiguities in my presentations. Students in the seminar always encouraged me when I was struggling to advance my research. Also, I would like to express my gratitude to Professor Freysteinn Sigmundsson for accepting my proposal and approving my work in Iceland. He always warmly welcomed me to discuss and gave me interesting feedbacks for advancing our research. Discussion with researchers and students in the Institute of Earth Science, the University of Iceland, also contributed to promoting our research. The working in Iceland has been an irreplaceable experience in my life. I wish to thank the financial support from Japan Society for the Promotion of Science (JSPS) during my doctoral course. The Research Fellowship for Young Scientist maintained my living without part-time jobs, and the Overseas Challenge Program for Young Researchers supported my living in Iceland from November 2017 to March 2018. The Geodetic Society of Japan supported my travel grants for attending AGU meetings in US. Last but not least, I would like to thank all of the people who helped and supported me in the course of my graduate school life.

PALSAR-1 level 1.0 and PALSAR-2 level 1.1 data in this thesis are sharing among the PALSAR Interferometry Consortium to Study out Evolving Land surface (PIXEL), and provided by Japan Aerospace Exploration Agency (JAXA) under a cooperative research contract with the Earthquake Research Institute, University of Tokyo. The ownership of PALSAR-1 data belongs to both JAXA and the Ministry of Economy, Trade and Industry (METI). That of PALSAR-2 belongs to JAXA. COSMO-SkyMed, TerraSAR-X, RADARSAT-2 data in Chapter 5 are sharing among the FUTUREVOLC consortium (European Community's Seventh Framework Programme Grant No. 308377). COSMO-SkyMed and TerraSAR-X data in Chapter 5 are owned by the Italian Space Agency (ASI), the German Space Agency (DLR), both through the Icelandic Volcanoes Supersite project, supported by the Committee on Earth Observing Satellites (CEOS). RADARSAT-2 data were provided by the Canadian Space Agency and MDA Corporation. Sentinel-1A data in Chapter 5 is provided by the European Space Agency (ESA) at Copernicus Open Data Hub

(<https://scihub.copernicus.eu/>).

Focal mechanisms and hypocenters in Chapter 3, 4 are provided by the Global Centroid Moment Tensor Project database. These information of earthquake in Japan in Chapter 6 are provided by Japan Meteorological Agency (JMA). Some of figures are generated by commercial software MATLAB and the public domain Generic Mapping Tools (GMT).

List of Figures

Figure 1-1. World map with tectonic lines and seismicity, and enlarged maps of study areas in this thesis.	9
Figure 2-1. An example of the range split-band spectrum method for PALSAR-2 dataset.	25
Figure 2-2. Azimuth offset and MAI data which are derived from same PALSAR-2 dataset in Figure 2-1.	26
Figure 3-1. Study area in Chapter 3.	35
Figure 3-2. Subsampled PALSAR-1 InSAR data which show co-diking displacement associated with the 2007 Natron dike intrusion episode.	37
Figure 3-3. Observation and calculation of azimuth offset for ascending orbit.	38
Figure 3-4. Surface projection and 3D description of our optimal elastic model.	39
Figure 3-5. Co-diking 3D displacement inferred from PALSAT-1 InSAR and pixel-tracking data.	41
Figure 3-6. Inferred our optimal faulting and opening distributions.	43
Figure 3-7. Coulomb stress changes due to dike opening for each receiver fault.	44
Figure 4-1. Study area in Chapter 4.	53
Figure 4-2. Temporal evolution of PALSAR -1 pixel-tracking data from 2007 to 2010 associated with the dike intrusion sequence in Afar.	56
Figure 4-3. Cumulative PALSAR-1 pixel-tracking and MAI data from 21 May 2007 to 5 August 2010.	58
Figure 4-4. Temporal evolution of cumulative azimuth offset and its cross-sections.	60
Figure 4-5. Our optimal elastic model for the PALSAR-1 pixel-tracking data.	62
Figure 4-6. Standard deviations of faulting and opening distributions.	63
Figure 4-7. Coulomb stress changes due to dike opening in our model for each receiver fault.	64
Figure 4-8. Cross section of topographic height and cumulative azimuth offset from 12 June 2007 to 5 August 2010 along the profile C-C' in Figure 4-2.	66
Figure 5-1. Study area in Chapter 5.	71
Figure 5-2. Pre- and co-diking Cosmo-SkyMed (CSK) pixel tracking results and ice-corrected signals.	77

Figure 5-3.	Pre-diking and co-diking 3D displacements inferred from CSK data.	79
Figure 5-4.	Stacked TerraSAR-X (TSX) pixel-tracking and co-diking 3D displacement inferred from CSK and TSX dataset.	80
Figure 5-5.	Enlarged 3D displacement inferred from CSK and TSX dataset and cross-section across and along the graben subsidence.	82
Figure 5-6.	RADARSAT-2 (RS2) pixel tracking results during pre- and co-rifting period and ice-corrected signal.	85
Figure 5-7.	Cross sections of descending Cosmo-SkyMed (CSK) range offset during the co-diking signal (grey dots) and ice-corrected signal (blue dots).	86
Figure 5-8.	Profiles of RADARSAT-2 (RS2) range and azimuth offset in Track 81 during the co-diking signal (grey dots) and ice-corrected signal (red dots).	87
Figure 5-9.	Time-series of vertical component of line-of-sight (LOS) change on the icecap from June 2014 to January 2017.	89
Figure 5-10.	Our optimal elastic model and the model geometry.	95
Figure 5-11.	Comparison of observations, calculations derived from our model, and residuals.	96
Figure 5-12.	Dike opening and normal faulting distributions inferred from the observations which are masked above the icecap and its standard deviations.	98
Figure 5-13.	A PALSAR-2 interferogram across the Bárðarbunga caldera.	102
Figure 5-14.	CSK pixel-tracking data observed from ascending track across the Bárðarbunga caldera.	103
Figure 5-15.	CSK pixel-tracking data observed from descending track across the Bárðarbunga caldera.	103
Figure 5-16.	Lava field subsidence derived from stacked PALSAR-2 InSAR and pixel tracking.	108
Figure 5-17.	Range offset between 24 November 2014 and 2 February 2015.	109
Figure 6-1.	Study area in Chapter 6.	113
Figure 6-2.	PALSAR-2 pixel-tracking data which shows co-seismic displacement.	116
Figure 6-3.	Cumulative 3D displacement inferred from our pixel-tracking data of tracks 23 and 130.	117
Figure 6-4.	Comparison of cumulative 3D displacements inferred from three combination of PALSAR-2 pixel-tracking data.	118
Figure 6-5.	Schematic perspective of fault geometry of our inferred model viewing from NNE.	120
Figure 6-6.	Comparison with observation of pixel-tracking data, calculation derived from our slip distribution and their residual.	122

Figure 6-7. Slip distributions on each fault segment viewing from WNW.	123
Figure 6-8. Slip 1-sigma uncertainties for each segment calculated by 200-times iteration of inversion with random noise.	124
Figure 6-9. Focal mechanisms of the mainshock derived from JMA catalog, and that derived from the inferred slip distribution.	127
Figure 6-10. PALSAR-2 footprints for detecting post-seismic crustal deformation.	131
Figure 6-11. Stacked PALSAR-2 InSAR following the mainshock.	133
Figure 6-12. Cumulative post-seismic quasi-displacements inferred from the stacked PALSAR-2 InSAR.	134

List of Table

Table 3-1. ALOS-1/PALSAR-1 dataset in Chapter 3.	36
Table 4-1. Timing and volume of intruded magma during the 2005-2010 Afar dike intrusion sequence.	54
Table 4-2. PALSAR-1 dataset in this Chapter 4.	55
Table 5-1. Satellite SAR dataset in Chapter 5 and scale factors for correction of icecap signal.	76
Table 5-2. Dataset for inferring elastic model.	99
Table 5-3. PALSAR-2 dataset for detecting the post-emplacement deformation.	107
Table 6-1. PALSAR-2 dataset in Chapter 6.	115
Table 6-2. Parameters of our fault model.	121
Table 6-3. Total moment release derived from the inferred fault model (GM) and JMA catalog (SM).	125
Table 6-4. PALSAR-2 dataset for the post-seismic deformation.	129

Chapter 1

Introduction

Chapter 1. Introduction

1.1 Geodetic measurement for detecting Earth's surface movement

Geodesy is a study for measuring the Earth's shape, rotation, and orientation and these spatiotemporal variations. Geodesy has also been contributing to observing crustal deformation associated with earthquakes, volcanic activities, and other geophysical phenomena. Since the late 1900's, satellite geodetic techniques have contributed to improvements in measurement accuracy and spatiotemporal resolution for monitoring surface movement on the Earth. Satellite geodetic techniques can observe ground movement with high precision continuously or regularly. For volcano, long-term continuous observations contribute to the understanding of the mechanisms of volcanic eruptions because precursors (such as inflations of the magma chamber due to charging magma) usually initiate from a few hours to several years before the eruption.

Space-based geodetic techniques are utilized for detecting various scale of surface movement above the Earth including plate motion and crustal deformation associated with earthquakes. Detecting plate motion allows the understanding of the process of dynamic plate tectonics and to sustain the geospatial reference. Observations of geomagnetic reversal at seafloors and the similarity of coastline between two continents can provide evidence of plate tectonics. Additionally, a space-based geodetic technique known as very long baseline interferometry (VLBI) has detected variations in the spatial baseline between two sites. This is direct evidence for plate tectonics. Regarding crustal deformation, measuring ground displacement due to earthquakes and volcanic activities contributes to our understandings the mechanism of each physical process. In the case of modeling observed ground deformation due to earthquakes, an analytical solution is usually employed for the ground deformation associated with rectangular dislocations in uniform elastic half-space proposed by Okada (1985, 1992).

This analytical solution has been mostly utilized to infer a fault source model for computing distributions of slip (and tensile opening) by solving inversion problems (e.g., Jonsson et al., 2002; Wright et al., 2003). For crustal deformation due to volcanic activities, analytical solutions for approximating ground deformation have been reported using a point source (e.g., Mogi, 1958), an ellipsoidal source (e.g., Yang et al., 1988), a tensile dislocation (e.g., Okada, 1985), and a penny-shaped source (e.g., Fialko, 2001). Sometimes multiple sources are used to fit the observational data because ground displacements due to volcanic activities cannot be completely explained using a simple source (e.g., Fialko and Simons, 2000). These analytical solutions can also be used to infer the volume of magma intrusion/extrusion, and the volume change due to inflation/deflation of the magma chamber.

Various satellite geodetic techniques have contributed to the accumulation of observations of the Earth's surface movement including VLBI, and the Global Navigation Satellite System (GNSS). VLBI can observe relative plate motion between two observation sites (e.g., Christodoulidis et al., 1985). VLBI can also determine the location of observation sites with an accuracy of a few millimeters (Schuh and Behrend, 2012). VLBI can infer the distance between each telescope by measuring the arrival time difference of signals from the Quasi-Stellar object (an object emitting electromagnetic waves). VLBI has detected baseline shortening of 7-9 cm/yr between the Kashima station and Kawai station, suggesting that the Pacific plate is drifting eastward (Heki et al., 1987). VLBI is not only for observing relative plate motion but also for observing the fluctuation of Earth's rotation axis (precession and nutation), and for determining the location of extragalactic objects in inertial space. VLBI can determine the Earth Orientation Parameters (EOPs) by observing the Earth's rotation axis movement.

GNSS is the most famous geodetic observation system for positioning. A well-known example of a GNSS constellation is the Global Positioning System (GPS) operated by the US army and consisting of 24 satellites orbiting above 20,000 km in altitude. Some countries have launched GNSS network of their own to improve the measurement accuracy for their regions. For example, Beidou in China, Galileo in the European Union (EU), and Quasi-Zenith Satellite System (QZSS) in Japan. Improving measurement accuracy by increasing the number of GNSS satellites is expected to help realize developments of automatic transportation systems, such as a self-driving car. In Japan, the Geospatial Information Authority of Japan (GSI) installs and maintains a dense GNSS network across Japan with 1300 observation sites and called the GNSS Earth Observation Network System (GEONET). GEONET contributed to revealing a wide-region of co-seismic crustal deformation moving toward the Japan trench due to the 2011 Tohoku-oki earthquake (e.g., Nishimura et al., 2011). GNSS observation data sometimes includes artifacts induced by the delay of the microwave signal arrival time and ionospheric disturbances. However, the ionospheric artifacts can be corrected because GNSS measurement employs a dual frequency of L-band microwave. The correction of ionospheric artifacts can describe the distribution of total electron content (TEC). Calais and Minster (1995) have reported that the first detection of travelling ionospheric disturbance (TID) due to propagating acoustic waves excited by surface uplifts due to the 1997 Northridge earthquake, California. GNSS measurement detected a positive TEC anomaly less than 1 hour before the mega-earthquakes (e.g., Heki, 2011). Although a temporal resolution of ionosonde observation is 15 minutes, the ionosonde observation and a geomagnetic declination also simultaneously varied as well as the GNSS observation (e.g., Heki and Enomoto, 2013).

VLBI and GNSS networks are utilized to measure crustal deformation and relative plate motion. They are also used to maintain the International Terrestrial Reference Frame (ITRF) for

precise positioning. ITRF has been renewed regularly with the accumulation of past datasets. ITRF 2014 is the most up to date version (Altamimi et al., 2016). The datasets of the Satellite Laser Ranging (SLR) and Doppler Orbitography and Radio-positioning Integrated by Satellite (DORIS) are also employed for the maintenance of ITRF.

For measuring crustal deformation using VLBI or GNSS (or other geodetic methods, such as leveling surveys), the instruments must be installed at the observation sites before the deformation events. Installing measurement instrumentation is expensive. To observe crustal deformation automatically, power generators (e.g., solar photovoltaic) are required to perform observations. Instrument maintenance and data collection (which is recorded on loggers) are required at regular intervals. Measuring crustal deformation associated with volcanic activities is dangerous due to the risk of sudden eruptions during the installation of instrumentation. Observing crustal deformations in the field requires money, time, and manpower for data collection. In contrast, synthetic aperture radar (SAR) can observe crustal deformations without installing observation instruments in the region of interest. Although optical images cannot identify surface conditions at night or when obscured by clouds, SAR images can always reveal surface characteristics such as back-scatter intensity because SAR sensors employ microwaves. Generally, either payment or a relevant research proposal is required to obtain SAR data. However, SAR data recorded by Sentinel-1 (operated by the European Space Agency (ESA)) is currently available at no cost via ESA website (<https://sentinel1.esa.int/>). SAR sensors onboard satellites can acquire data regularly because satellites orbit Earth at an interval of the designated period. COSMO-SkyMed (operated by the Italian Space Agency (ASI)) is a constellation of SAR satellites and provides a minimum of one day of temporal resolution. A single Sentinel-1 satellite acquires data at an interval of 12 days. Data accumulation reveals long-term small displacements as well as GNSS measurements. GNSS measurement provides higher temporal resolution. It is not necessary to install

any instruments for observations. Spatial resolution of SAR observations are a few meters at a minimum. However, the spatial resolution depends on image acquisition modes and scale factors of spatial filters used for mitigating noise. In summary, employing SAR data for observations can circumvent various issues associated with non-satellite based geodetic methods. SAR principles and analysis methods are described in Chapter 2.

1.2 Objective of this thesis

This thesis focuses on crustal deformations associated with dike intrusions and earthquake episodes along subaerial rift zones. Generally, most rift zone are subject to an extensional stress regime. Such stress regimes are usually driven by upwelling mantle plume, negative buoyancy, and tectonic stress. Processes of splitting continental crust and new crust formation along continental rifts (like the East African rift and Iceland) can be observed due to the upwelling materials of the upper mantle. Subducting slab induces negative buoyancy of crust and contribute to forming back-arc basins (such as the Ryukyu and Mariana troughs). A pull apart basin can be formed at a junction of rift and lateral fault termination (such as with Kyushu island in SW Japan and the Dead Sea basin). Formations of rift zones are induced by various geophysical factors. The majority of rift zones are located on the seafloor (only 2% of all rift zones on land). Hence, subaerial rift zones are important interest for elucidating processes of splitting crust or rift evolutions.

Even if convergence plate boundaries are located far from the metropolitan area, mega-earthquakes usually generate strong shaking and sometimes tsunamis if subduction zones are beneath the sea. Strong shaking generated by an earthquake and occurring at a deeper brittle part of the Earth's crust propagates over wide range, destroying buildings and inducing secondary disasters. A tsunami is a destructive water wave induced by mega-earthquakes, and usually wipe out physical objects on land.

That is why various observation instruments are installed offshore along subduction zones such as the trench around Japan, Cascade in US, and Chile. In contrast, the scales of earthquakes along rift zones are moderate compared to subduction zones in which earthquakes of magnitude greater than 8 occur. Because the thickness of the brittle part is relatively small, large scale earthquakes cannot physically occur along rift zones (mega-earthquakes occur only along convergence plate boundaries). The range of destruction is relatively limited for earthquakes along rift zones because they involve a shallower part of the Earth's crust. Hence, rift zone earthquakes have a lower priority in terms of research associated with disaster prevention and human society. However, the accumulation of observational data on rift zones is expected to contribute to improvement in our understanding of plate tectonics and the dynamics of the crust and mantle. Using satellite SAR data, crustal deformation can be observed along remote subaerial rift zones without the need for surface access.

Although moderate-scaled earthquakes have occurred along rift zones, the scale of crustal deformation is sometimes beyond one meter despite the scale of earthquake. In such cases, the earthquake may have a relationship with magma within the crust because it is easy to transport magma along weak lineaments from the magma source. Because the weak lineaments are formed in the direction of the rift axis, the strike of lateral magma propagation would also be consistent with the rift axis. The propagated magma is usually referred to as a dike and an episode sequence related to dike intrusions would be a dike intrusion episode. Dike intrusions are supposedly a preliminary stage of rift evolution and they induce meter-scale crustal deformation, which can be described through formations of graben structure.

One of the objectives of this dissertation is to determine appropriate SAR analysis methods for revealing crustal deformations (with limited data) due to dike intrusion and earthquake episodes

along rift zones. Identifying crustal deformation with large displacement gradient in interferograms (such as displacement near surface ruptures) is challenging because dense fringes sometimes cause phase unwrapping errors. However, interferometric SAR (InSAR) can detect surface movements with high measurement accuracy. Crustal deformations with large displacement gradients which usually appear near fault are expected to reveal important information concerning the deformation source. Xu et al. (2016) investigated a synthetic inversion test of how the limited input data near deformation source contributes to retrieval of the original deformation map. The synthetic test result also confirmed that the re-inferred slip distribution indicates both slip deficits at the shallowest part of fault segment and artificial overestimated slip at the slightly deeper part of segment when the input data were masked by a wider region of data across the center of the deformation field. Therefore, reducing missing data is expected to contribute to providing information on displacement fields and inferring elastic models precisely.

1.3 Thesis roadmap

This thesis consists of four main topics. Study areas are shown in Figure 1-1. All topics focus on crustal deformations due to dike intrusions and earthquakes along rifts observed from satellite SAR data.

The thesis outline is as follows:

Chapter 2 introduces the principal of SAR observation and SAR processing approaches to monitor surface movement across SAR images.

Chapter 3 focuses on the crustal deformation associated with the 2007 Natron dike intrusion episode in Tanzania. A 3D displacement inferred from PALSAR-1 InSAR and pixel-tracking data showed non-negligible southward displacement at the graben subsidence, despite the direction of the rift axis around Lake Natron being NNE-SSW. The optimal elastic model used here required the strike-

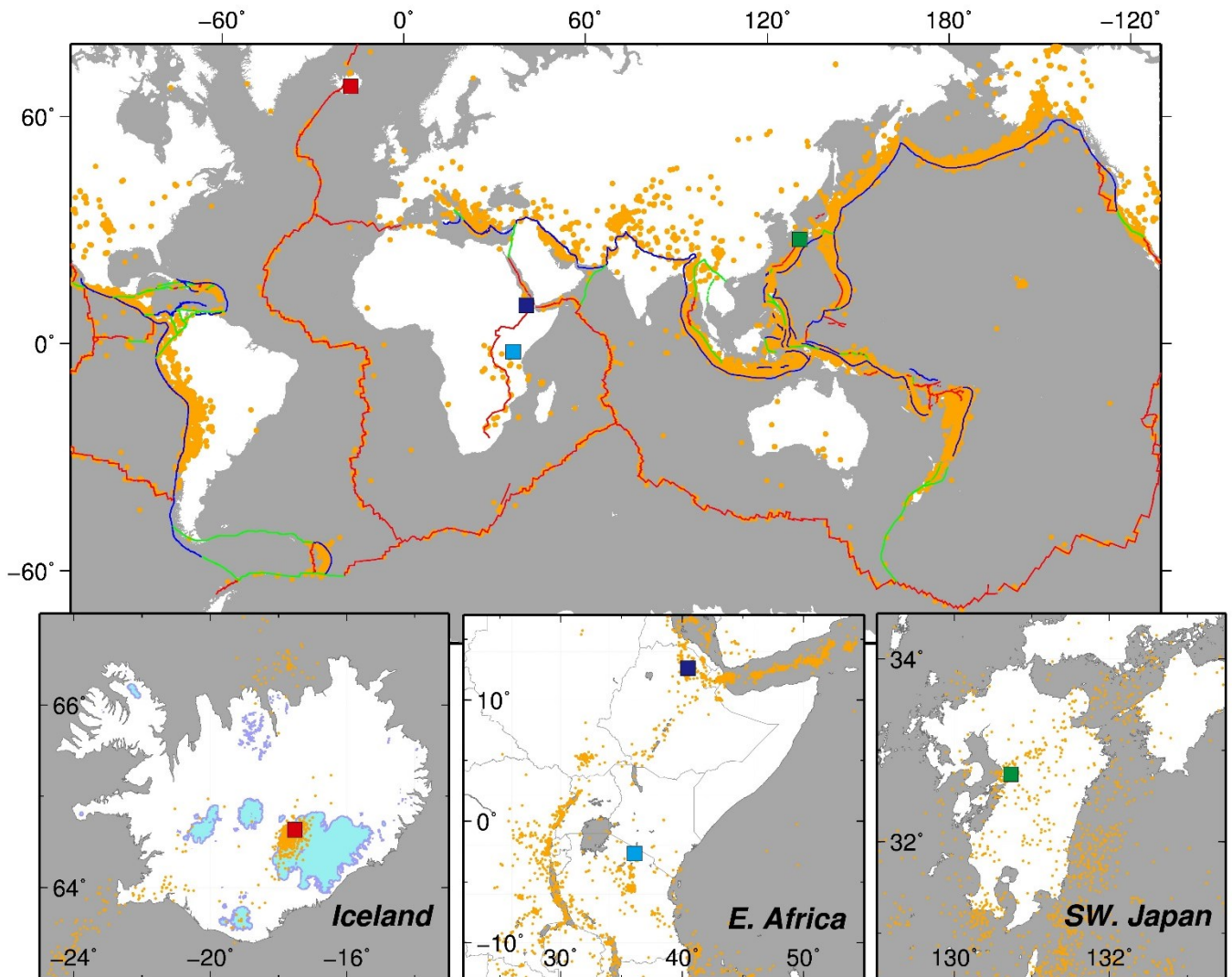


Figure 1-1. World map with tectonic lines and seismicity, and enlarged maps of study areas in this thesis. Red, blue and green lines indicate divergent, convergent, and transform plate boundaries from Peter (2003) and Coffin et al., (1998). Orange dots are the seismicity of $M>3$ during January-August 2018. Red, dark blue, light blue and green rectangles are the location of Bárðarbunga volcano, Afar basin and Lake Natron, and Kumamoto city, respectively.

slip components to reproduce the along-rift displacements at the graben subsidence. Because focal mechanisms during the episode indicated few strike-slip components, the strike-slips along the graben-bounding faults occurred aseismically.

Chapter 4 focuses on the crustal deformation associated with the 2005-2010 dike intrusion sequence in Afar, Ethiopia. PALSAR-1 pixel-tracking data derived from only ascending track during 2007-2010 detected signal of horizontal displacement at the northern half of graben subsidence. The horizontal displacement signals revealed the along-rift horizontal displacement at the graben subsidence as well as the 2007 Natron dike intrusion episode. In this case, the optimal elastic model also requires strike-slip components to reproduce the signal of horizontal displacement at the graben subsidence.

Chapter 5 focuses on the crustal deformation associated with the 2014 dike intrusion episode at the Bárðarbunga volcanic system in Iceland. Most of the dike propagation paths are located beneath the icecap. Although previous InSAR data revealed crustal deformation only in the ice-free region, the Cosmo-SkyMed and RADARSAT-2 pixel-tracking data obtained a line-shaped subsidence signal above the icecap. This implied subglacial graben formation due to subglacial dike intrusion. Using these pixel-tracking data, the subglacial crustal deformation was inferred by subtracting the scaled pre-diking signal from the co-diking signal with the assumption that the pre-diking signals contains only the signal of the steady-state of icecap flow. This chapter also describes an experiment to determine whether the inferred subglacial crustal deformation contribute to improvement of the dike opening/faulting elastic model.

Chapter 6 focuses on the crustal deformation associated with the 2016 Kumamoto earthquake sequence in Japan. The episode contains two foreshocks and a following mainshock (Mw 7.0) 28 hours after the first foreshock. The epicentral region was located along the Beppu-Shimabara graben system, which is an extension stress regime across the central Kyushu island. The Japan Meteorological Agency (JMA) reported that focal mechanisms during the episode dominated strike-

slip components with ENE-WSW striking. However PALSAR-2 pixel-tracking data revealed significant subsidence of 2 m. This chapter presents the fault source model inferred from the geodetic data and discusses the relationship between the non-double couple components in the focal mechanisms of the mainshock and significant subsidence.

Chapter 7 presents the overall findings of the research and the conclusions of this thesis.

Chapter 2

Monitoring Crustal Deformation Using Synthetic Aperture Radar Image

Chapter 2. Monitoring crustal deformation using synthetic aperture radar images

2.1 Synthetic Aperture Radar (SAR)

SAR is an active sensor to observe information regarding back-scatter intensity and phase of the emitted microwave from scatterer on the ground. SAR sensors are usually onboard airplanes or satellites. Importantly, observation instruments for acquiring data (such as GNSS measurements) do not have to be installed. SAR data is described by complex numbers (i.e., a pixel contains real and imaginary parts.) The real part shows the distribution of the backscatter intensity, indicating ground characteristics. A white color indicates strong back-scatter intensity and is observed for rough ground conditions such as buildings. Black color indicates low back-scatter intensity as observed for smooth ground conditions including airport runways and water surfaces. Change of back-scatter intensity between consecutive SAR image acquisitions contributes to the detection of flooded region due to heavy rain and/or a tsunami. SAR images usually contain some geometric image modulations due to the variation of microwave incident angles, causing, shadowing, layover, and foreshortening. Because of the geometric modulation, mountains in SAR images appear to skew toward a near-range direction. On the other hand, the imaginary part of SAR data indicates the phase data of the microwaves. Although these look like random noise, the phase data is utilized to detect surface movements across the image (see Chapter 2.3.1). Information on microwave and polarization directions also contributes to identifying characteristics of the ground condition. An RGB composition image can also be characterized by assigned coloring to each polarization to represent artificial buildings, cultivations, and forests etc.

Japan Aerospace Exploration Agency (JAXA) have launched three SAR satellites at the time

of writing this thesis. These satellites have contributed to the observation of crustal deformation and also provided an overview of the damage caused by natural disasters in Japan. The first Japanese SAR satellite was the Japanese Earth Resources Satellite-1 (JERS-1, Japanese nickname of Fuyo-1), and was operational from 1992 to 1998. It was used to observe the crustal deformation due to the 1995 Kobe earthquake in Japan (e.g., Ozawa et al., 1997). The second Japanese SAR satellite was the Phased Array type L-band Synthetic Aperture Radar (PALSAR, Japanese nickname of Daichi), and was operational from 2004 to 2011. It was used to observe the crustal deformation associated with the 2008 Sichuan earthquake in China and the 2008 Iwate-Miyagi inland earthquake in Japan (Kobayashi et al., 2009; Takada et al., 2009). At the time of writing, the latest Japanese SAR satellite is PALSAR-2, which has been operational since 2014. These Japanese SAR satellites employ L-band microwave (1.25 GHz, wavelength of 23.6 cm) to acquire images. The advanced Satellite with New system Architecture for Observation 2 (ASNARO-2) is another Japanese small X-band SAR satellite which was launched and is operating by the NEC corporation in collaboration with the Ministry of Education, Culture, Sports, Science and Technology (MEXT).

SAR data is employed to monitor hard to access ground characteristics including glaciers, deforestation in tropical rainforests, and unidentified ships floating out at the sea etc. For example, the JICA-JAXA Forest Early Warning System in the Tropics (JJ-FAST) monitors tropical rainforest using ALOS-2/PALSAR-2, which is one of the satellite SAR sensors operated by JAXA. The system provides information of on-going illegal deforestation to governments in the 77 countries in the tropics using SAR data (<http://www.eorc.jaxa.jp/jjfast/>).

SAR sensors usually employ three-types of microwave frequency to acquire images: X-band, C-band, and L-band. Shorter wavelength microwave (X-band) is adopted by the COSMO-SkyMed

and the TerraSAR-X satellites which are operated by ASI and the German Aerospace Center (DLR), respectively. COSMO-SkyMed consists of a four-satellite constellation. The TerraSAR-X was the first commercial SAR satellite and produced a high-spatial resolution digital elevation model (DEM) of the world in conjunction with Tandem-X satellite data. European SAR satellites operated by ESA (such as ERS-1/2, ENVISAT/ASAR and Sentinel-1A/B) have utilized C-band microwaves for image acquisitions. The sensors on Japanese SAR satellites such as PALSAR-1/2 employ L-band microwaves. Differences in radar wavelengths cause variations in the sensitivities of back-scatter intensities from the ground. Shorter wavelength microwaves are reflected by the leaves on trees. In contrast, longer wavelength microwaves can pass through dense foliage and branch of trees are planted. The difference in radar wavelengths causes variations in the characteristics of backscatter intensity for vegetation and non-vegetation regions. Decorrelation problems are induced by the variation of vegetation on the ground when ground movements are measured using the interferometric SAR approach discussed below. Rignot et al. (2001) also reported that difference in the radar wavelength causes variations in the penetration depth into ice and/or glaciers. Variation of microwave penetration depth can reveal physical properties of ice, such as characterizing wet or dry ice.

A primary advantage of SAR sensors is that they can acquire data-rich images even at night or when it is cloudy. Because passive sensors (such as optical satellites) require sunlight to acquire images, ground features cannot be determined during overcast period. Image acquisition is also not possible during the winter in the polar region due to the polar night. In contrast, the SAR sensor radiates microwaves towards the ground then receives reflected microwaves when they are reflected from the scatterer repeatedly. SAR images can reveal the ground surface and the caldera surface even if volcanic gases (with dust and tephra) have been pluming. Therefore, SAR data can be acquired without being influenced by the weather or day/night.

SAR data consists of monochrome images with high spatial resolution. A data acquisition mode with super high spatial resolution can distinguish between different aircraft models on an airport runway. Various technique can be applied to realize the high spatial resolution of SAR images. Pulse compression is one of the image processing techniques used to improve the spatial resolution in the range direction R_r . R_r strongly depends on the bandwidth B_w . Shortening pulse width is one of the strategies used to improve R_r . However, the shortening pulse width requires significant electricity to not degrade the signal-to-noise ratio. Electricity supply is limited onboard satellites and airplanes. Instead of shortening pulse width, the pulse compression technique is usually employed to improve R_r . Modulating microwave frequency allows a shorter pulse width while maintaining signal-to-noise ratio (SNR) using the matched filter. The improved spatial resolution can be described as follows:

$$R_r = \frac{c}{2B_w \sin \varphi} \quad (2.1)$$

where c represents the speed of light in a vacuum, and φ the incidence angle of the illuminating microwave.

For the azimuth direction, the synthetic aperture technique enables improvement of the spatial resolution for the azimuth direction R_a compared with real aperture radar images. To identify two-point scatterers located along the azimuth direction, the distance between two scatterers must be longer than beam width. The beam pattern can be described using the sinc function. The beam width asvdefined by the 3 dB width $W_{3\text{ dB}}$ can be expressed as;

$$W_{3\text{ dB}} = \frac{\lambda R}{D} \quad (2.2)$$

where λ is microwave wavelength, R is distance for slant range direction, and D is length of antenna. If the parameters of ALOS-2/PALSAR-2 are applied, the spatial resolution for azimuth

direction would be ~15 km ($\lambda = 0.236$ m, $R = 628$ km, $D = 10$ m). Clearly, the spatial resolution is not suitable for observing details of surface characteristics. To improve the spatial resolution of images, the doppler phase shift must be considered. Because the analysis assumes that the long antenna is synthesized along the azimuth direction, the improved spatial resolution can be re-described as half of the antenna length L .

$$R_a = \frac{L}{2} \quad (2.3)$$

Theoretically, the shorter the antenna length is, the finer the spatial resolution is. However, shorter antenna length causes low SNR because of small microwave gain.

In addition to observing the surface of the Earth, SAR sensors are utilized for exploration of Venus whose surface is covered with thick carbon dioxide clouds. A SAR sensor was onboarding the Magellan spacecraft which observed the surface of Venus by taking advantage of the ability of microwaves to penetrate cloud. SAR images are mainly observed from satellites and aircrafts. However, SAR images are also acquired using ground instruments which is referred to ground-based SAR (GB-SAR) (e.g., Tarchi et al., 1999). GB-SAR enables measurements with high spatial resolution and high temporal resolution for specific observation target, such as volcanoes and landslides (e.g., Antonello et al., 2004; Intrieri et al., 2013).

2.2 Monitoring surface movement using SAR images

2.2.1 Interferometric SAR (InSAR)

SAR is a powerful strong tool for detecting surface movement associated with earthquakes, volcanic activity, glacier flow, and landslides. The most well-known SAR processing method for detecting surface movement is InSAR. InSAR can detect surface movement within an accuracy of a few centimeters using the phase data within SAR images. InSAR data is sensitive to the displacement

projected to the line-of-sight (LOS) direction, which is the direction between the satellite and ground. LOS lengthening indicates subsidence or horizontal movement away from the satellite, LOS shortening indicates uplift or horizontal movement towards the satellite.

An initial interferogram includes information on surface movement, topographic height, observation geometries, and other noise. To identify surface movement, the fringes derived from topographic height and the orbital baseline must be corrected. Additionally, noise due to atmospheric delay, ionospheric disturbance, and systematic sources must be reduced. Topographic fringes were subtracted from simulated fringes which were estimated using a digital elevation model (DEM). For example, using 3-arcsec Shuttle Radar Topography Mission (SRTM) data (Farr et al., 2007). Conversely, DEM maps can be generated using SAR data in short temporal baselines while assuming no surface deformation between the image acquisition interval. Orbital fringes derived from satellite observation geometries can be removed using precise orbital information provided by the relevant space agency. The larger the baseline between the first and second observation positions, the higher the density of the orbital fringes are. It is theoretically impossible to correct dense orbital fringes whose wavelength is beyond the spatial resolution per pixel (i.e., the critical baseline).

Initial phase difference is wrapped between $-\pi$ to $+\pi$, which means that the value is shown as modulo 2π . Thus the wrapped phase must be unwrapped in two dimensions to identify the cumulative phase difference from a reference point using certain algorithms, such as, the minimum cost flow or the brunch-cut algorithm (phase unwrapping). However, it is hard to connect spatial fringes where large movement occurs. If the wavelength of displacement fringes is larger than the pixel spacing of the SAR images, the absolute phase difference cannot be identified.

Fringes in interferograms show surface movements along a LOS direction. The interval of interferogram fringes coincides with a half of the radar wavelength for image acquisitions. This indicates that one cycle of fringe generated by L-band microwave show 11.8 cm of surface movement along a LOS direction. Fringes in interferograms become dense if SAR data acquired by shorter wavelength microwaves is used to measure ground deformations due to an event. Therefore, it is hard to identify surface movements with high displacement gradients using interferograms generated by shorter wavelength microwaves. Dense fringes sometimes cause phase unwrapping errors if the gradients of the surface movements per pixel are beyond one cycle of the radar wavelength. The limit of detectable displacement gradient can be described as

$$d = \frac{\lambda}{2D} \quad (2.4)$$

where d is the limit of detectable displacement gradient, λ is the radar wavelength, and D is the spatial resolution of the SAR images (Massonnet & Feigl, 1998).

The artificial phase anomaly is an issue in InSAR data because of the fluctuation of TEC in the ionosphere and water vapor content in the troposphere. These factors of artificial phase error are derived from the variation of refractive index in the medium. The variation of refractive index changes the propagation speed of the microwave. The theoretical propagation speed of microwave is described as

$$v = \frac{c}{n} \quad (2.5)$$

where c is the speed of light in a vacuum (299,792,458 [m/s]), n is the refractive index, and v is the speed of microwave. The artificial phase anomaly must be corrected as it can lead to misinterpretation the actual signal in the InSAR data.

Strong artifacts due to a variation of electron content in the ionosphere (50-200 km altitude) usually contaminate InSAR data. Because traveling ionospheric disturbance (TID) is driven by gravity waves, the ionospheric artifacts appear in a wider region across the InSAR data, such as an azimuth streak (Meyer et al., 2006). The effect of electron fluctuation in the ionosphere depends on the microwave frequency because the ionosphere is a dispersive medium. In contrast, the effect of surface movement, topography and tropospheric noise appeared in the non-dispersive phase difference in the InSAR data.

The first order-term of ionospheric delay Δr_{iono} can be described as

$$\Delta r_{iono} = \frac{K}{f_0^2} \Delta TEC \quad (2.6)$$

where $K = 40.31 \text{ [m}^3/\text{s}^2\text{]}$ is a constant, f_0 is the carrier center frequency of SAR data acquisition, and ΔTEC is the relative TEC along the LOS between two SAR images. L-band images (wavelength: 23.6 cm) and 16-times more sensitive to C-band images (wavelength: 5.6 cm). In other words, L-band images are superior for observing ionospheric phenomena (Maeda et al., 2016). InSAR measurements can be used to determine dynamics of ionospheric phenomena with high-spatial resolution. For example, Maeda et al. (2016) was the first to report first imaging of the small-scale horizontal structure of midlatitude sporadic E (Es) patches using ALOS/PALSAR images. Although GNSS TEC measurement only revealed frontal structure of Es patches (Maeda & Heki, 2014), InSAR phase difference showed small-scale disc-shaped patches within the frontal structure.

One of the most robust approaches for correcting ionospheric artifacts in interferograms is a range split-spectrum method (Brcic et al., 2010; Furuya et al., 2017; Gomba et al., 2016; Rosen et al., 2010). The original idea is equivalent to GNSS-TEC observation in which GNSS observations can be corrected using two carrier microwave frequencies (e.g., Tsugawa et al., 2004). Similar to the

GNSS-TEC observation, the split-spectrum method can distinguish between dispersive and non-dispersive components using low- and high-frequency SAR images. This method is particularly suitable for correcting ionospheric noise in InSAR data observed by recent SAR sensors (e.g., PALSAR-2) because these sensors employ wide bandwidths for improving image spatial resolution for range direction. An example of the application of the split-spectrum method is described by Gomba et al, (2016) The measurement accuracy of sub-band interferograms becomes inferior to that of original interferograms due to loss of a part of bandwidth. To reduce the effect of ionospheric artifacts correctly, short perpendicular baselines between two SAR images are required.

Figure 2-1 shows an example of the application of the range split spectrum method for PALSAR-2 data covering the mid-west Kyushu island, Japan. Although the data was expected to contain the post-seismic deformation signal associated with the 2016 Kumamoto earthquake sequence, patches and/or streaks of phase difference appeared in the interferogram. The co-seismic deformation due to the episode and its implications are reported in Chapter 6. To understand the InSAR data in detail, the range split spectrum method was applied to the PALSAR-2 data. Applying the range split spectrum method to the sub-band images, the dispersive and non-dispersive components can be distinguished, as shown in Figures 2-1c and 2-1d. The dispersive component shows wedge-shaped phase streaks across the data (Figure 2-1d). The azimuth offset and Multiple Aperture Interferometry (MAI) data also reveal strong streaks which were induced by the ionospheric disturbance (Figure 2-2). Therefore the wedge-shaped phase anomalies in the dispersive component are induced by the disturbance of TEC in the ionosphere. The non-dispersive component reveals ~ 1 phase cycle (~ 10 cm) of positive E-W aligned phase anomaly patches (Figure 2-1c). However, a few phase fluctuations were observed the area far from the epicentral region. The phase anomaly patches can indicate the surface movement from the post-seismic deformation (e.g., localized subsidence at urban area due to

liquefactions). However, an interferogram derived from images acquired on 10 May 2016 and 19 July 2016 shows a few centimeters of positive LOS changes near the epicentral area. At the time of data acquisition on 21 June 2016 (15:18 UTM), high rainfall intensity was observed across central Kyushu island according to the map of rainfall distribution on 15:10 and 15:20 21 June 2016 (UTM) (Figures 2-1e and 2-1f). The intensity of radar echo for identifying the precipitation per hour indicates E-W aligned patches of strong rainfall, whose locations are slightly westward from the locations of phase anomaly patches in the interferograms. The reason is that the locations of high precipitable water vapor are projected along the LOS direction as reported in Kinoshita et al. (2013). Thus the patches of phase anomaly indicate the tropospheric artifact due to strong rain clouds, not the actual crustal deformation.

Refractivity change due to variation of water vapor content in the troposphere and generates artifact phase difference in interferograms (tropospheric artifacts). According to Equation (2.5), the speed of microwave passing through high humidity (such as cloud patch) decreases because the refractive index of the troposphere is greater than 1. Therefore, the phase of the microwave is delayed if the microwave travels through a moist region. Theoretical tropospheric artifact is 10 cm of LOS changes for the 20% humidity variation (Howard et al., 1997). Several methods exist for correcting tropospheric artifacts using numerical weather models. Two examples are the Weather Research and Forecasting (WRF) model (e.g., Skamarock et al., 2008), and GNSS measurement (e.g., Li et al., 2012). After the generation of synthetic phase artifacts using the numerical weather model, the tropospheric artifacts due to the precipitable water vapor can be significantly reduced. GNSS measurement can detect surface movement with sub-centimeter accuracy, although the water vapor content contaminates the measurement accuracy. Phase anomaly due to atmospheric delay is reduced using zenith wet delay which is derived from a modeled mapping function. The spatial resolution of the precipitable water vapor distribution in the weather model and GNSS measurement are inferior to that of the InSAR

phase difference. However, the temporal resolution of InSAR is lower than that of the weather model and GNSS measurement. To correct the tropospheric error using the weather model and GNSS measurement, oversampling, interpolations and data assimilation for refining the spatial resolution must be applied (e.g., Kinoshita et al., 2013).

Although InSAR is one of the most robust techniques for monitoring surface movement using SAR data, certain factors usually contaminate processing results. Zebker and Villasenor (1992) described three main factors of decorrelation noise: thermal, temporal, and spatial decorrelations. Thermal decorrelations are induced by an irregular thermal excitation of free electron on sensors. Thermal noise can be expressed by the SNR. Hence, decorrelation problems would be caused at a region with low SNR. Temporal decorrelations are caused by changing of scattering characteristics from a target point between an interval of two image acquisitions. Examples which cause a change of scattering characteristics include snow covering, volcanic ash covering, flooding, drastic ground deformation. Zebker and Villasenor (1992) investigated variations of decreasing correlation as time passes non-vegetated, forested and lava flow covered regions in Oregon. Spatial decorrelations are dependent on observation geometries and volumetric scattering. The variation of observation geometry causes the differences in incidence angle and Doppler centroid frequency. The volumetric scattering is dependent on radar penetration depths, the wavelength of microwave used and scattering objects.

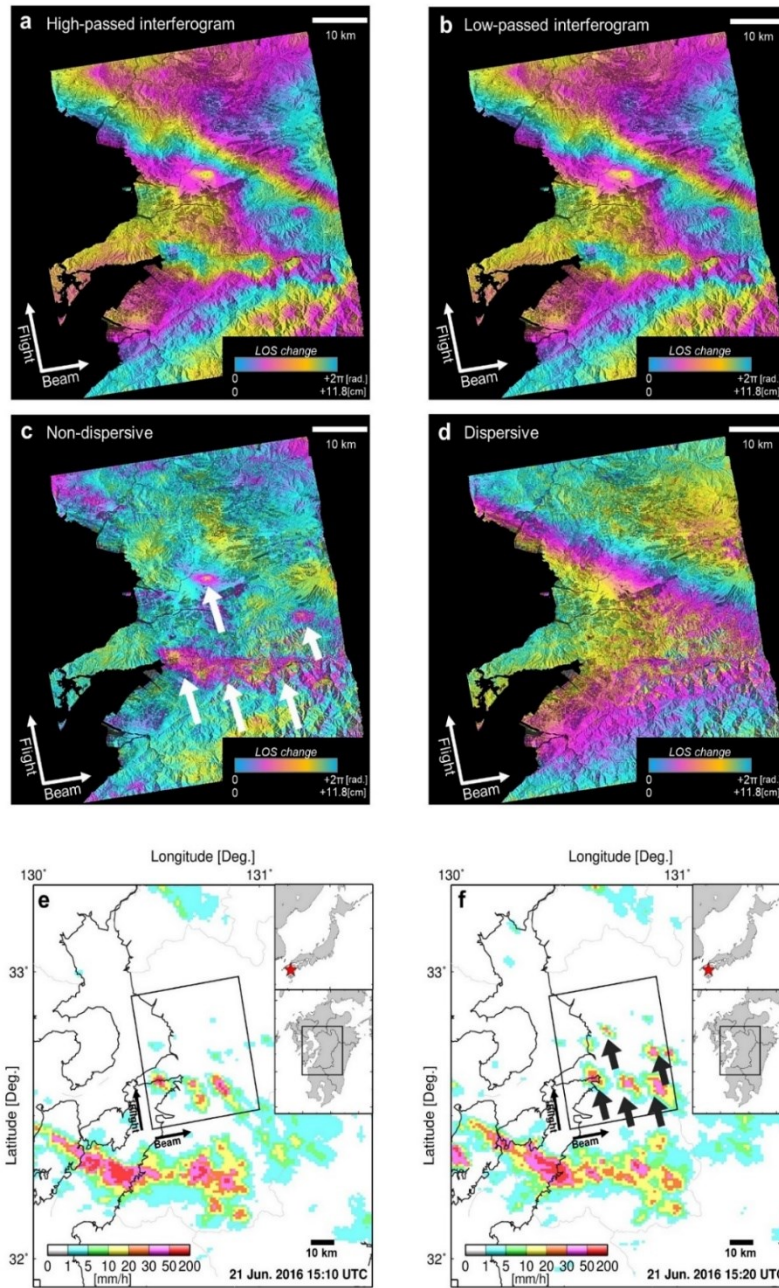


Figure 2-1. An example of the range split-band spectrum method for PALSAR-2 dataset. The original bandwidth is 79.4 MHz. Perpendicular baseline between two SAR images is -112.21 m. Master image was acquired on 10 May 2016, slave image was acquired on 21 June 2016, 15:18 UTC. The reduced bandwidth is 26.4 MHz which is nearly one-third of the original bandwidth. a) High-passed sub-band interferogram, b) Low-passed sub-band interferogram, c) Non-dispersive component, d) Dispersive component. One color cycle in Fig. 2-1a-d indicates 11.8 cm of line-of-sight displacement. e) Precipitation intensity observed by synthetic radar on 21 June 2016, 15:10 UTC, and f) 15:20 UTC. Red star in Fig.2-1e-f indicate the location of study area.

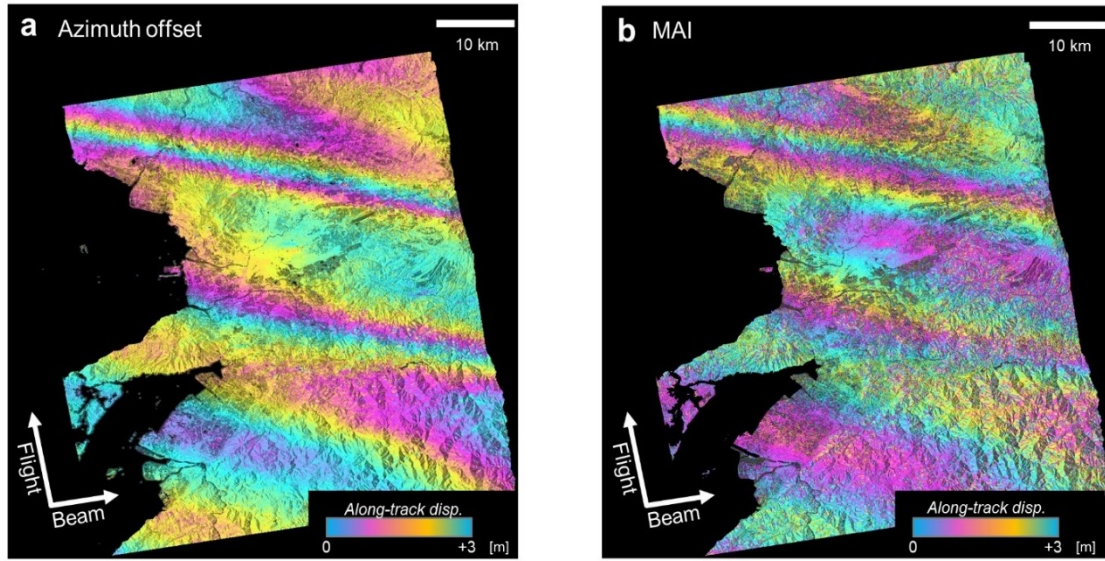


Figure 2-2. Azimuth offset and MAI data which are derived from same PALSAR-2 dataset in Figure 2-1. a) Azimuth offset, and b) MAI data. Azimuth offset and MAI data are sensitive to horizontal displacement along the satellite flight direction. Note that one color cycle in azimuth offset and MAI represents 3 m of horizontal displacement along the satellite flight direction.

Quantitative degrees of decorrelation are usually evaluated as coherence. The coherence can be defined as:

$$\gamma = \frac{|\langle c_1 c_2^* \rangle|}{\sqrt{\langle c_1 c_1^* \rangle \langle c_2 c_2^* \rangle}} \quad (2.7)$$

where γ is coherence, which can range from 0 to 1. Decorrelation problems induce a decreasing value of γ . c_1 and c_2 are average signal values of two SAR images at a pixel. The superscript * means the complex conjugate (Zebker & Villasenor, 1992; Zebker et al., 1996).

MAI is an example of the phase-based SAR processing technique to detect surface movement (Bechor & Zebker, 2006). The technique reveals horizontal displacement along the satellite flight direction. Hence, the MAI data enables easy understanding of the geometry of surface movement.

MAI data can be derived by combining forward-looking interferograms and backward-interferograms. These forward-looking and backward-looking single-look complex (SLC) images are generated by splitting the Doppler spectrum for azimuth direction, indicating the filtering bandwidth for azimuth direction. The MAI data allow mapping of the relative TEC distribution with high-spatial resolution through integration of the phase difference in the azimuth direction (Jung et al., 2013). During this processing, both topographic and orbital fringes between forward- and backward-looking interferograms can be reduced.

The phase difference in MAI φ_{MAI} can be described as

$$\varphi_{MAI} = -\frac{4\pi}{l}nx \quad (2.8)$$

where l is effective antenna length, n is normalized squint, and x is horizontal displacement along the satellite flight direction. Bechor and Zebker (2006) reported that the measurement accuracy of MAI data depends on the coherence. For example, measurement accuracy of ~ 8 cm was obtained for coherence of 0.6. For the PALSAR-2 sensor, $l = 10$ m and a normalized squint of $n = 0.5$ is generally employed.

2.2.2 Pixel tracking

Another SAR processing method involves a pixel tracking approach to detect surface displacement. This approach identifies offsets between two coregistered images from a linear function using the normalized cross-correlation function (e.g., Michel et al., 1999). Generally, image coregistration employs affine transformation, which can describe rotation, projection, reflection, shearing, and scaling. Affine transformation can coregister the outline of images. However, the local offset on images remains. While the local offset had been considered as residue, even these offsets can match with sub-pixel accuracy using normalized cross-correlation functions (Li & Goldstein, 1990). The

pixel tracking approach measures that residue after linear image coregistration. Therefore, measurement accuracy of the pixel tracking method strongly depends on the accuracy of image coregistration, which is generally evaluated by coefficient of cross correlation (De Zan, 2014). Other papers considered measurement accuracy of the pixel tracking method as using the RMS around a stable (no deformation) region (Kobayashi et al., 2009), RMS between GNSS measurement, pixel tracking results (Fialko et al., 2001; Sandwell et al., 2008), or standard deviations (Strozzi et al., 2002). Low image SNR, large temporal baseline and changing surface condition between two images would cause poor accuracy of image matching. Although advanced techniques of image coregistraion have been improved based on orbital information and DEM (Sansosti et al., 2006) or point scatterers (Serafino, 2006), the normalized cross correlation can identify offset with measurement accuracy of 1/10-1/20 pixels (Strozzi et al., 2002). In other words, higher spatial resolution can identify smaller displacement. Recently, Casu and Manconi (2016) have reported the time-series of pixel tracking data for detection of long-lasting crustal deformations following the Afar dike intrusion in 2005. The pixel tracking approach can be applied to both SAR images and optical images for identifying surface movements. For example, Hollingsworth et al. (2012) revealed meter-scale crustal deformations due to the 1975-1984 Krafla rifting episode in NE Iceland by applying the pixel tracking approach to SPOT5 optical images and aerial photos(Fahnestock et al., 2016).

The pixel tracking method has two main advantages compared with interferograms. First, the method can identify surface movement with high displacement gradient. Because the cross-correlation identifies offsets in SAR images itself, unwrapping errors can be avoided at high displacement gradient. Therefore this approach can also detect the location of surface ruptures due to large earthquakes at shallow depth. Theoretically, the decorrelation problem could occur if the displacement gradient is larger than half the radar wavelength per pixel (Baran et al., 2005). For

example, the threshold of the displacement gradient of PALSAR-2 interferograms observed by SM3 mode is 27.4 mm/m. The second advantage of the pixel tracking method is that it can reveal two displacement components: one is sensitive to the LOS direction (range offset) and the other is sensitive to the along-track direction (azimuth offset). To retrieve three-dimensional displacements using interferograms, any three datasets from ascending track, descending track, and right- or left-looking observations. When the pixel tracking method was applied to the dataset observed from both ascending and descending tracks, four independent four displacement components are found. Using these four displacement components, the three-dimensional displacement can be retrieved by solving an over-determined least squares problem. Tobita et al. (2001) were the first to report three-dimensional displacement using the pixel tracking method.

The pixel tracking approach also has two disadvantages. Firstly, the spatial resolution of pixel tracking is worse than that of interferograms. Approach requires arbitrary window size is required to identify a peak of cross correlation where the location of the peak is recognizable as residue. Thus, the window size is consistent with the spatial resolution of pixel tracking. Generally, window size is set from 32 to 256 pixels. Smaller window size can identify local displacement features, although the uncertainty would be large. In contrast, the larger window size can reveal reliable pixel tracking results, but the spatial resolution is lower. The second disadvantage is the low measurement accuracy. Interferograms can identify a few centimeters displacement. However, the pixel tracking approach can detect ground deformations with 1/10-1/20 pixels of measurement accuracy.

Another characteristic is that azimuth offset is more easily contaminated by ionospheric artifacts (Gray et al., 2000; Meyer, 2011). Although ionospheric noise is a factor, the strongest factor is the ionospheric disturbances at E and/or F layers causing ray-bending of the microwave. MAI are

also more easily contaminated for the same reason (Bechor & Zebker, 2006; Jung et al., 2009).

2.2.3 Time-series analysis

Another SAR processing approach, not adopted in this thesis, is time-series analysis. Time-series analysis for SAR data is suitable for detecting long-lasting small displacements. For example, subsidence in urban areas, and volcanic deformation due to magma source inflation/deflation. The signal of an actual small deformation and atmospheric/ionospheric artificial errors cannot be distinguished within an interferogram, because the signal amplitudes are close in size. Time-series analysis approaches need to process large volume of SAR data covering the same region to identify slow and/or small movements. However, any randomly-appearing artificial errors are cancelled out. These approaches can detect displacement rates of sub-centimeters per year if the processing conditions are good. Generally, increasing the number of images and using a small spatiotemporal baseline make it possible to improve the measurement accuracy. Another advantage compared with conventional InSAR is avoidance of the temporal decorrelation problem. Although longer intervals between SAR data acquisitions induces temporal decorrelation, the time-series analysis can reveal long-term continuous deformation. To apply the time-series analysis, the Stanford Method for Permanent Scatterers (StaMPS) software is one of the most well-known non-commercial softwares for processing time-series analysis (Hooper et al., 2004).

The most widely-known analysis methods are conventional stacking, Permanent Scatterer InSAR (PS-InSAR), and the Small-Baseline Subset (SBAS). The conventional stacking approach estimates average deformation rates by dividing cumulative displacement by each data acquisition interval (e.g., Zebker et al., 1997). Atmospheric artificial errors are eliminated by averaging multi interferograms. Although conventional stacking is superior for detection of signals with constant

displacement rate, it is inferior for detection of signals with seasonal trend and/or fluctuation. The two other approaches (PS-InSAR and SBAS) can identify displacement rates with variations.

The PS-InSAR approach can detect LOS displacement at permanent scatterer (PS) points, in cases where the phase coherence is stable during the acquisition period (Ferretti et al., 2000, 2001). Artificial objects, for example buildings in metropolitan areas, tend to be PS points which are stable with respect to backscatter intensity. In contrast, it is difficult for vegetated regions (where temporal backscatter intensity varies) to be PS points. The pixels containing stable coherence points can avoid temporal and spatial decorrelation problems. PS points are selected using criterion of phase coherence or SAR intensity dispersion (Ferretti et al., 2000, 2001). Hooper et al. (2004) reported that vertical deformation from 1992 to 2000 was detected at Long Valley Caldera in California by applying the PS-InSAR approach to the ERS-1/2 dataset. The temporal variation of the vertical deformation is almost consistent with their electric distance meter (EDM), leveling, and GPS measurements. The paper also suggested that PS-InSAR is superior at avoiding temporal decorrelation by comparing conventional InSAR and PS-InSAR data.

SBAS infers the displacement rate by analyzing the SAR dataset with small spatiotemporal baselines (e.g., Berardino et al., 2002; Schmidt & Bürgmann, 2003). Interferograms with small spatiotemporal baseline also allow the decorrelation noise to be minimized even if there is no scatterer in the pixel. Pixels are selected better points based on spatial coherence maps. This is the reason SBAS utilizes several master images to reveal time-series of displacement, while PS-InSAR select single master image. PS-InSAR selects a single image after extracting the time-series of deformation signal, filtering the inferred time-series results in both the time and space domains to decompose tropospheric artificial errors from the average displacement rate. Schmidt and Bürgmann (2003) reported vertical

movement due to seasonal variations of groundwater level at the Santa Clara Valley in California, by applying the SBAS approach to the ERS-1/2 dataset.

Chapter 3

Aseismic Strike-slip on Graben Subsidence Associated with the 2007 Natron Dike Intrusion Episode, Tanzania

The contents of this chapter have been published in *Tectonophysics*

Himematsu, Y., M. Furuya (2015) Aseismic strike-slip associated with the 2007 dike intrusion episode in Tanzania, *Tectonophysics*, 656:52-60, DOI 10.1186/s40623-016-0545-7

Chapter 3. Aseismic strike-slip along graben subsidence associated with the 2007 Natron dike intrusion episode, Tanzania

3.1 Introduction

The East African Rift (EAR) valley is a divergent plate boundary between Nubian plate and Somalian plate that extends the length of ~5000 km-long from Ethiopia to Mozambique (e.g., Ebinger, 1989; McKenzie et al., 1970). The EAR contains numerous normal faults and Quaternary active volcanoes along the rift (e.g., Hamling et al., 2009; Paquet et al., 2007). Also, moderate-sized earthquakes frequently occur along the plate boundary (e.g., Chorowicz, 2005). Northern Tanzania is located in the middle of the EAR, and the relative opening rate is 2–4 mm/yr along the E–W direction according to the GPS measurement (Saria et al., 2014; Stamps et al., 2008). The 2007 swarm near the Lake Natron started on July 12 (e.g., Calais et al., 2008). The largest earthquake with moment magnitude (M_w) 5.9 occurred on July 17, and the swarm activity continued until the middle of September 2007 (Figure 1). The campaign-based local seismic network revealed the details of spatial–temporal distribution of epicenters, indicating a migration of earthquake swarm from a deeper depth to the SW toward a shallower depth in the NE (Albaric et al., 2010). Albaric et al. (2010) and Global CMT catalogue (<http://www.globalcmt.org>) reported that eight earthquakes with magnitude larger than 5 occurred during the event, all of which indicated ENE–WSW striking normal fault at depths shallower than 20 km. A swarm of more 1400 earthquakes was recorded for 180 days by a campaign seismic network since June 1 (Albaric et al., 2010). Earthquake swarms are often accompanied with magma intrusion (e.g., Aoki, 1999). Mt. Oldoinyo Lengai located about 20 km to the SW from the swarm, is one of the most active volcanoes along the EAR. In 2007, an effusive eruption started one month prior to the swarm activity for the first time in 24 years. The eruptive activity of Mt. Oldoinyo Lengai abruptly switched to episodic explosive eruptions when the swarm activity was decaying in

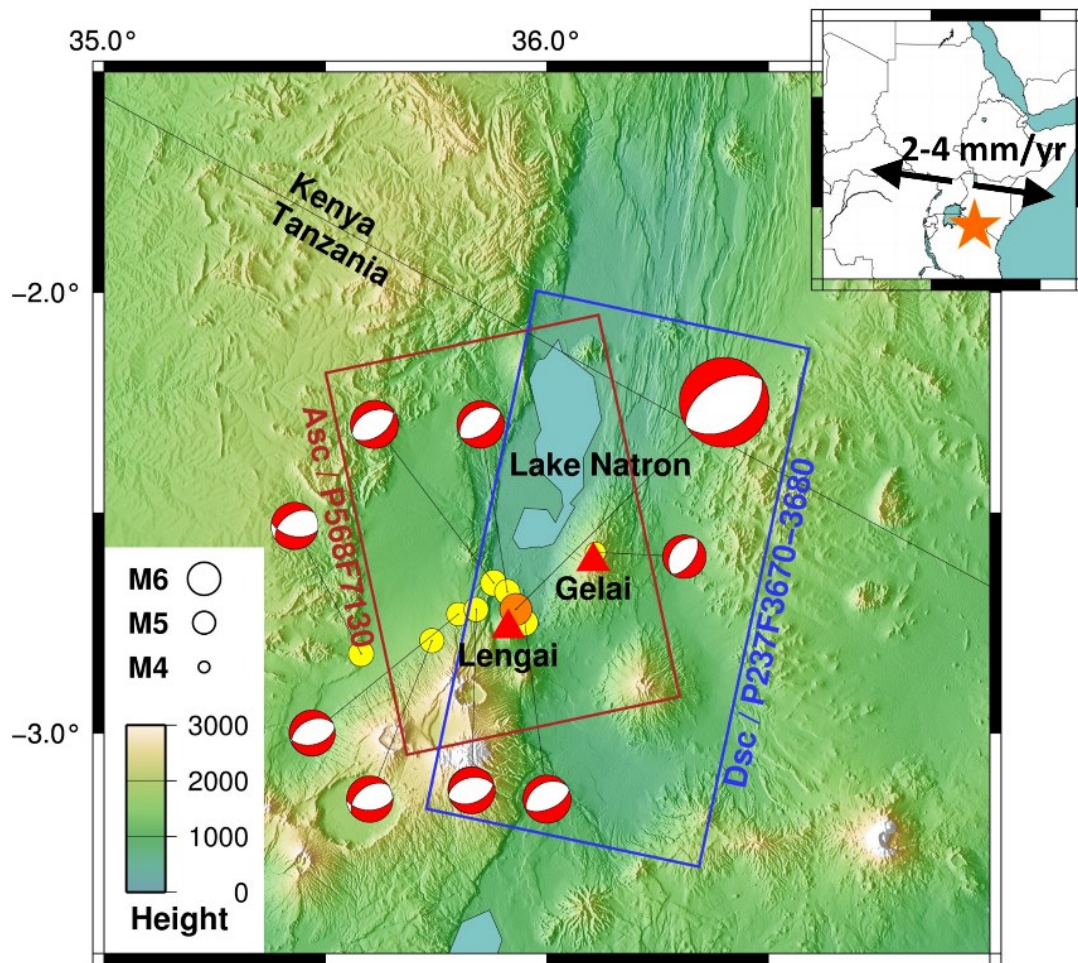


Figure 3-1. Study area in Chapter 3. Yellow and orange circles indicate the locations of epicenter of greater than M5 earthquakes and that of a mainshock during the 2007 event, respectively. Beachballs show each focal mechanism. A wide map of the study area is shown at the upper-right of the figure. Colored rectangulars indicate footprints of the PALSAR data we used in this chapter. Star represents the location of study area. Black arrows show the far-field displacement direction derived from the GPS measurement (Saria et al., 2014; Stamps et al., 2008).

September and continued until April 2008. Several previous studies have already reported the crustal deformation signals associated with the swarm by using satellite synthetic aperture radar (SAR) data (Baer et al., 2008; Biggs et al., 2009; Calais et al., 2008). Calais et al. (2008) pointed out the presence of aseismic slow slip besides the dike intrusion and examined the details of the dike intrusion processes using the high temporal resolution SAR data. Baer et al. (2008) examined the Coulomb stress changes

associated with the event to study the interaction of each fault source. Biggs et al. (2009) studied the relationship between the length of dike and the size of magma chamber compared with those in Afar and Iceland events. In regard to the relationship between the Oldoinyo Lengai eruption and the swarm, Baer et al. (2008) considered that the passage of the seismic-wave through the magma chamber could dynamically trigger the eruption, whereas Biggs et al. (2009) reported that there was no relationship between the eruption and the swarm due to the ground deformation spanning 2001–2004 implies no significant pressure changes in the magma chamber. Thus, the interrelation between the eruption and the event is still uncertain. The objectives of this paper are to report the three-dimensional (3D) displacement fields that have never been reported by the previous studies and to show our source modeling results. This was made possible by a couple of reasons. Firstly, in contrast to the previous studies, we used L-band ALOS/PALSAR images acquired from both ascending and descending tracks. The L-band SAR is more advantageous in terms of the easiness of phase unwrapping even the areas with large phase gradient. Secondly, we apply both InSAR and offset-tracking methods that can reveal the full 3D displacements. Based on the inferred fault slip model, we also discuss the implications for the regional stress field and their possible role for the generation of fault segmentation along the rift axes. Moreover, we point out the possibility of the aseismic slip as the driver of earthquake swarm.

Table 3-1. ALOS-1/PALSAR-1 dataset in this chapter

Pair No.	Date (dd.mm.yyyy)	Orbit	Path	Frame
1	07.07.2007-07.10.2007	Asc.	568	7130
2	05.06.2007-13.06.2007	Dsc.	236	3670-3680

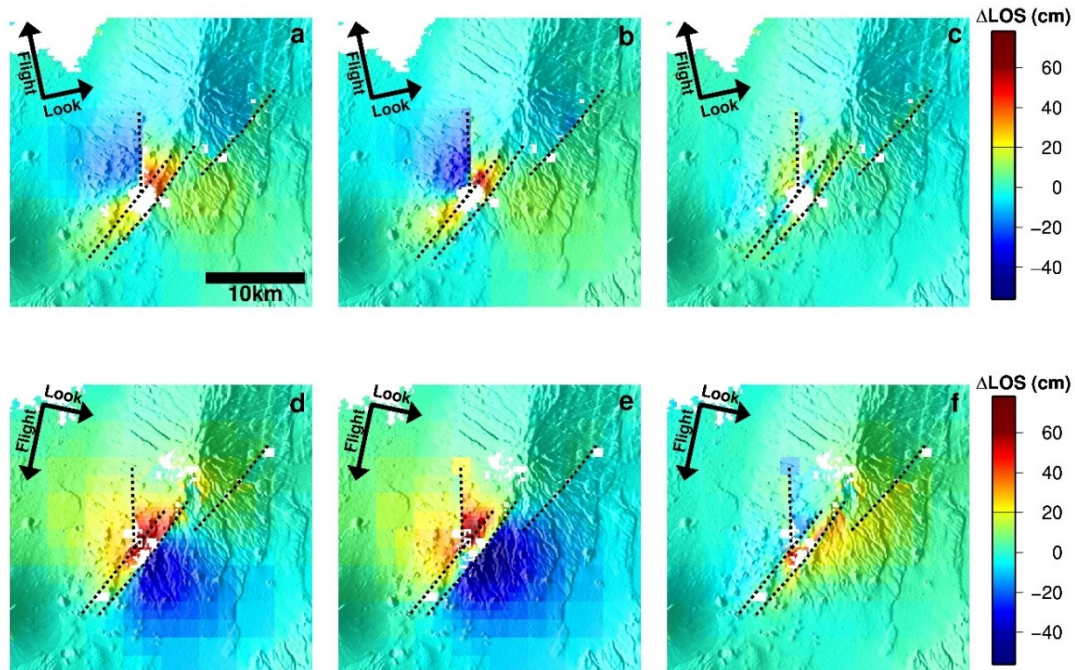


Figure 3-2. Subsampled PALSAR-1 InSAR data which show co-diking displacement associated with the 2007 Natron dike intrusion episode. a-c) Unwrapped PALSAR interferograms observed from ascending track. a) Subsampled observation, b) calculation, and c) misfit residual. d-f) Unwrapped PALSAR interferograms observed from descending track. a) Subsampled observation, b) calculation, and c) misfit residual. Black dot lines traced the top locations of fault segment in our elastic model (see Figures 3-4 and 3-6). Positive signals represent displacement along the line-of-sight away from the satellite.

3.2 Methods and results

Satellite-based SAR is helpful to obtain ground surface deformation signals with unprecedented spatial resolution over wide areas (e.g., Hanssen et al., 2001; Massonnet & Feigl, 1998). We detected the deformation signals associated with the 2007 event using both ascending and descending ALOS/PALSAR (L-band, 23.6 cm wavelength) images (Table 1), providing us with the range changes along the radar line of sight (LOS) from two independent directions. We also applied the offset-tracking method to derive the displacements projected along the satellite flight direction. We could

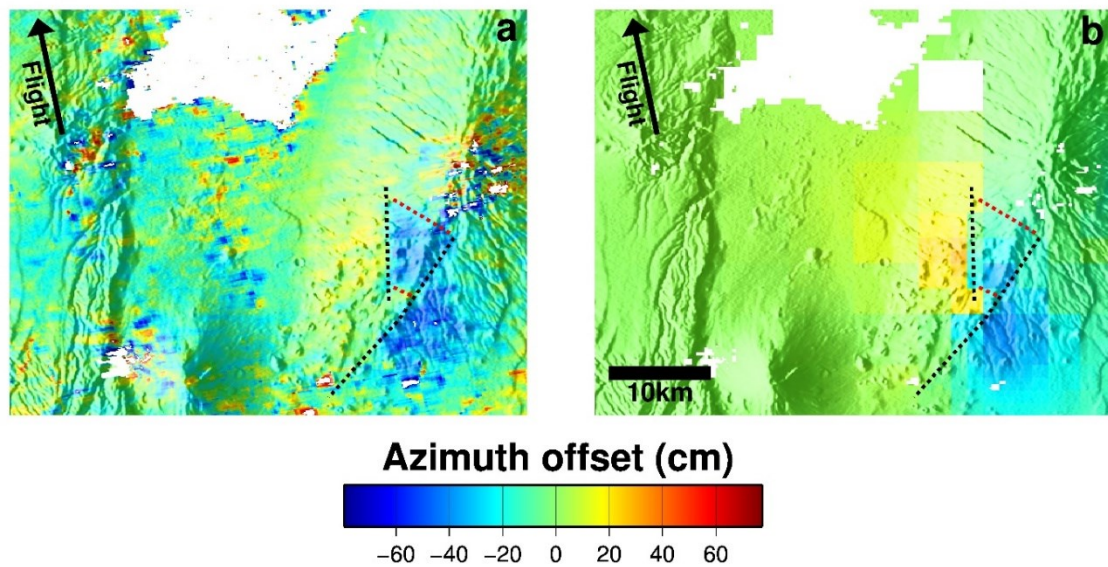


Figure 3-3. Observation and calculation of azimuth offset for ascending orbit. a) Observed azimuth offset derived from PALSAR ascending track (Pair No. 1 in Table 1). b) Simulated azimuth offset derived from the inferred opening/slip distributions in our optimal model (see Figure 3-6). Black dashed lines represent the top of the two facing faults. The two phase discontinuities along the direction orthogonal to the fault strike are indicated by red dots lines. Upper-right arrows show the direction of the satellite flight direction.

thus derive the 3D displacements associated with the entire episode. The off-nadir angles are 34.3° for both tracks. The ascending data set (7 July 2007 to 7 October 2007) and the descending data set (5 June 2007 to 13 June 2010) cover the entire swarm period (Figure 1). While the temporal coverage of the descending InSAR image is much longer than that of the ascending InSAR image, because no descending images were acquired between July 2007 and June 2010, and the descending InSAR could include post-seismic deformation signals. However, we confirmed insignificant deformation signals after October 2007 from the ascending post-seismic interferogram (7 October 2007 to 15 July 2010) that revealed very little deformation (Fig. S2). To remove the topographic fringes in InSAR data, we used the 3 arc-second (90 m) Shuttle Radar Topography Mission (SRTM) digital elevation model (DEM) (Farr et al., 2007). SAR data were processed by GAMMA software (Wegmüller & Werner,

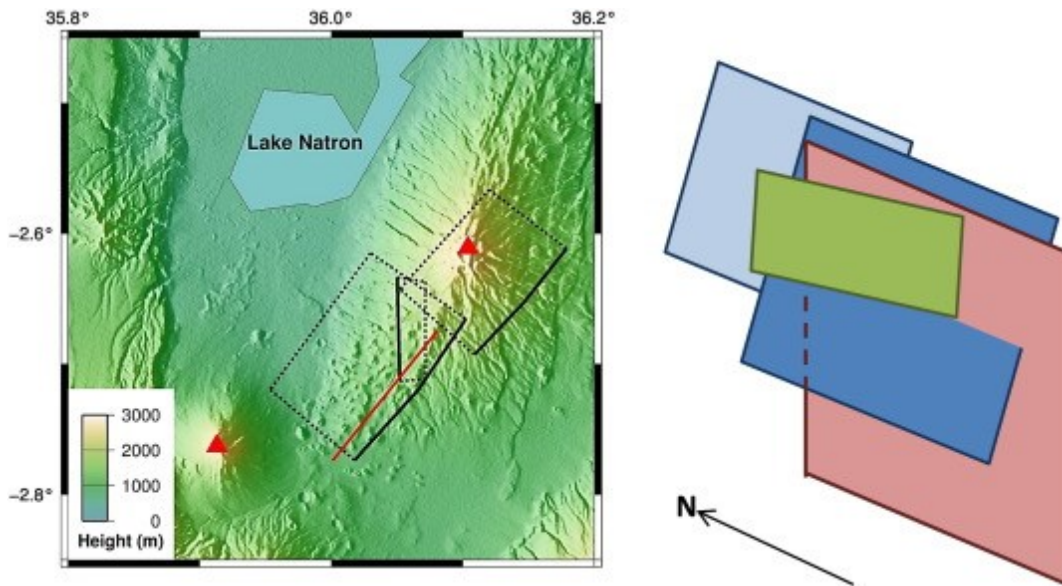


Figure 3-4. Surface projection and 3D description of our optimal elastic model. (Left) Solid lines mark the top edge of the faults, and the dashed lines indicate the side and bottom edges of the faults. Red indicates the location of the dike segment. (Right) Blue segments indicate east-dipping faults, green segment is east-dipping fault, and red segment is dike. The inferred slip distributions are shown in Figure 3-6.

1997). Although we corrected for the orbital and topographic fringes with the use of precision orbit data by JAXA and SRTM DEM, respectively, there still remain long-wavelength phase trends and topography-correlated fringes. The effects of long-wavelength trend and topographic-correlated atmospheric delay in the interferograms were removed, by fitting low-order polynomials and DEM, respectively. For phase unwrapping, we used the branch-cut algorithm (Goldstein et al., 1988). While the unwrapping error would appear at different locations in the ascending and descending data, we confirmed that the phase discontinuities were observed at the same locations, suggesting that they are real deformation signals. The observed InSAR data for both ascending and descending tracks are shown in Fig. 2a and d. They are resampled with the quad-tree algorithm to effectively reduce the number of data points from ~25,000 to ~4000 (Jonsson et al., 2002). The two interferograms indicate two clear phase discontinuities around the center of the graben that strike NE–SW (36.10E, 2.66S–

36.01E, 2.77S) and NNW–SSE (36.05E, 2.63S–36.05E, 2.71S). We also identify another phase discontinuity to the NE that is particularly clear in Fig. 2a. The area between the two discontinuities indicates an increase in the radar line of sight (LOS) in both ascending (Figure 2a) and descending data (Figure 2d), suggesting that the area has subsided. In contrast, outside this region the signal in the ascending and descending data is opposite, suggesting E–W motion (Figures 2a and 2d). We can thus roughly interpret that the LOS-increasing area was subsiding, and that the outer eastern and western areas were moving to the east and west, respectively. The interferograms indicate that the subsidence area covers 3–4 km width and 13–15 km length. The maximum positive range changes are 46 and 63 cm in ascending and descending data, respectively. Overall, the spatial pattern of the deformation signals looks like a graben structure, which has been reported at other rifting episodes such as the 2009 western Arabia, the 2007 Dallol, and the 1998 Réunion island (Baer & Hamiel, 2010; Fukushima et al., 2010; Nobile et al., 2012). As shown below, however, the azimuth offset data exhibit some unexpected signals. Azimuth offset data derived from the ascending path similarly indicates two discontinuities (Figure 3a) that are compatible with the expanding areas with E–W motion in the interferograms (Figures 2a and 2d). The most remarkable point is that the subsiding zone indicates ~40 cm negative offset, which indicates that the area has moved opposite to the satellite flight direction. Namely, the central subsiding region was not only subsiding but also moving horizontally, because the azimuth offsets have no sensitivities to the vertical displacements. Although the azimuth offset derived from the descending pair is much noisier due to the lower-coherence, the data set also exhibits small horizontal displacements that are nearly in parallel with the satellite flight direction (Fig. S1). The azimuth offset data from both ascending and descending tracks thus unambiguously indicate horizontal displacements of a subsiding graben structure. Biggs et al. (2009) showed a result from multiple aperture InSAR (MAI) measurement (Bechor & Zebker, 2006), which are quite consistent with Fig. 3a in terms of both the signal amplitude and the deforming area. Nevertheless, they dismissed

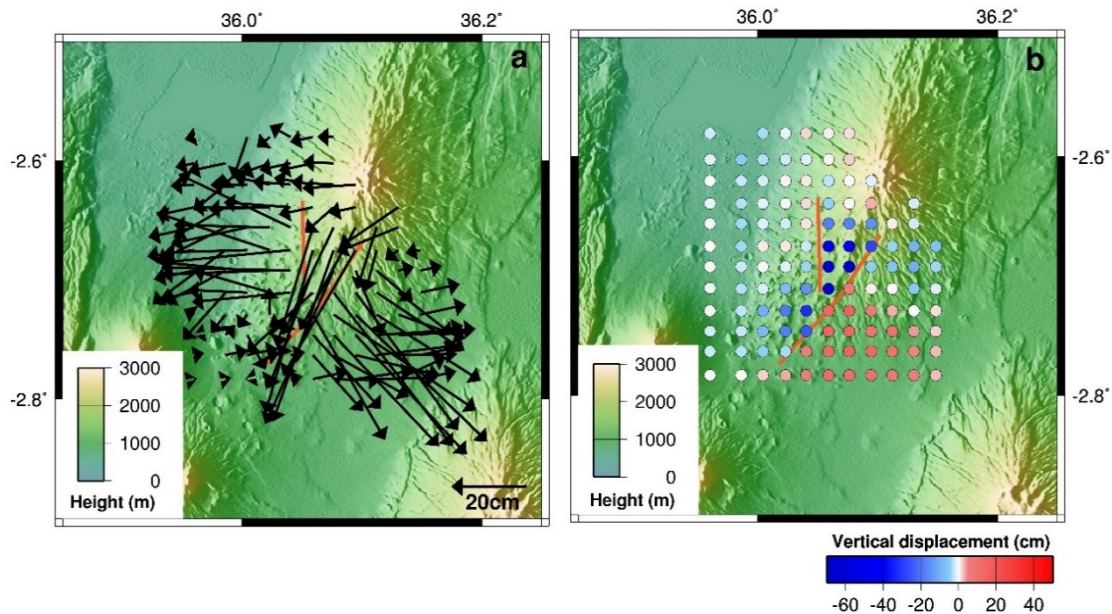


Figure 3-5. 3D displacement inferred from PALSAR-1 interferograms and pixel tracking data. (a) Horizontal displacement, and (b) vertical displacement. Orange solid lines indicate the top locations of the fault segments in our model.

the MAI observation in their analyses, probably because there were no other independent data that could support the signal. We calculated 3D displacements from the ascending and descending interferograms and the azimuth offset (Figure 5a) (Fialko et al., 2001). The orange lines in Figure 4 show the locations for the top edges of our fault source models shown below. The interval of the observation point is 2×2 km. The lack of the points around the summit of Mt. Gelai is because the azimuth offsets are noisier than the InSAR data and thus such area are masked. The horizontal displacements in Fig. 5a indicate that the western and the eastern half of the areas moved up to ~ 35 cm toward W–WSW and ~ 51 cm toward E–NE, respectively. The subsidence zone moved toward SSW direction with a maximum horizontal displacement of ~ 48 cm. The vertical displacements are shown in Figure 5b, which indicates that the eastern half was uplifting, and the center area was subsiding by ~ 62 cm. In contrast, the western half was uplifting by only a few centimeters.

3.3 Elastic source model

Static ground displacements associated with earthquakes and/or dike intrusion episodes are often interpreted by using analytical solutions due to planar rectangular dislocation elements in elastic half-space (Okada, 1985). In this study, we estimate non-planar fault planes based on the analytical solutions due to triangular dislocation elements because the observations reveal complex deformation signals. The triangular dislocation elements are advantageous because it can represent non-planar fault planes without making unrealistic overlaps or gaps (Furuya & Yasuda, 2011; Maerten et al., 2005). To calculate the ground deformation due to the triangular dislocation elements, we use the MATLAB script that is made available by Meade (2007). To generate the mesh coordinates for the non-planar planes, we used Gmsh software (Geuzaine & Remacle, 2009). Almost all the focal mechanisms of the earthquakes during the event show normal faulting. We set a west-dipping and an east-dipping fault whose top edges can match the locations of the phase discontinuities in the interferograms (Figures 4 and 6); the other parameters for the fault geometry, the bottom location and depth, were estimated by trial-and-errors (e.g., Furuya & Yasuda, 2011). We set another west-dipping fault at the eastern flank of Mt. Gelai (Figure 6e–f), because the two interferograms indicate a phase discontinuity at the same location. The deformation pattern is consistent with a dike intrusion and can be modeled as a tensile opening dislocation source. We set a vertical tensile dislocation source as the dike segment, whose horizontal location is the center of the subsidence zone. Without dike opening, we could have only reproduced the subsidence zone with smaller E–W extension displacement. The final position of the dike segment was set where the RMS misfit was minimum. We thus estimated three faults and one dike segment to explain the crustal deformation (Figure 5). Our model is similar to the geometry of Baer et al. (2008), regarding an east-dipping fault, two west-dipping faults and a dike segment. After setting the location and geometry of the fault sources and dike, we performed a linear least squares inversion to derive the spatially variable slip and opening on the fault and dike, inverting jointly the

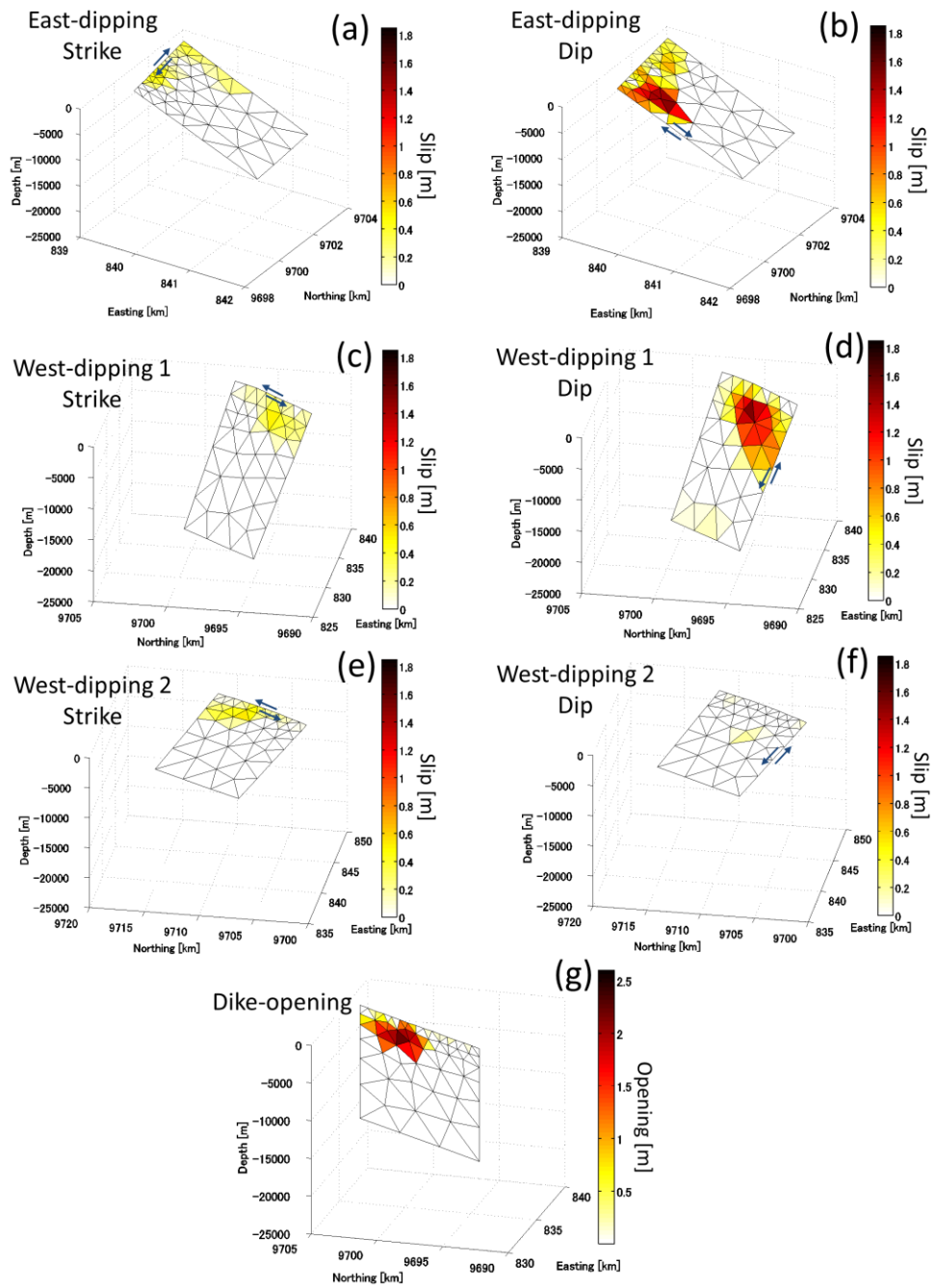


Figure 3-6. The inferred dike opening and slip distributions. Distribution of (a) Strike-slip and (b) normal faulting along the east dipping fault. Distribution of (c) Strike-slip and (d) normal faulting along the west-dipping fault 1. Distribution of (e) Strike-slip and (f) normal faulting along the west-dipping fault 2. (g) Opening distribution along the dike. All figures are plotted in the UTM coordinate (Zone 36).

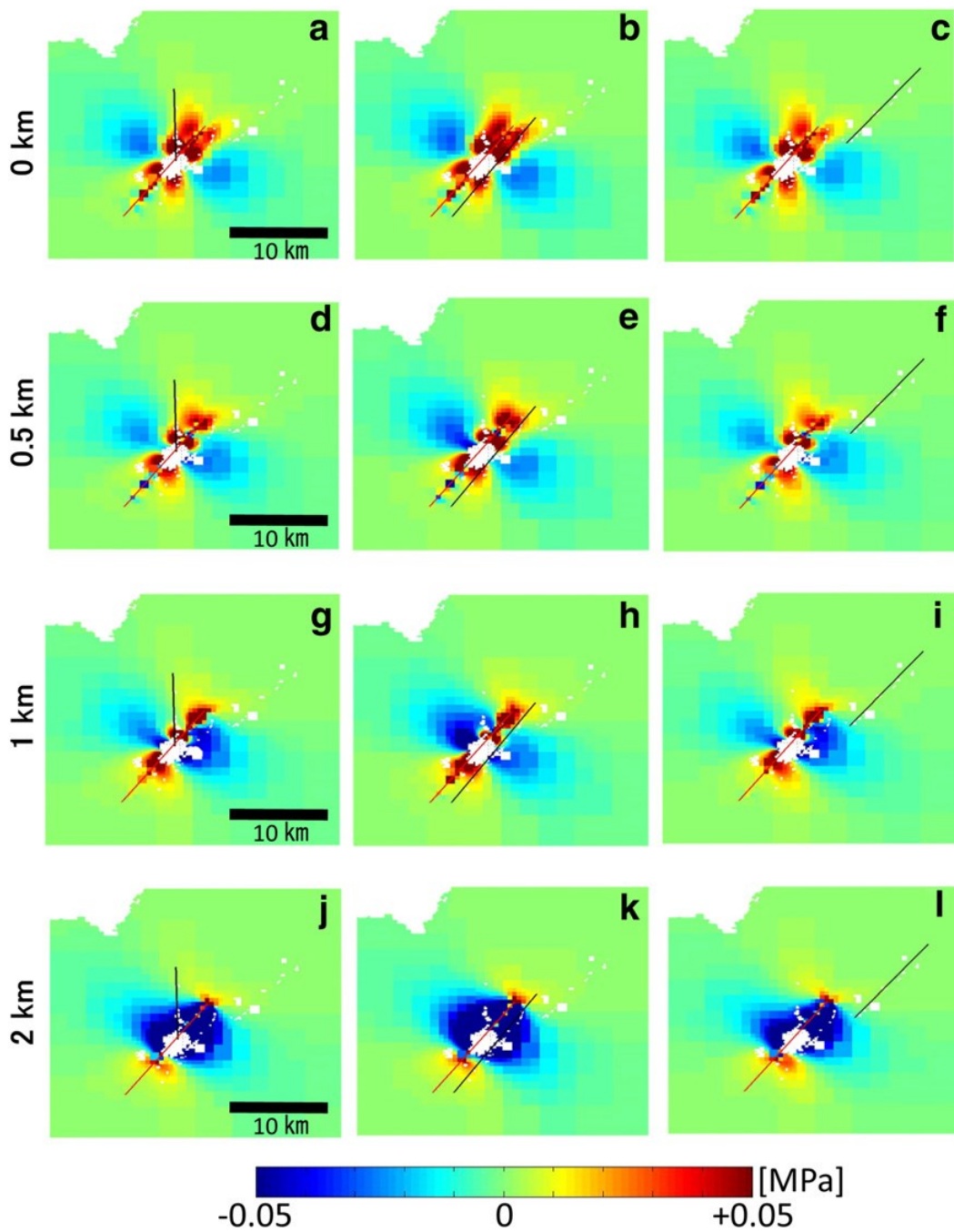


Figure 3-7. Coulomb stress changes for each receiver fault (black lines) due to the dike opening as the source fault (red line). The top edges of the receiver faults are shown as black lines (left column: east-dipping fault, center: west-dipping fault, right: shallow west-dipping fault). Stress changes indicate positive (unclamping) the near surface, and the most negative (clamping) at the depth of maximum dike opening around 2–3 km.

ascending and descending interferograms. Here we do not invert for the azimuth offset data, and instead we check the consistency a posteriori as argued below. In solving the least squares problem, we applied a “non-negativity” constraint. Namely, in order to derive physically plausible slip distributions, we prescribed that the east-dipping and west-dipping faults are allowed to slip right-laterally and left-laterally, respectively, and that the dip slip on each segment has only normal slip component. The dike segment is allowed to have only pure opening. Moreover, we apply a smoothing constraint on the slip distribution by using an umbrella operator that is equivalent to the Laplacian operator for the rectangular dislocation elements (Maerten et al., 2005). The moment release from the fault lip distribution can be calculated, assuming Poisson ratio of 0.25 and shear modulus of 30 GPa. The optimum fault slip and dike opening distribution on each segment are shown in Fig. 6. Each fault slip distribution has maximum amplitude around the depth of ~ 5 km with their amplitudes up to 60 cm in the strike-slip and 160 cm in the dip slip. As expected from the Global CMT solutions that indicate predominantly normal faulting, the normal slip is much larger than the strike-slip (Figures 6b and 6d). However, the inferred strike-slip component is unexpectedly larger than that inferred by seismology (Figure 6a and 6c). The calculated geodetic moment for the dip slip component is 3.3×10^{18} Nm, and that for the strike-slip component is 8.1×10^{17} Nm. Thus, the contribution of the strike-slip is 19.9%, and the equivalent moment magnitude for the dip slip and strike-slip is M_w 6.28 and 5.87, respectively. Because the cumulative seismic moment is 2.2×10^{18} Nm according to the Global CMT, it turns out that about 56% of the geodetic moment were released aseismically. The moment for the strike-slip must be responsible for the southward movement of the subsidence zone. The dike segment exhibits up to 220 cm opening at the depth of 2–4 km (Figure 6g), and the volume of intrusion is 0.036 km^3 . While we may include a Mogi-type deflation source to account for the source of the intruded dike, we cannot identify any circular signals in the observed InSAR data that allows us to constrain such a source. Although we do not discard the presence of a deflation source, we consider

that the depth of the Mogi source, if any, would be deeper than 3 km, because otherwise there would arise circular fringes; we then assumed that the Mogi source has the same volume changes as those of intruded dike. Moreover, even if we include the deflation source at the center of the largest displacement field, the E–W trending sharp offset at northern and southern edge of the negative signal will never be generated.

Based on the inferred fault slip and dike opening distribution, we computed the ground deformation (Figures 2b and 2e) and misfit residual (Figure 2c and 2f). RMS residual values in our model are 3.0 cm in the ascending and 6.3 cm in the descending data. Although there still remain some residuals in the eastern half of the descending data, the calculated deformation well reproduces the observations, and the misfit residuals cannot be distinguished from measurement errors that would be empirically less than 5 cm for a single interferogram. Also, we calculated the displacements for the azimuth offset, which also reproduces the characteristic offsets in the subsidence zone (Figure 3). Without the strike–slip component, we could not reproduce the large azimuth offset signals in the subsidence zone. Thus we conclude that the strike–slip is necessary to explain the observation results, and it occurred aseismically because almost all the Global CMT solution exhibits the normal-dip slip.

3.4 Discussion

To our knowledge, not only the previous studies of the 2007 Lake Natron event, but also many studies of dike intrusion events in rift settings elsewhere assume normal slip and dike opening in their fault source modeling (e.g., Baer & Hamiel, 2010; I. J. Hamling et al., 2014; Nobile et al., 2012; Wright et al., 2006). Focal mechanisms of earthquakes during the 2007 event indeed indicate few strike–slip components. In contrast, the fault source model we estimated in this study includes significant strike

components, without which we cannot reproduce the InSAR and azimuth offset observations. Considering the few strike-slip in the focal mechanisms, it turns out that aseismic strike components are required to explain the ground deformation associated with the 2007 Natron event. Why then did the aseismic strike-slip occur at the area that is supposed to extend in the E–W direction? Why did the subsiding area move toward the south that is orthogonal to the rift axis? In order to examine if the stress changes due to the dike intrusion promoted the fault slips, we computed the Coulomb stress changes (ΔCFF), based on our inferred fault models (e.g., King et al., 1994; Toda & Stein, 2002). In the calculations of the ΔCFF , we use a shear modulus of 30 GPa and a friction coefficient of 0.4. Figure 7 illustrates the distribution of the ΔCFF by the dike opening for each receiver fault at depths from the surface to 6 km. We observe positive values of ~ 0.05 MPa at shallower depths, suggesting unclamping, mainly distributed along the dike axis (Figures 7a–f). In the meantime, at the depths of 2–4 km at which we inferred the peak values of dike opening, the negative ΔCFF (clamping) are widely distributed (Figures 7j–r). Our inferred fault models indicate significant slip distributions mostly at shallower depths, and thus are mechanically consistent with the ΔCFF . In the above ΔCFF modeling, however, we do not consider the background tectonic stress fields. The two west-dipping faults are forming en-echelon structure, and the strike components are much larger than the normal slip at the shallower depth of the west-dipping fault to the northeastern end. There are many normal fault systems in the EAR, which are forming relay zones and segmented structures (Ebinger, 1989; Moustafa, 2002; Tesfaye et al., 2008). Relay zone is a geological structure formed by multiple overlapping, en-echelon fault segments and develops under a transtensive stress field instead of pure extension (Crider & Pollard, 1998). The background stress field around the Lake Natron has been estimated from the focal mechanisms of past earthquakes (Delvaux & Barth, 2010; the World Stress Map available online at <http://www.world-stress-map.org>). Those studies indicate a pure extension stress regime toward NNW–SSE around the Lake Natron. The NNW–SSE axis is consistent with the orthogonal direction

of the main shock strike direction during the 2007 event. Moreover, Delvaux and Barth (2010) and the World Stress Map indicate ENE–WSW pure extensive stress field in the Lake Manyara region, which is located 50 km to the south from the 2007 Natron rifting event area. The stress field estimated from seismological studies, however, indicates seismotectonic stresses, and the stress field can change at the other depths than the depth of the employed hypocenters. It is likely that the existence of a microplate or magma intrusion can build up a three-dimensionally complicated stress field. As shown in the slip distribution in Figure 6, the strike–slip is dominating at the shallower depth, suggesting the transcurrent stress regime. Meanwhile, it is well-known that the shallowest zone of the crust exhibits a velocity-strengthening tendency in the friction parameters of the rate-and-state dependent friction law, meaning the absence of seismic slip and the presence of aseismic slip (Scholz & Contreras, 1998). In other words, it should be noted that we cannot infer a true stress regime at the shallowest depths from seismological studies, no matter what type of stress fields are dominant. Thus we may claim that this study is the first to have confirmed the transtensive stress regime at shallower depth around the Lake Natron by the detection of the aseismic strike–slip based on the InSAR data. Although Wright et al. (2006) suggested that dike intrusion is essential to form the along-axis segmentation, and we do not dispute its importance, our detection of significant strike–slip at shallow depth is a direct evidence for the presence of transtensive stress that is necessary to generate the along-axis segmentation like relay zone (transfer zone). We consider that the dike intrusion could contribute to generate the three-dimensionally complex stress distributions. Since our dike opening model sets a kinematic displacement boundary condition instead of stress boundary condition, we should note that the stress axis around the study area does not have to coincide with the dike opening direction. The relay ramp is known to form between antithetic normal faults like graben structure (Amer et al., 2012; Tesfaye et al., 2008). As the relay ramp develops, a fracture can be built up along the direction orthogonal to the fault strike direction, generating new normal faults as transfer faults (Commins et al., 2005; Xu et al.,

2011). Such fractures are also observed at the Northern Lake Rukwa (Chorowicz, 2005). While we do not include it in the source model of this study, we can identify such discontinuities in the azimuth offset observation as indicated by the red dashed line (Figure 3). We consider that those discontinuities would also be the evidence for the horizontal motion of the subsiding region. The observed aseismic slip may also have an important implication for generation of earthquake swarm (Lohman & McGuire, 2007; Takada & Furuya, 2010; Wicks et al., 2011). Earthquake swarm is often attributed to fluid or magma intrusion, and it is apparent that such an intrusion occurred during our studied period. However, besides the dike intrusion process, aseismic slip has been proposed as another possible driver of swarm episode. We may regard the detected aseismic strike–slip as another evidence for the proposed swarm mechanism.

Chapter 4

Along-Rift Horizontal Displacement on Graben Subsidence during the 2005-2010 Afar Dike Intrusion Episode Detected by PALSAR-1 Data

The contents in this chapter are preparing to submit to the *Journal of African Earth Sciences*

Himematsu, Y., M. Furuya, Rift-parallel block-like motion on the graben floor during the 2005-2010 dike intrusion episode, *in preparation*.

Chapter 4. Along-rift horizontal displacement on graben subsidence during the 2005-2010 Afar dike intrusion episode detected by PALSAR-1 data

4.1 Introduction

Afar is a triple junction of the subaerial divergent plate boundaries between Arabian, Somalian and Nubian plate (Figure 4-1) (McKenzie et al., 1970). While the geodetic observations indicate the largest steady spreading along the East African Rift (Kreemer et al., 2003; Stamps et al., 2008), dike intrusion episodes intermittently occur along the continental rift zones, accompanying significant ground displacement (Wright et al., 2006; Calais et al., 2008). The 2005-2010 Afar rifting episode was one of the long-lasting dike intrusion episodes, which took place along the Manda-Hararo Dabbahu magmatic segment that is located Nubian-Arabian plate boundary (Figure 4-1). Previous studies have indicated the three dimensional (3D) displacements due to the September 2005 event from satellite synthetic aperture radar (SAR) and optical images (e.g., Wright et al., 2006; Grandin et al., 2009, 2010; Hamling et al., 2009). Spatial pattern of the derived crustal deformation showed an archetypical graben structure; the uplifted graben shoulders were extending from NE to SW, and the narrow graben floor subsided by up to 3 m. Those displacement data were helpful to understand the kinematics of the dike intrusion (Wright et al., 2006; Grandin et al., 2009, 2010b; Hamling et al., 2009). Ground displacements of the subsequent events after June 2006 (Events 2-14) were also derived by interferometric SAR (InSAR) data. However, we should keep in mind that the displacement data over the graben floor were lacking due to the phase decorrelation problem of the C-band ENVISAT data (Hamling et al., 2009; Hamling et al., 2014); we follow Hamling et al. (2009) and Wright et al. (2012) for the numbering of the sequential events, and the September 2005 event is Event 1.

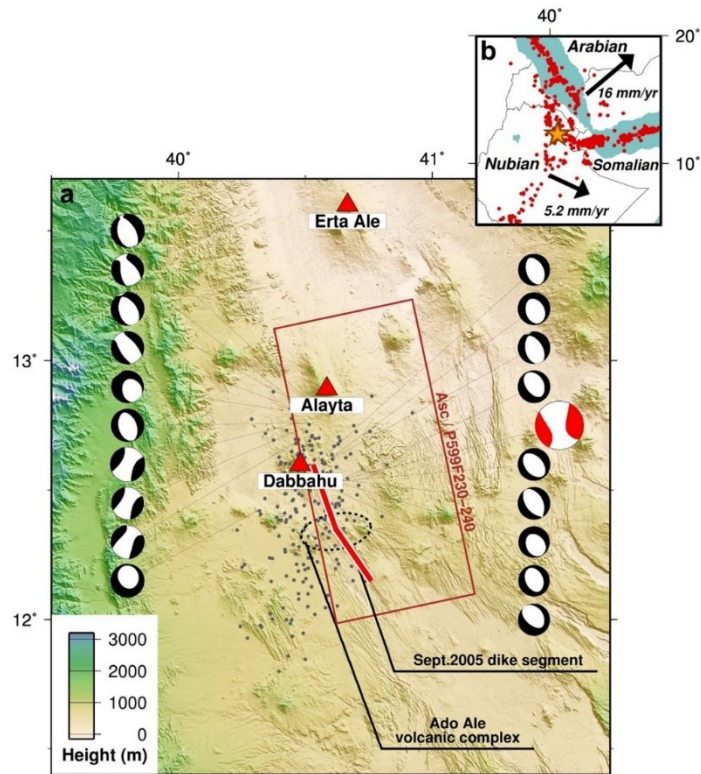


Figure 4-1. Study area in this chapter. a) Enlarged map, Grey dots are the location of epicenters during 2005-2010. Beachballs are focal mechanisms of each earthquake that are greater than M 4.9. Red one is focal mechanism of the mainshock during the episode (M 5.5, 24 September 2005). Red triangles indicate the location of active volcanoes around the study area. Red rectangular shows the PALSAR-1 footprint we processed in this chapter. The satellite flight direction is from SSE to NNW direction. The observation conducted right-looking geometry. b) Location map around the Afar basin. Red dots are the location of epicenters during 1960-2010. Star indicates the study area in this chapter. Black arrows represent direction of relative plate motion in a Nubian-fixed reference frame. The information of earthquake is derived from USGS catalog.

Some previous studies have presented 3D displacement fields associated with the rifting events since 2006 (Grandin et al., 2010; Hamling et al., 2014; Pagli et al., 2014). However, they were derived by interpolating the displacement data outside the graben floor into the data-missing graben floor. In other words, it is still uncertain if graben was simply subsiding without any horizontal

displacements. Meanwhile, Himematsu and Furuya (2015) reported significant rift-parallel block-like horizontal motion at the subsiding graben floor in the 2007 Natron rifting event by analyzing L-band PALSAR (Phased-Array type L-band Synthetic Aperture Radar) images acquired from the ALOS (Advanced Land Observation Satellite). Those displacements were explained by strike-slips on the two graben-bounding faults, which, to our knowledge, have never been reported in any previous rifting events. Very few strike components in seismological data and a gap of seismic and geodetic moment release suggested that these strike-slips were aseismic. No similar rift-parallel horizontal displacements were, however, reported in the 2005-2010 Afar rifting event, and it remains uncertain how frequent and universal such rift-parallel movements are. Here we reexamine the crustal

Table 4-1. Timing and volume of intruded magma during the 2005-2010 Afar dike intrusion sequence.

Event #	Date	Volume of magma intrusion [km³]
1	September 2005	2.5
2	June 2006	0.12
3	July 2006	0.042
4	September 2006	0.088
5	December 2006	0.058
6	January 2007	0.037
7	August 2007	0.048
8	November 2007	0.15
9	March 2008	0.088
10	July 2008	0.066
11	October 2008	0.17
12	February 2009	0.077
13	June 2009	0.046
14	May 2010	0.08?

Date and volume of intruded magma in each event are acquired from Hamling et al. (2009) and Wright et al. (2012). The magma intruded volume during May 2010 event is not presented accurately.

deformation data acquired from PALSAR data to see if the rift-parallel movements were accompanied with the 2005-2010 Afar rifting events; the details on the PALSAR images are shown in Table 4-1.

Moreover, regarding the Afar dike intrusion episodes, no observation results based on PALSAR images have been reported so far. The advantage of L-band PALSAR over shorter wavelength data is its higher coherence even if the temporal separations are long, which allows us to monitor long-lasting displacements. To reduce phase decorrelation problem, we applied an intensity-based pixel tracking technique (Strozzi et al., 2002), which could provide us with robust data rather than InSAR.

Table 4-2. PALSAR-1 dataset in this chapter.

Data #	Acquisition date (dd.mm.yyyy)	B_perp [m]
1	12.06.2007	0
2	12.12.2007	778.2
3	29.04.2008	1420.8
4	14.09.2008	-498.3
5	15.12.2008	-387.8
6	02.08.2009	-140.3
7	17.09.2009	606.6
8	05.05.2010	602.6
9	20.06.2010	858.5
10	05.08.2010	264.1

Processed PALSAR data and each perpendicular baseline. Ten L-band radar images are obtained from ascending track (Path: 599, Frame: 230-240). Perpendicular baselines (B_perp) are in reference of Data #1. Image cover area is shown in Figure 4-1.

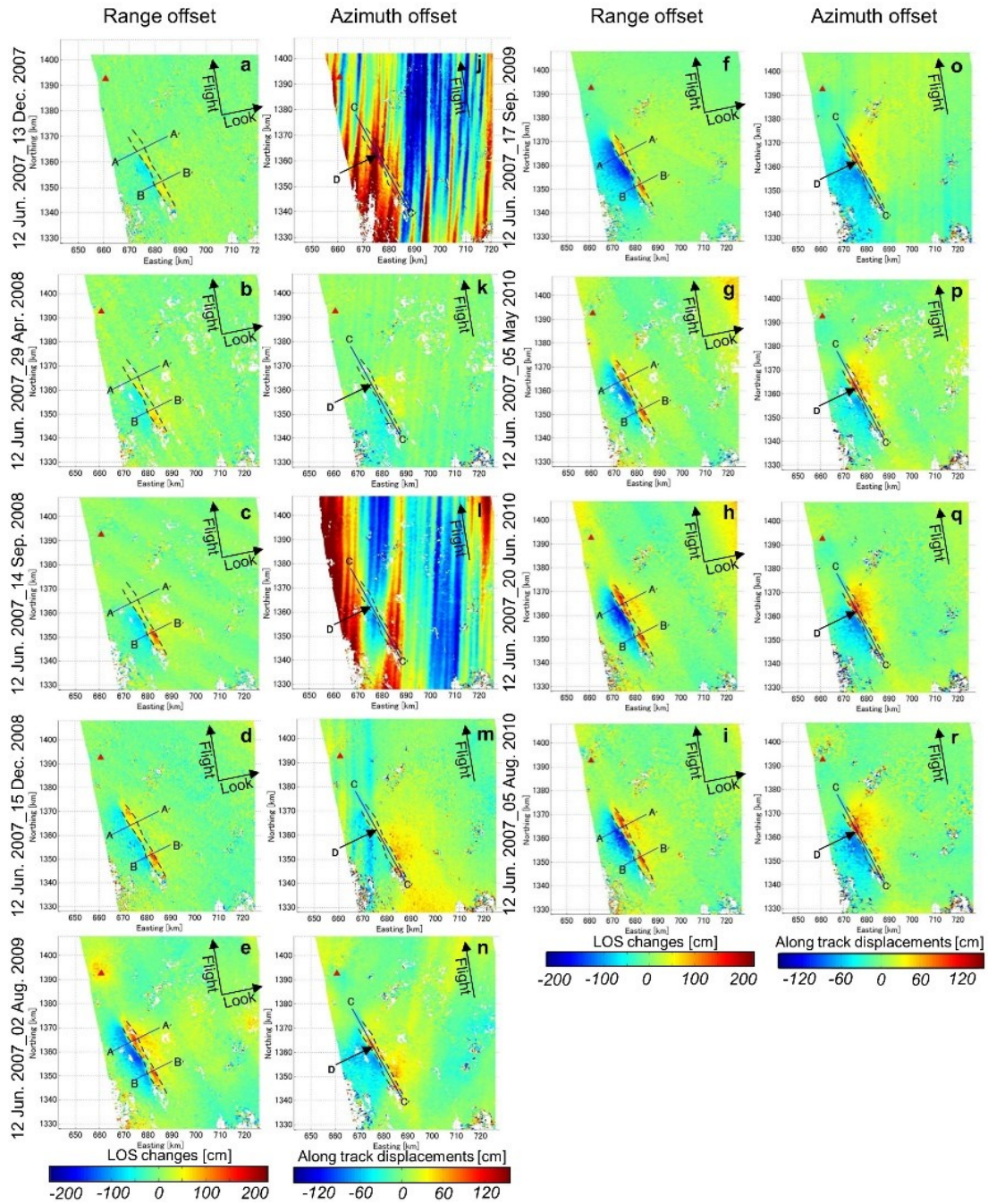


Figure 4-2. PALSAR -1 pixel-tracking data for the dike intrusion sequence in Afar. Cumulative range (a-i) and azimuth offset (j-r) from 12 June 2007. Cross sections of range offsets across north and south part of a graben (profiles A-A', B-B') are shown in Figures 4-4b and 4-4c. Cross sections of azimuth offsets along the graben floor (profile C-C') are shown in Figure 4-4d. Point D (Black arrow) shows a point which is a maximum positive signal in Figure 4-2r. Black dashed lines show top locations of two faults in our model.

4.2 SAR data and processing method

Pixel tracking technique can provide us with two independent displacement data sets that are sensitive not only to the line-of-sight direction (range offset) but also to the along-track direction (azimuth offset) (Jonsson et al., 2002; Kobayashi et al., 2009; Simons et al., 2002; Tobita et al., 2001). Our processed images were acquired from only ascending track and thus did not allow us to completely resolve the 3D displacements. However, the range and azimuth offset data in the present satellite track can well constrain the displacement field, because the satellite flight direction is nearly in parallel with the rift-axis, and the range and azimuth offsets are sensitive to such displacement that are perpendicular and parallel to the rift-axis, respectively. Highly coherence over longer temporal separation in the L-band SAR data is even more important and helpful to robustly constrain the displacements. Because ALOS/PALSAR was launched in January 2006 and the images became available since 2007 in this study area, we cannot quantify the surface displacements due to the earlier events in 2005-2006. For the PALSAR data processing, we used the commercial GAMMA software (Wegmüller & Werner, 1997). In performing pixel tracking technique, we set the search window size of 64×192 pixels for range and azimuth directions with sampling interval of 16×36 pixels. Artificial error due to the topography were reduced by using the 3 arc-second SRTM DEM (Shuttle Radar Topography Mission digital elevation model) (Farr et al., 2007).

While both the range and azimuth offset indicate that the displacements are distributed over the ~40 km-long graben structure (Figures 4-2 and 4-3), the azimuth offset shows positive signal (toward N349°E) greater than 1 m over the northern half of the graben floor, and no such positive signals can be observed outside the graben floor (Figures 4-2 and 4-3). Time-series of pixel tracking results are shown in Figure 4-2 and the details of the dataset are indicated in Table 4-2. Also, it is

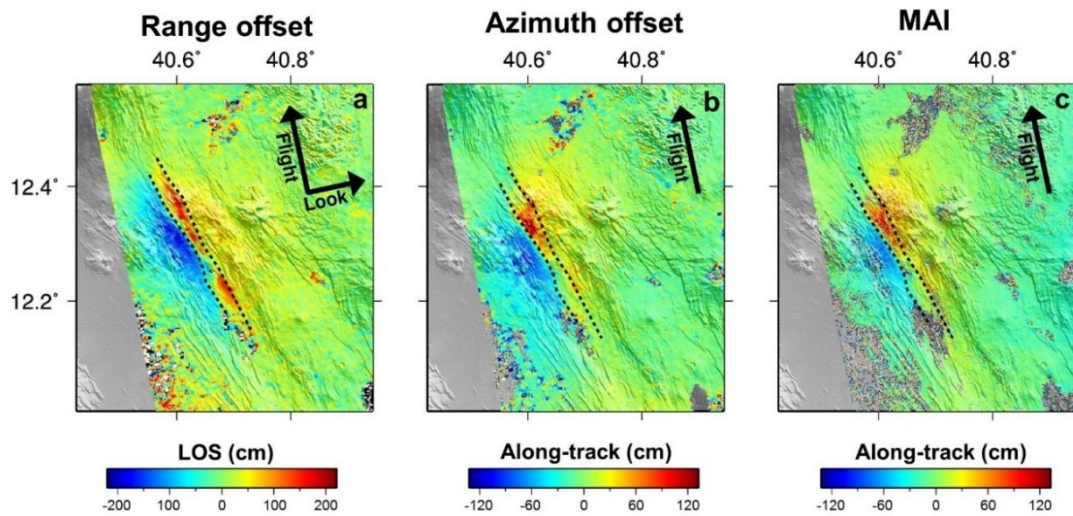


Figure 4-3. PALSAR-1 pixel tracking and MAI from 12 June 2007 to on 5 August 2010. (a) Range offset, (b) azimuth offset, and (c) MAI data. Positive signals indicate LOS lengthening in range offset and horizontal displacements along the satellite flight direction (NNW), respectively. Dotted lines traced signal discontinuities in the pixel tracking. Arrows indicate the direction of radar irradiation (Beam) and satellite flight direction (Flight), respectively.

important to note that the offset fields between the graben floor and the shoulders are clearly discontinuities. Namely, the graben floor moved along the satellite flight direction independently from both sides of the graben. Those positive signals in the azimuth offset implied that the rift-parallel horizontal movements did indeed occur as observed during the 2007 Natron event. We confirmed that multiple aperture interferometry (MAI) (Bechor & Zebker, 2006)), which is a phase-based method to detect horizontal displacements along the satellite tracks, also indicated the same signals as the azimuth offset data (Figure 4-3c). Thus, the rift-parallel horizontal displacements at the graben floor were indeed occurring at least since 2007. Given the presence of discontinuities in both the range and azimuth offsets across the boundaries between the graben floor and both sides, we can easily rule out a possibility that the rift-parallel motion could be caused by the volume changes of a magmatic source. We will further discuss the mechanisms of the movement in the following sections.

Casu and Manconi (2016) have shown short-baseline time-series of pixel tracking data, using C-band ENVISAT/ASAR dataset during the post-2005 rifting event. Although they did not insist on the rift-parallel motion at the graben floor, we can again clearly identify ~80 cm of northward rift-parallel movements in the displacement velocity from 2006 to 2010 (see Figure 6b in Casu & Manconi, 2016). Namely, the rift-parallel motion at the graben floor during the post-2005 rifting event was confirmed by both L-band and C-band data. Meanwhile, in view of the 3D displacement for the largest event in September 2005 shown by Wright et al. (2006) and Grandin et al. (2009), there appear few rift-parallel displacements.

In order to examine if there is any relationship between the rift-parallel movements and the intruded magma volume, we compared the temporal evolution of the azimuth offset data with the estimated volume of magma injection at each rifting event by Hamling et al. (2010) and Wright et al. (2012) (Figure 4-4a); our fault model shown later is derived from cumulative displacements. In view of each azimuth offset profile along the rift-parallel graben floor (Figure 4-4d), the temporal evolution of azimuth offset does not show clear correspondence to the timing of magma intrusion. However, there appears to be some lagged correlations with a delay time of ~6 months or more, which might be consistent with the absence of the rift-parallel motion during the first largest Event 1 if the rift-parallel motion took place with significant delay (Grandin et al., 2009; Wright et al., 2006).

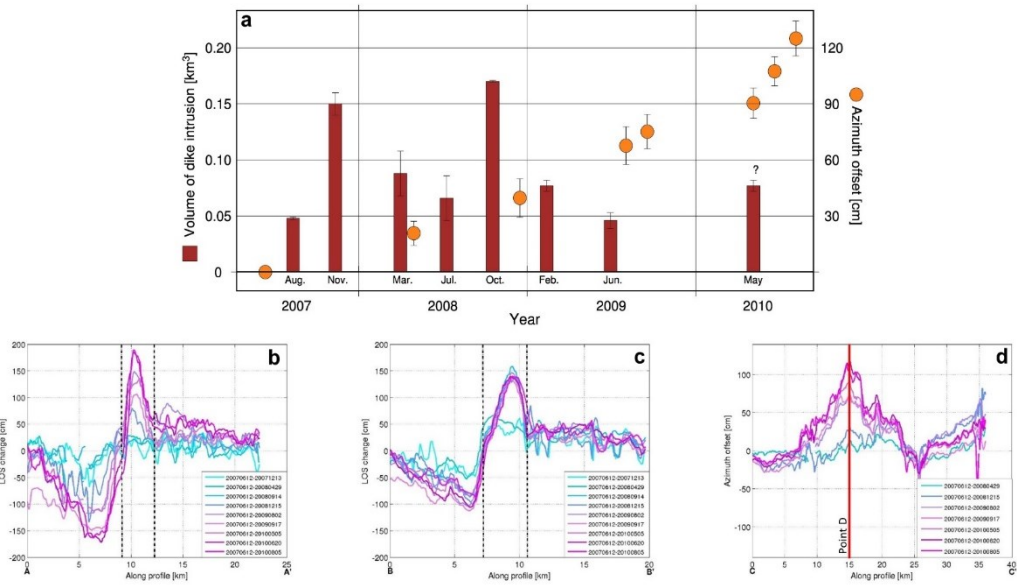


Figure 4-4. Temporal evolution of cumulative azimuth offset and its cross-sections of pixel tracking. (a) Volume of dike intrusion and temporal evolution of azimuth offset. Left-vertical axis shows volume of magma intrusion (Red bars) whose data are shown in Hamling et al. (2009) and Wright et al. (2012). Right-vertical axis shows azimuth offset (Orange circles) at a point that indicate the maximum positive signal at a graben floor (Point D). Vertical error bars represent the root-mean-squares at the non-displacement field in each of the results. (b-d) Temporal evolution of the range and azimuth offset along each cross-section in Figure 4-2. Black dashed lines are the location of the graben-bounding fault.

4.3 Fault source model

We have derived a fault slip distribution model in an elastic half space that can explain the cumulative displacements from June 2007 to August 2010 (Figure 4-5). We applied quad-tree method to reduce the number of the data (Figures 4-5a and 4-5d). The slip and tensile opening distribution model consist of two graben-bounding faults and a dike segment (Figures 4-5g-l), which were constructed by triangular dislocation elements (Furuya & Yasuda, 2011; Meade, 2007). A Poisson's ratio of 0.25 and a rigidity of 30 GPa were assumed. In deriving the slip and tensile opening on each segment, we constrained both the slip direction and the smoothness of the inferred slip and opening distributions (Furuya & Yasuda, 2011; Himematsu & Furuya, 2015). Standard deviations of each component were

derived by using iterative inversions with random noise (Wright et al., 2004) (Figure 4-6). The slip distributions revealed that the strike-slip mostly concentrated near the surface, whereas the peak of the strike-slip (1.1 m at maximum) is located at a depth of 2 km on the west-dipping fault. Cumulative geodetic moment release of the strike components alone turned out to be 1.61×10^{18} Nm ($M_w = 6.07$), while the total geodetic moment release, which includes both normal faulting and tensile opening, is 1.82×10^{19} Nm. It turns out that even the strike-slip contributions in the geodetic moment release alone were five times as great as the cumulative total seismic moment release (3.3×10^{17} Nm) during the observation period (Belachew et al., 2013). Considering that very few strike-slip earthquakes were detected by local seismic networks, the gap of those moment releases suggested that these strike-slips were aseismic. We checked that synthetic displacements could explain both observation results with root-mean-square (RMS) misfits of 12.9 cm and 7.0 cm for range and azimuth offset, respectively.

Some previous models derived from the ENVISAT/ASAR InSAR data showed ~ 2.5 m opening even during each individual event (Grandin, Socquet, Doin, et al., 2010; Ian J. Hamling et al., 2010). In contrast, our tensile opening is estimated to be 2.3 m even for the cumulative displacements, much smaller than previous estimates. We should keep in mind, however, that both Grandin et al. (2010a) and Hamling et al. (2010) did not include any fault segments but only tensile opening in their models, because the missing data over the graben floor did not let them to include the contribution by fault slip. On the other hand, other models by Ebinger et al. (2010) and Hamling et al. (2009) included not only tensile opening but also fault segments and provided us with the cumulative opening from 2005 to 2009 (Ebinger et al., 2010; Hamling et al., 2009). The accumulation diagram by Ebinger et al. (2010) indicates ~ 2.5 m cumulative opening along the southern part of the Manda-Hararo Dabbahu magmatic segment during 2007-2009, which is nearly consistent with our estimated opening distribution. We consider that such models including only dike segments will overestimate an opening

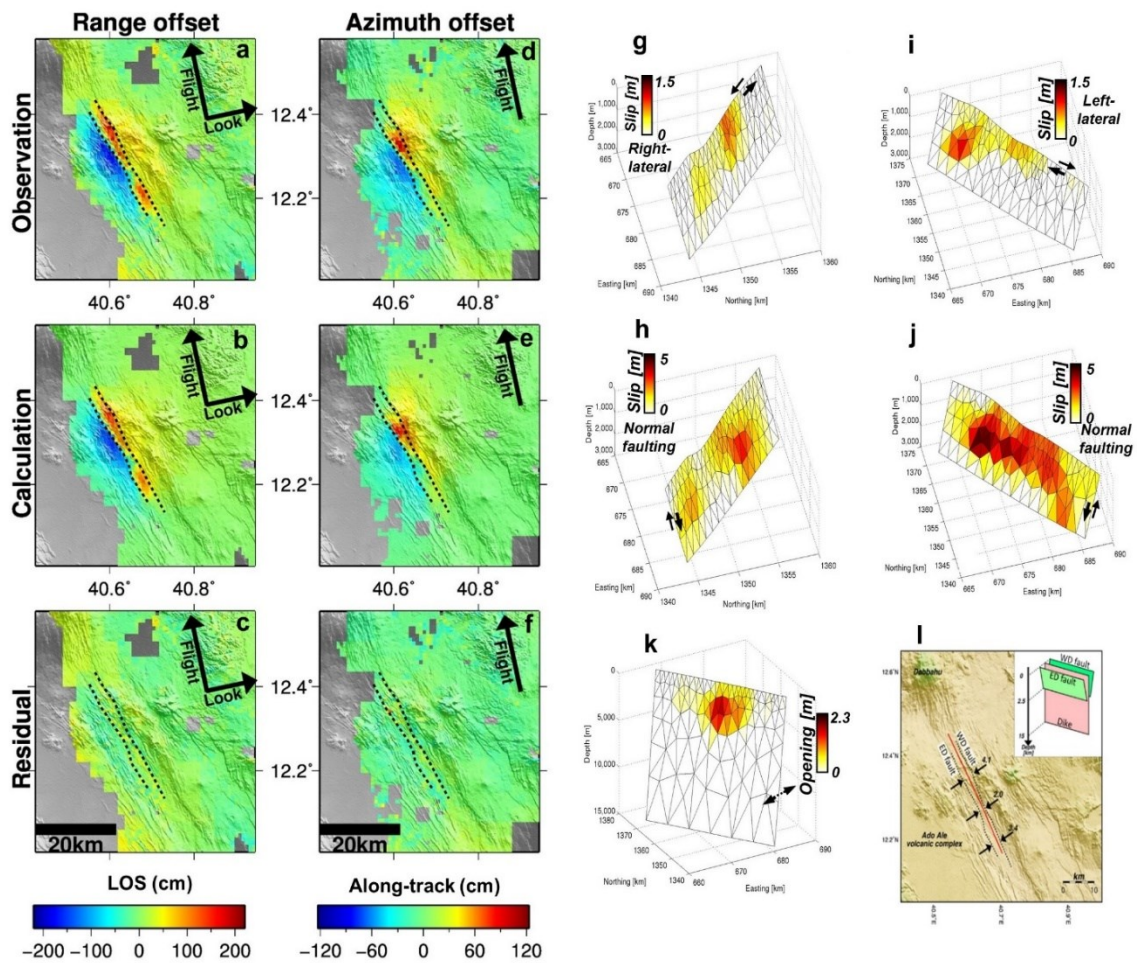


Figure 4-5. Our optimal elastic model for the PALSAR-1 pixel-tracking data. Range offset observation (a), calculation (b) and misfit residual (c). Azimuth offset observation (d), calculation (e) and misfit residual (f). Slip distributions on each fault segment. Left-lateral strike-slip (g) and normal slip (h) on the east-dipping fault. Right-lateral strike-slip (i) and normal slip (j) on the west-dipping fault. (k) Dike opening distribution. (l) Overview and geometry of the fault model. Black and red lines indicate top locations of the two faults and the dike segments, respectively. Numbers with black arrows are graben widths at each point. Inset shows schematic image of fault model geometry.

volume, probably the observed significant displacements were entirely attributed to the tensile opening despite the presence of displacements due to fault segments.

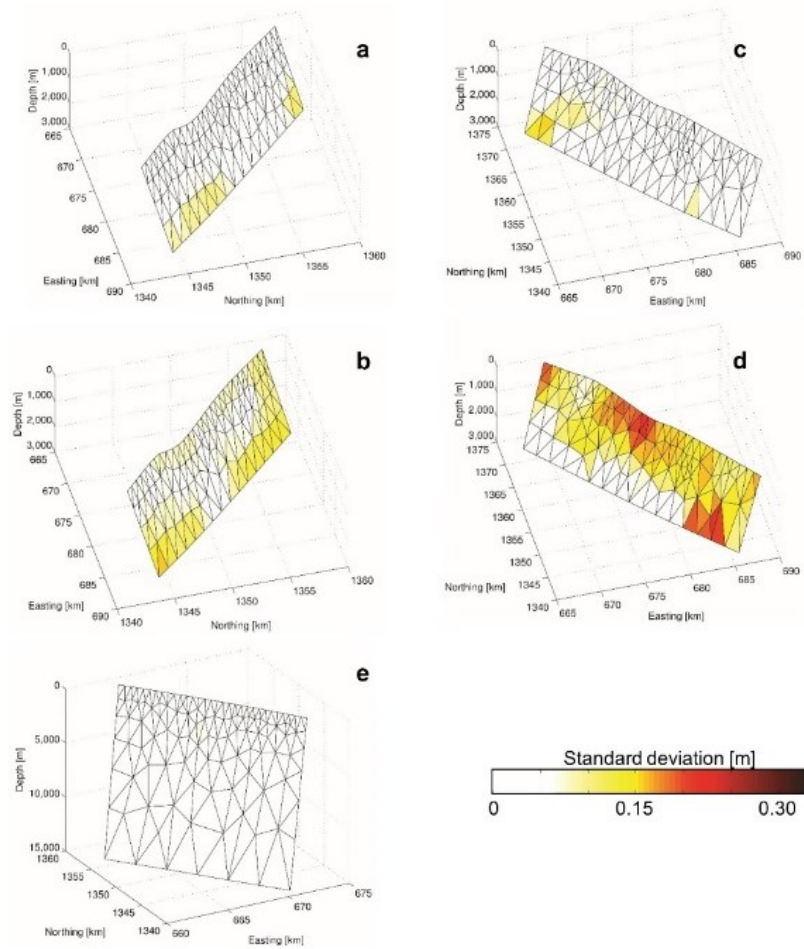


Figure 4-6. Standard deviations of faulting and opening distributions. Slip error was calculated by 200-times iterative inversion with random noise. Standard deviations of left-lateral strike-slip (a) and normal slip (b) on east-dipping fault, that of right-lateral strike-slip (c) and normal slip (d) on west-dipping fault, and that of dike opening (e).

We computed Coulomb stress changes (ΔCFF) caused by tensile opening upon the two graben-bounding faults in order to assess if the dike intrusion promoted the inferred fault slip (Figure 4-7) (King et al., 1994). Positive stress changes that correspond to unclamping are concentrating at shallower depths (0-1.5 km) on each receiver fault. The distributions of positive stress changes are consistent with the inferred strike-slip distributions, but a peak of strike-slip located at a depth of 2 km where slight negative stress changes were indicated. Thus, the stress changes due to dike opening did

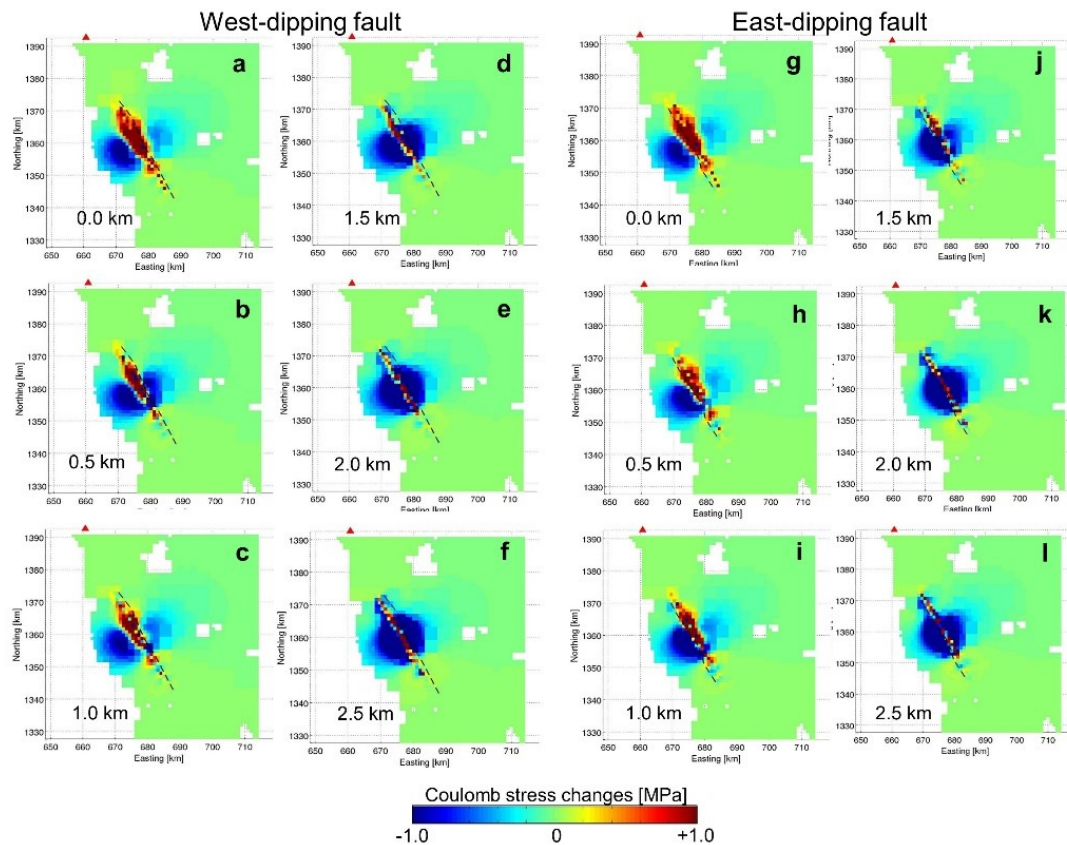


Figure 4-7. Coulomb stress changes due to dike opening in our model for each receiver fault. Horizontal slices of stress changes associated with dike opening inferred from our model on west-dipping fault (a-f) and east-dipping fault (g-l). Depths of slice are shown at bottom-left corner of each panel. Positive stress changes indicate promoting fault slip on receiver fault. Black dashed lines show top locations of each receiver fault. Red triangles located at the Dabbahu volcano.

not prevent the aseismic strike-slip in the shallower part, but the stress changes were unlikely to be a driver of the rift-parallel motion.

4.4 Discussion

4.4.1 Aseismic slip consistent with rate-and-state friction law

Our pixel tracking data and the fault model indicate that the observed displacements are mostly caused by aseismic processes, because cumulative seismic moment release can only explain less than 2% of the geodetic moment release. Aseismic slip plays a role in strain accommodation during rifting events

(Calais et al., 2008), and can be one of the key drivers for earthquake swarms at volcanic or geothermal area including divergent plate boundaries (Lohman & McGuire, 2007; Vidale & Shearer, 2006; Wicks et al., 2011). According to the rate-and-state dependent friction law, aseismic slip tends to occur at shallower depths of crust, in which stable slip tends to take place (Dieterich, 1979; Ruina, 1983; Toda & Stein, 2002). The slip tendency is consistent with our slip distribution estimates, which indicate the strike-slip patches are mostly located at shallower depths than the normal faulting patches (Figure 4-5).

4.4.2 Any relevance to strike-slip earthquakes along divergent plate boundaries?

Even divergent plate boundaries under an extending stress regime include potential for causing strike-slip earthquakes. Most accepted mechanisms of strike-slip earthquakes under extensive stress regime are bookshelf faulting (Green et al., 2014; Mandl, 1987; Tapponnier & Courtillot, 1990) and dog-bone seismicity (Toda et al., 2002). The observed rift-parallel displacements, however, look like block-like uniform movement of the graben floor and cannot be explained by either bookshelf faulting or dog-bone seismicity even if those mechanisms worked by aseismic processes.

4.4.3 Block-like motion of graben floor as a response to horizontal flow of plume material?

The elastic fault model can successfully explain the rift-parallel block motion but does not clearly tell the dynamical mechanisms. We may interpret that the rift-parallel block-like motion of the graben floor would represent the passive advection of the upper crust that is coupled with the horizontally underlying flow of sill; the sill would be deeper than 5 km in light of the depth tensile opening (Figure 4-5). Although sill intrusion has been incorporated as a horizontally lying mass to reproduce uplift signals (Fialko et al., 2001), we do not observe any uplift signals but horizontal movements that were kinematically explained by shallow aseismic strike-slip in our model. In the framework of elastic modeling, however, we can no longer express the effects of flowing sill that can

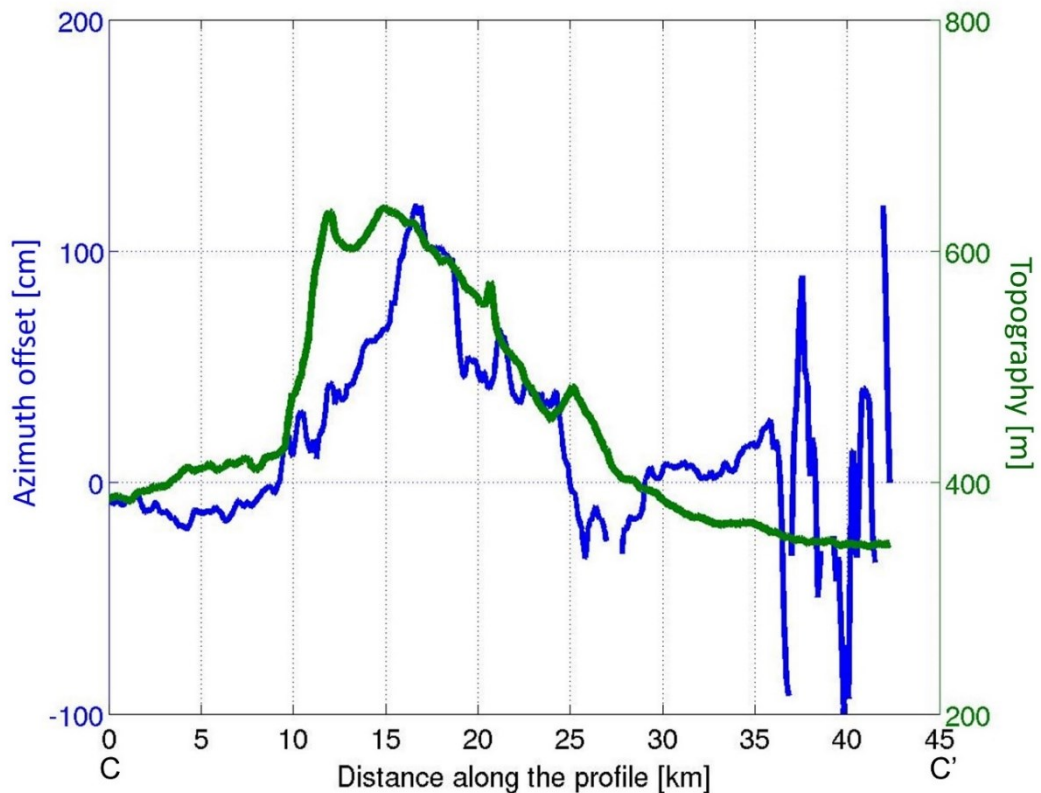


Figure 4-8. Cross sections of topographic height and cumulative azimuth offset from 12 June 2007 to 5 August 2010 along the profile C-C' in Figure 4-2. Green and blue lines indicate topographic height and azimuth offset from 12 June 2007 to 5 August 2010 along the C-C', respectively.

viscously couple with the overlying crust. Meanwhile, in a recent thermo-rheological geodynamic model that aims to reproduce the presence of both active and passive rift zones around the Tanzanian craton in central East African Rift (EAR) (Koptev et al., 2015), similar rift-parallel displacements have been demonstrated during the dynamic topographic evolution. Although there are significant gaps in terms of both spatial- and temporal-resolutions between the thermo-rheological geodynamics model and our geodetic observations, and the model does not yet reproduce the episodic processes such as rifting, the simulated rift-parallel displacements could be essentially what we observed geodetically. A key simulated process relevant to the geodetic observations could be a channelized flow of plume material, which is a deflection of the plume head at the cratonic keel (Albers & Christensen, 2001;

Sleep, 1997). The lateral channelized plume flow can generate narrow strain localizations and induce slow surface movements along rift axes (Koptev et al., 2015). Around Lake Natron in the simulation results, the surface velocity indicated southward horizontal movements on the order of a few millimeters per year, which is consistent with a direction of the rift-parallel displacements in the 2007 Natron rifting episode (Himematsu & Furuya, 2015).

A seismic tomography results showed low velocity zones at the southern edge of Afar, where we may expect the upwelling mantle plume (Bastow et al., 2008). A Moho depth distribution along the western-edge of Afar also indicates that crustal thickness becomes thinner toward NNW (Hammond et al., 2011). If the plume material flows along the rift axis in the western Afar, the plume material would form a channel toward NNW. The direction is also consistent with the rift-parallel movements over the graben floor in Afar. Assuming that the plume channeling causes along-axis surface velocity on the order of a few millimeter per year as in the numerical model over the central EAR, the amplitude of the rift-parallel displacements (~ 1 m) in Afar is largely consistent with the strain accumulated from an interval of rifting cycle (~ 400 years) (Ebinger et al., 2010; Grandin et al., 2010a) and the surface velocity. We may thus interpret the rift-parallel displacements in both Natron and Afar as caused by the channelized flow that would be also responsible for dike intrusion. In other words, rift-parallel block-like motion of graben floor might be absent under magma-poor passive rifting.

Chapter 5

Icecap and Crustal Deformation Associated with the 2014-2015 Bárðarbunga Dike Intrusion Episode Inferred from SAR Pixel Tracking

Some contents in this chapter submitted to *Journal of Geophysical Research: Solid Earth*

Himematsu, Y., F. Sigmundsson, M. Furuya (2018) Icecap and crustal deformation associated with the 2014 Bárðarbunga dike intrusion episode inferred from SAR pixel tracking, *Submitted*

Chapter 5. Icecap and crustal deformation associated with the 2014-2015 Bárðarbunga dike intrusion episode inferred from SAR pixel tracking

5.1 Introduction

Iceland is a subaerial part of the divergent plate boundary between the North American plate and the Eurasian plate with a spreading rate of 18-19 mm/yr in the N100-105°E direction (e.g., DeMets et al., 2010). Combination of both an oceanic spreading ridge and a mantle plume beneath the central Iceland leads to the formation of the complex divergent plate boundary (Figure 5-1). The divergent plate boundary in Iceland consists of several volcanic systems, some of which are covered with glaciers or icecaps. The Vatnajökull icecap, the largest icecap in Europe, covers some of the most active volcanic systems in central Iceland (Figure 5-1). Subglacial volcanic eruptions may induce lahars and floods due to ice melting as heat transfers from magma, that is known as “jökulhlaup” (Björnsson, 2003; Gudmundsson et al., 1997). Such jökulhlaups are one of the primary volcanic hazards in Iceland.

The central volcano of the Bárðarbunga volcanic system is one of the subglacial volcanoes under the Vatnajökull icecap, with a 10 km diameter caldera (Figure 5-1). In 2014-2015, a major dike intrusion episode occurred in the volcanic system. Seismicity propagated away from the Bárðarbunga caldera and a fissure eruption occurred at Holuhraun, 10 km north of the margin of the Vatnajökull icecap (Figure 5-1). Rectilinear propagation of seismicity and the fissure eruption suggested a migration of magma (dike) from a source beneath the Bárðarbunga caldera (Sigmundsson et al., 2015). The magma passed through pre-existing fractures which were formed during previous eruption episodes (Gudmundsson et al., 2016; Hjartardóttir et al., 2015; Pedersen et al., 2017; Ruch et al., 2016).

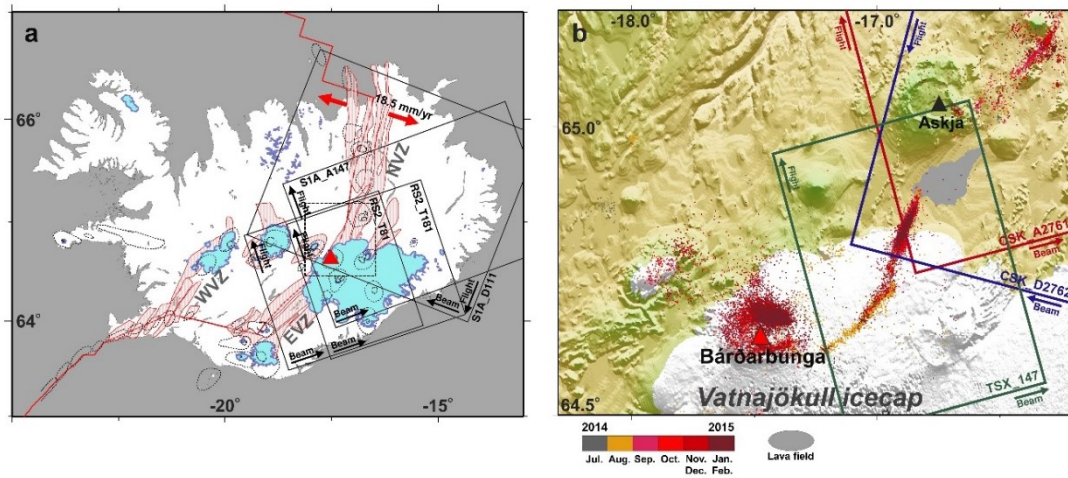


Figure 5-1. (a) Map showing the volcanic systems (dashed lines), calderas (combed lines), and associated fissure swarms (red transparent) in Iceland. Dashed box shows a region of Figure 5-1b. RADARSAT-2 (RS2) footprints are shown as solid black boxes. Outline data of glaciers or icecaps (light blue) is from the Randolph Glacier Inventory version 6.0 (GRI consortium, 2017). (b) Colored dots locate hypocenter locations from July 2014 to February 2015 (source, Icelandic Meteorological Office database, “<http://hraun.vedur.is/ja/viku/>”, last accessed on 17 October 2017). Footprints of Cosmo-SkyMed (CSK) and TerraSAR (TSX) images are shown as colored boxes. Each direction of satellite flight (“Flight”) and looking (“Beam”) are shown as arrows. Gray region marks the 2014-2015 lava field outline traced by comparing back scatter intensity between two CSK images which acquired before and after the episode (28 July 2014 - 6 March 2015 on Track D2762).

Both numerical and analog models suggested that variation in regional strain and gravitational potential due to topographic and ice mass load strongly contributed to the lateral magma propagation (Heimisson et al., 2015; Sigmundsson et al., 2015; Urbani et al., 2017). The main Holuhraun fissure eruption began on 29 August 2014 at the northern end of seismic propagation. The eruption continued until February 2015 and generated 84 km² lava field at the Holuhraun plain (Hjartardóttir et al., 2015; Pedersen et al., 2017; Sigmundsson et al., 2015). Overview flight observation reported that a minor eruption occurred between the main eruption site and the icecap edge on 5-7 September 2014 (Hjartardóttir et al., 2015).

Previous geodetic studies in the area have reported ground displacements associated with the dike intrusion. Satellite radar interferograms and GPS measurements revealed the displacements in WNW-ESE direction at north of the Vatnajökull icecap, which were caused by the dike intrusion as well as the evolution of the collapse of the subglacial Bárðarbunga caldera (Parks et al., 2017; Riel et al., 2015; Ruch et al., 2016; Sigmundsson et al., 2015). The direction of horizontal displacements is nearly consistent with that of far-field tectonic stress. However, as the focal mechanisms indicated, the observational data require some shearing along the dike (Ágústsdóttir et al., 2016; Parks et al., 2017; Ruch et al., 2016; Sigmundsson et al., 2015).

Ruch et al. (2016) applied SAR pixel tracking technique, and showed temporal evolution of the graben region, where conventional InSAR could not be used to detect the signal. Based on such data, Ruch et al. (2016) proposed that the evolution of graben formation almost ceased as of 6 September 2014, whereas the fissure eruption still continued. Ruch et al. (2016) did not use those signals over the icecap for their inversion model. Over the northernmost part of the dike outside the icecap, their inversion model indicated 4.5 m of opening and 1 m of left-lateral shearing across the dike. They proposed that both the opening and the shearing indicated the cumulative strain accommodation of oblique opening since a previous rifting episode in 1797. The digital elevation model (DEM) differences before and after the episode showed graben subsidence not only over the non-ice region but also above the icecap, indicating subglacial graben formation (Dirscherl & Rossi, 2018; Rossi et al., 2016). Airborne altimetry observations revealed up to 65 m of cumulative subsidence at the Bárðarbunga caldera due to the deflation of sill-like magma source and ring-faulting around along a caldera boundary (Gudmundsson et al., 2016). Although some interferograms with short-temporal baseline could detect icecap subsidence due to the caldera collapse, these data could

not reveal signals on icecap surface above the dike (Riel et al., 2015). After the fissure eruption ceased on February 2015, moderate-scale earthquakes ($M > 4$) have been observed along the Bárðarbunga caldera even by now, suggesting ongoing caldera uplift due to pressure increase, either renewed magma accumulation or viscoelastic relaxation (Sigmundsson et al., 2018).

Although direct evidence of a subglacial volcanic eruption has not been reported so far, the magma may have been implied to approach the bedrock surface. Observations on a seismic array show pre-eruptive tremor at depth shallower than 3 km, suggesting magma reaching close to the bedrock surface (Eibl et al., 2016). An airborne altimetry study detected three circle-like ice sink holes (ice cauldrons) along the dike path before the fissure eruption (Reynolds et al., 2017; Sigmundsson et al., 2015). The volume of ice cauldron is up to 18 million m³. A numerical model demonstrates that formation of at least one of the ice cauldrons required magma penetration into the ice (Reynolds et al., 2017). Chemical compositions in river water discharged from the icecap during and after the eruption show notable changes, suggesting subglacial eruptions before the Holuhraun eruption (Galeczka et al., 2016). Despite the indications of subglacial eruptions, no jökulhlaup has been reported. Stored subglacial meltwater would contribute to promote a hydraulic-driven speed-up of glacier flow speed due to decreasing friction between ice and bedrock (e.g., Iken & Bindshadler, 1986). At Vatnajökull, for example, meltwater derived from a discharging subglacial lake water facilitated an acceleration of basal sliding at the bottom of glacier as observed by InSAR in 1995-1996 (Magnússon et al., 2007).

The aims of this chapter are to infer subglacial crustal deformation associated with the 2014-2015 Bárðarbunga dike intrusion episode, and to evaluate the advantage of pixel tracking approach for mapping subglacial crustal deformation. To our knowledge, few studies have reported subglacial crustal deformations associated with the subglacial dike intrusion due to InSAR

decorrelation problems at ice surfaces. To achieve these aims, we employ primarily the satellite SAR pixel tracking data to infer the subglacial crustal deformation.

5.2 SAR data and processing method

5.2.1 Processing method and SAR dataset

Satellite synthetic aperture radar (SAR) is one of the remote sensing techniques to observe the Earth's surface characteristics in the form of back-scatter intensity and reflected microwave phase. The phase difference between two SAR images allow us to map the surface movement with high spatial resolution between data acquisition interval (Interferometric SAR; InSAR). The cross-correlation-based pixel tracking approach can detect surface movement as a local residual of image coregistration using SAR amplitude (Michel et al., 1999; Strozzi et al., 2002; Wright et al., 2006). The pixel tracking identifies local residuals within an arbitral window size (64-256 pixels) after two SAR images are precisely coregistered. The spatial resolution of pixel tracking is controlled by the window size. The approach is suitable for detecting meter-scale surface movement, such as glacier flow or large-scale crustal deformation e.g. associated with dike intrusion. Measurement error of the pixel tracking approach depends on the accuracy of image coregistration. Although we coregister two images with an accuracy of 1/10-1/20 pixels, some factors such as changing surface characteristics due to covering/melting snow on the icecaps cause decorrelation problems. Standard deviation of pixel trackings at stable regions can be regarded as a measurement of the accuracy (Kobayashi et al., 2009).

The window size and sampling interval for each dataset in this chapter are described in Appendix A. We discarded the cross-correlation of below 0.05 as missing data. We corrected for stereoscopic effect, an artificial elevation-dependent offset, in pixel tracking results (Kobayashi et al., 2009) using a digital elevation model from the advanced spaceborne thermal emission and reflection

radiometer (ASTER) satellite mission. All SAR data were processed by using GAMMA software package (Wegmüller & Werner, 1997).

We applied the pixel tracking approach to X-band COSMO-SkyMed (CSK), TerraSAR-X (TSX), and C-band RADARSAT-2 data (RS2) for detecting both icecap surface change and crustal deformation due to the subglacial dike intrusion in 2014. We also analyzed C-band Sentinel-1A (S1A) data to identify the temporal evolution of icecap surface changes during the 2014-2016 period (Appendix A). Spatial resolution of CSK and TSX data is 1-2 m, while the spatial resolution of RS2 data is 4-5 m (Appendix A). Spatial coverage of CSK and TSX images is, however, smaller than that of RS2 data (Figure 1). In this chapter, we refer to the period of 16 August-6 September 2014 as a co-diking period. Although the fissure eruption and the caldera collapse were continuing after the observation period, the crustal deformation associated with the dike intrusion mostly ceased when the dike propagation path had been formed (e.g., Ruch et al., 2016). Glacial isostatic adjustment (GIA) around the northernmost part of Vatnajökull icecap does not influence our measurements significantly and can be ignored, because GIA signal is less than 2-4 cm/yr for both horizontal and vertical components (Drouin et al., 2017).

Table 5-1. SAR dataset in this chapter and scale factors for correction of icecap signal

Satellite ^a	Orbit [Track] ^b	Date ^c	Data acquisition interval [Days] ^d	Scale factor [Days] ^e	Result ^f
Cosmo-SkyMed	Ascending [2761]	30 Jul. 2014 12 Sep. 2014	44	22	Figure 5-2
	Descending [2762]	13 Aug. 2014 23 Sep. 2014	41	44	Figure 5-2
TerraSAR-X	Ascending [147]	26 Jul. 2012 4 Sep. 2014 20 Nov. 2014	-	-	Figure 5-4
RADARSAT-2	Ascending [81]	1 Aug. 2014 18 Sep. 2014	48	35	Figure 5-6
	Ascending [181]	8 Aug. 2014 1 Sep. 2014	24	18	Figure 5-6

a Name of SAR satellite.

b Satellite flight direction. Ascending and descending means flight from SSE to NNW, and NNE to SSW, respectively.

c Date of observation of master and slave images.

d Intervals between data acquisition between master and slave images.

e Scale factor to correct the icecap signal in the co-diking signal. See section 5.2.4.

f Showing where we can see the result.

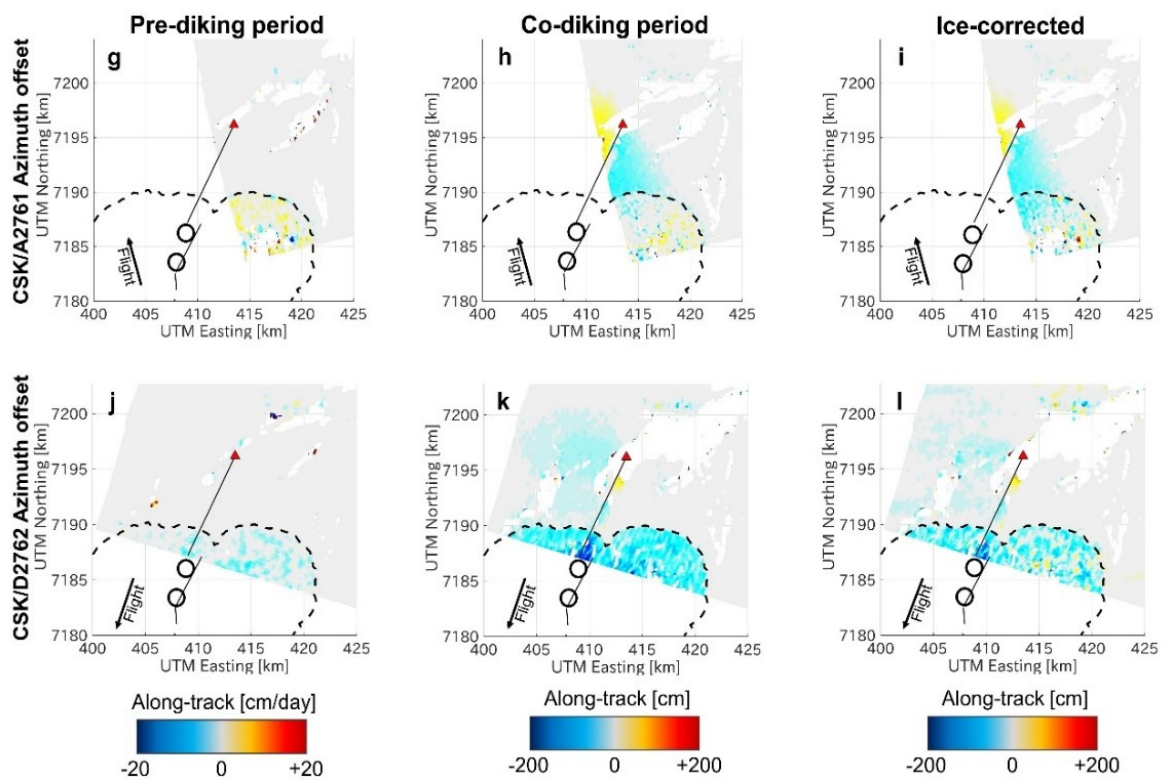
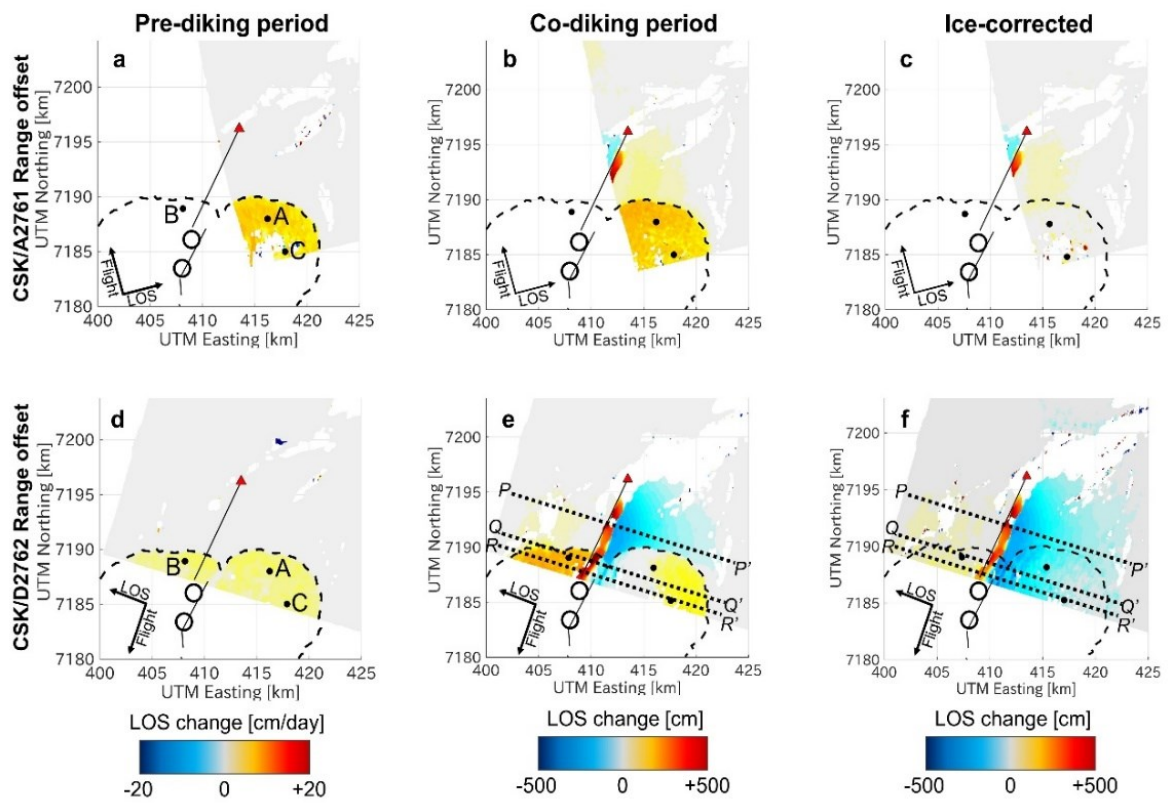


Figure 5-2. Pre- and co-diking Cosmo-SkyMed (CSK) pixel tracking results and ice-corrected signal. CSK range offset (line-of-sight: LOS) from ascending track (a-c, pre-diking: 28 June-30 July 2014, co-diking: 30 July-12 September 2014, ice-corrected) and descending track (d-f, pre-diking: 28 July-12 August 2014, co-diking: 12 August-23 September 2014, ice-corrected). CSK azimuth offset (along-track) from ascending track (g-i) and descending track (j-l), respectively. Dashed lines trace outline of the icecap. Solid black lines and circles are the locations of dike segments and ice cauldrons after Sigmundsson et al. (2015), respectively. Dotted lines show the profiles P-P', Q-Q', and R-R' displayed in Figure 5-7. Positive signal for azimuth and range offset indicates horizontal displacement toward satellite flight direction and line-of-sight change away from satellite, respectively. Red triangle denotes the Holuhraun main eruption site during the episode. Black dots are selected points of time series of ice surface change in Figure 5-9. Black dots with capital letters (A-C) locate observation points for time-series of icecap surface changes (Figure 5-9). Coordinates are in UTM zone N28.

5.2.2 Observation result during pre- and co-diking period

CSK pixel trackings during the pre-diking period reveal the steady-state of ice surface movement and no significant changes outside the icecap (Figures 5-2a, 5-2d, 5-2g and j, Table 5-1). CSK pre-diking range offset from both ascending and descending show positive signals on the icecap (Figures 5-2a and 5-2d). Positive line-of-sight (LOS) changes observed from both ascending and descending tracks indicate downward movement, possibly implying ice thinning. Rate of the LOS change on the icecap is about 15 cm/day in the ascending track and 5 cm/day in the descending track, respectively. Azimuth offsets during the pre-diking period indicate northward horizontal movement of the icecap because azimuth offsets are insensitive to vertical displacement and represent only the horizontal displacements along the satellite flight direction (Figures 5-2g and 5-2j). Both azimuth offsets show less than 5 cm/day on the icecap without any significant displacements at ice-free region except for decorrelation noise. The northward icecap movement can be explained by gravity-driven ice flow along topographic gradient at the region (Bjornsson & Einarsson, 1990). Using both range and azimuth offsets from ascending and descending track, we retrieved a three-dimensional (3D) movement field of the steady-state ice flow by solving over-determined least-square problem because the unit vector of displacement are independent (Tobita et al., 2001). Pre-diking 3D displacement

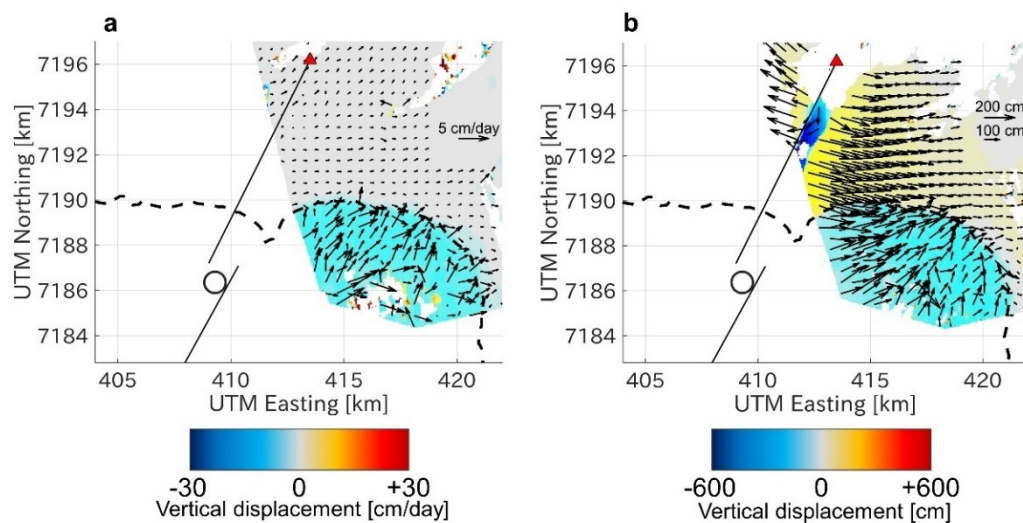


Figure 5-3. Pre-diking and co-diking 3D displacements inferred from CSK data. (a) Inferred pre-diking three-dimensional (3D) displacement rate. (b) Cumulative co-diking 3D displacement. Both are retrieved from Cosmo-SkyMed (CSK) range and azimuth offset from ascending and descending tracks. Arrows show the direction and amount of horizontal movement. Note that scales of horizontal movement are shown at the right-top in each result. Note that each color scales are different from each other. Dashed lines trace outline of the icecap. Solid black lines and circles are the locations of dike segments and ice cauldrons after Sigmundsson et al. (2015), respectively. Red triangle denotes the Holuhraun main eruption site during the episode. Coordinates are in UTM zone N28.

shows NNE horizontal movement (less than 5 cm/day) with downward movement (~ 20 cm/day) on the icecap during the observational period (Figure 5-3a).

Figures 5-2b and 5-2e show CSK range offset during the co-diking period. We regard a pair of 30 July 2014 – 12 September 2014 from ascending track and that of 12 August 2014 – 23 September 2014 from descending track as cumulative offsets during the co-diking period (Table 5-1). The pixel tracking data show signals of crustal deformation outside the icecap and icecap surface movement. The range offsets at ice-free region indicate graben formation associated with the dike intrusion as previous studies have already reported (Ruch et al., 2016). Positive signals along the dike indicate the subsidence; maximum positive offset is 5 m in CSK descending range offset (Figure 5-2e). We

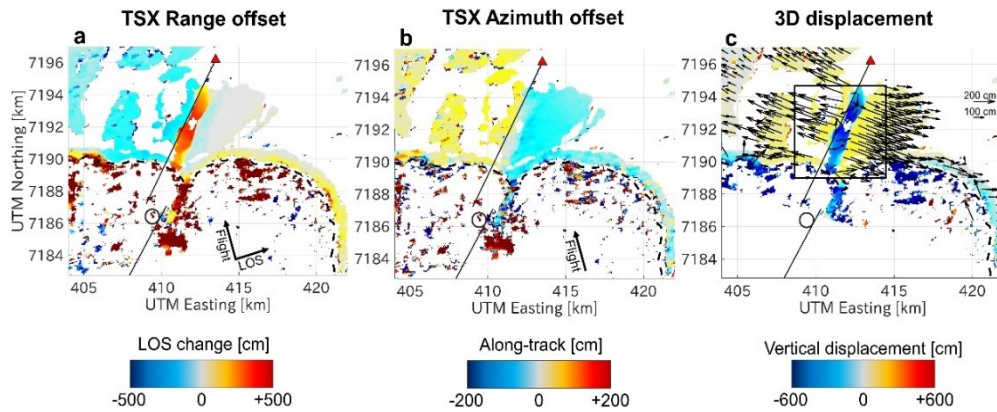


Figure 5-4. Stacked TerraSAR-X (TSX) pixel tracking and co-diking 3D displacement inferred from CSK and TSX dataset. Stacked TerraSAR-X (TSX) range offset (a) and azimuth offset (b) of 27 July 2012-4 September 2014 and 4 September 2014-20 November 2014. (c) Cumulative co-diking 3D displacement inferred from TSX ascending and CSK descending data. Black box shows the region of Figure 5-5a. Arrows show the direction and amount of horizontal movement. Scale of horizontal movement are shown at the right-top in the result. Dashed lines trace outline of the icecap. Solid black lines and circles are the locations of dike segments and ice cauldrons after Sigmundsson et al. (2015), respectively. Red triangle denotes the Holuhraun main eruption site during the episode. Coordinates are in UTM zone N28.

identified the maximum subsidence at ice-free region near the minor eruption site along the graben subsidence (Figure 5-5). CSK descending range offset reveals less than 50 cm at western half of graben flank and 1.5 m of negative signal at eastern half of graben flank (Figure 5-2e).

While the pre-diking range offset reveal only positive signal on the icecap (Figures 5-2a and 5-2d), the CSK co-diking range offset from descending track show negative signal on the icecap near the graben (Figure 5-2e). Negative signals of LOS change from right-looking descending track indicate eastward displacement and/or uplift. Thus, these negative signals imply icecap surface changes associated with subglacial crustal deformation. The descending range offset also indicates graben subsidence under the icecap because positive signal with signal discontinuities is detected even on the icecap. By contrast, we cannot find any signal variations across the icecap in the CSK co-diking

ascending range offset (Figure 5-2b).

The co-diking ascending azimuth offset shows about 1m of symmetric signal at the graben flanks (Figure 5-2h). Although there are little signal above the icecap, we find a clear offset discontinuity along the icecap edge. The co-diking descending azimuth offset shows very little signal at the graben flanks, because the observations are sensitive to displacements nearly parallel to the graben (Figure 5-2k). At the graben floor, we can identify ~ 1 m of positive offset at the northern half of graben subsidence and ~ 1 m of negative offset at the southern half of graben subsidence, that is, horizontal movement toward the minor eruption site at the graben floor.

The 3D displacements derived from both CSK ascending and descending data during co-diking period show not only crustal deformation of graben formation but also icecap surface change due to subglacial ground deformation (Figure 5-3b). At ice-free region, the 3D displacements reveal ~ 3 m of rift-perpendicular horizontal displacement with ~ 1 m of uplift at each graben flank, and ~ 5 m of subsidence with 1 m of SSW horizontal displacements at the graben floor. Although icecap surface far from the graben moves toward north, the co-diking 3D displacements represent eastward movement on the icecap near the graben. Due to the subglacial ground deformation, icecap horizontal displacements near the graben are larger than that far from the graben.

Figure 5-4 shows cumulative TSX pixel tracking between 26 July 2012 and 4 September 2014 and between 4 September 2014 and 20 November 2014 (Table 5-1). Although spatial resolution of TSX data is nearly the same as that of CSK data, the TSX pixel trackings are noisier than CSK pixel tracking because temporal baseline of the first TSX pair is over two years. Due to the decorrelation problems, the TSX data could not detect icecap surface displacement, while the TSX

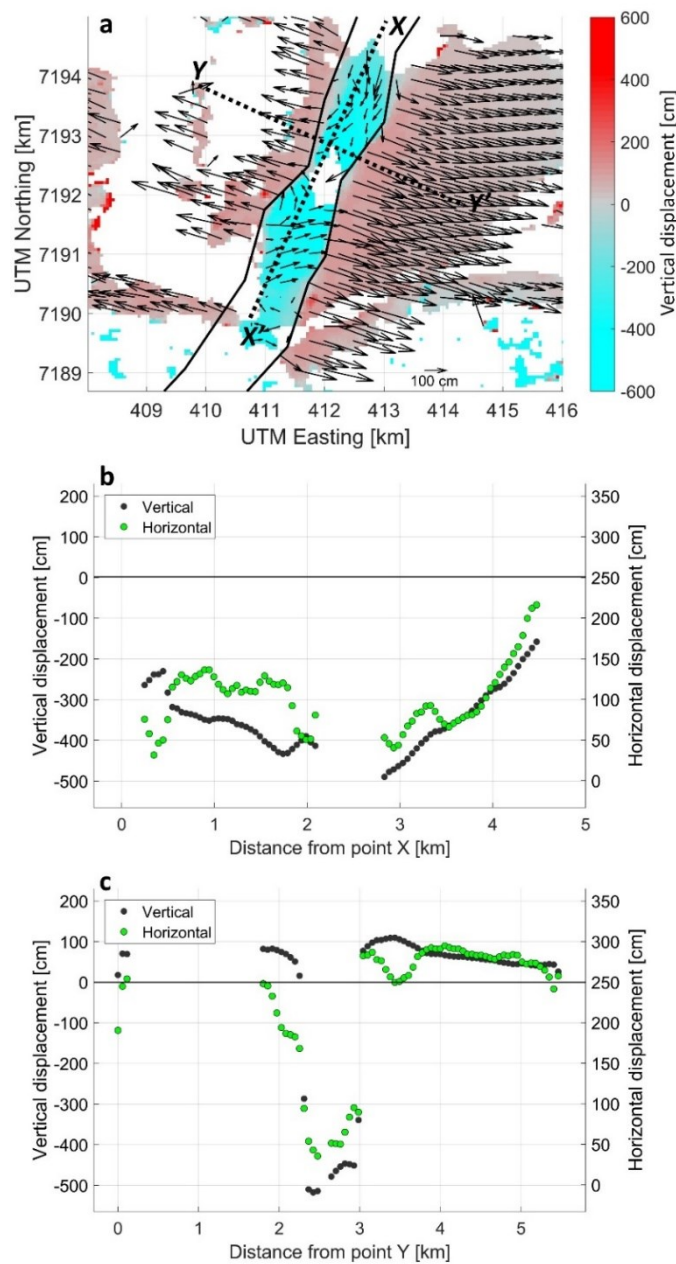


Figure 5-5. Enlarged 3D displacement inferred from CSK and TSX dataset and cross-section across and along the graben subsidence. (a) Enlarged 3D displacement inferred from TSX ascending and CSK descending data. The displayed region is shown in Figure 5-4c. Black solid lines trace discontinuities of vertical displacement. Dashed lines show locations of profiles along the graben (X-X'), and that across the graben (Y-Y'). Arrows show the direction and amount of horizontal displacement. Scale of horizontal displacement is shown at the right-bottom of the figure. (b) Profile of vertical (grey dots) and horizontal displacement (green dots) along X-X'. (c) Profile of vertical (grey dots) and horizontal displacement (green dots) along Y-Y'. Right axis shows the vertical displacement. Left vertical axis shows the horizontal displacement.

pixel trackings reveal wider displacement field over the ice-free region than the CSK ascending data. TSX range offset shows 5 m of positive signal at the subsiding graben. The amplitude of positive signal corresponds to the CSK co-diking range offset from ascending track in Figure 5-2b. TSX azimuth offset shows not only signal at the graben flank, implying NW-SE extending horizontal displacement, but also horizontal displacement toward the minor eruption site at the graben subsidence; 1 m of negative signal at the northern half of graben floor and 40 cm of positive signal at the southern half of graben floor. The negative signal at the northern half of graben floor was also identified in the CSK co-diking azimuth offset from ascending track. Figure 5-4c shows another co-diking 3D displacements which are inferred from TSX ascending and CSK descending data, and Figure 5-5a shows enlarged 3D displacements near the graben. The region is shown in Figure 4c as black box. The 3D displacements indicate 6 m of subsidence with 1 m of rift-parallel horizontal displacements toward the minor eruption site at the graben floor (Figures 5-4c and 5-5a). At the graben flanks, 3 m of WNW-ESE horizontal displacements, which are nearly perpendicular to the graben axis, with 1 m of symmetric uplift (Figures 5-4c and 5-5c).

RS2 data was acquired from two individual ascending tracks; track 81 (T81) and 181 (T181). We employed a larger window size for RS2 dataset to reduce decorrelation noise (Figure 5-6, Table 5-1). We processed one RS2 pair of 1 August 2014 – 18 September from T81 to infer co-diking offset. RS2 T181 dataset is used to check whether we can detect consistent displacement patterns with the RS2 T81 pixel tracking. Pre-diking range offsets indicate positive signal on the icecap, implying ice thinning, as we showed with CSK range offsets reveal in Figures 5-6a and 5-6d. The pre-diking RS2 azimuth offset are seriously contaminated by noise, and we could not identify any signals of icecap surface movement (Figures 5-6g and 5-6j). Co-diking RS2 range offsets reveal rectilinear positive signal along the dike at both non-ice region and the icecap, indicating graben subsidence. RS2 co-diking azimuth offsets show signal discontinuities along the dike at both ice-free region and icecap

(Figure 5-6h and 5-6k). The signal signs on both ice-free and icecap regions are consistent with each other, and signal amplitude on the icecap is stronger than that at ice-free region.

5.2.3 Estimation of subglacial ground deformation

We evaluate crustal deformation taking place beneath the icecap using pixel tracking data as presented in Chapter 5.2.2. Since our TSX data showed only co-diking signal, we used only CSK and RS2 data to infer the subglacial crustal deformation. Our strategy to estimate the subglacial ground deformation is to subtract the scaled pre-diking signal (cm/day) from the co-diking signal (cm). Here we assume that the pre-diking data contain only the icecap surface movement. The scaling factors in each case were determined so that the inferred crustal deformations became smooth at the edge of the icecap. Each of data acquisition intervals and the scale factors are shown in Table 5-1.

Figures 5-2c and 5-2f show the corrected icecap signal, call it “ice-corrected signal” as follow. The ice-corrected CSK range offsets from both ascending and descending track show insignificant offsets along the icecap edge, indicating that the icecap surface movement in CSK range offset could be well-corrected. Although the CSK coverages over the icecap are limited, the CSK range offsets isolate the subglacial crustal deformation due to the dike intrusion. Figure 5-7 shows the profiles of co-diking and ice-corrected range offset across the graben. The profiles of the co-diking signal at non-ice region (profile P-P’) and the ice-corrected signal (profiles Q-Q’ and R-R’) also suggest that the icecap signal in the co-diking signal well-corrected because all signal trends are similar. The icecap signal correction was also functioning as expected in the CSK ascending azimuth offset (Figure 5-2i), whereas the 1 m of negative residual was still leaving on the icecap in the CSK descending azimuth offset (NNE horizontal displacement) even though we tried to change the scale factors to reduce the icecap signal (Figure 5-2l).

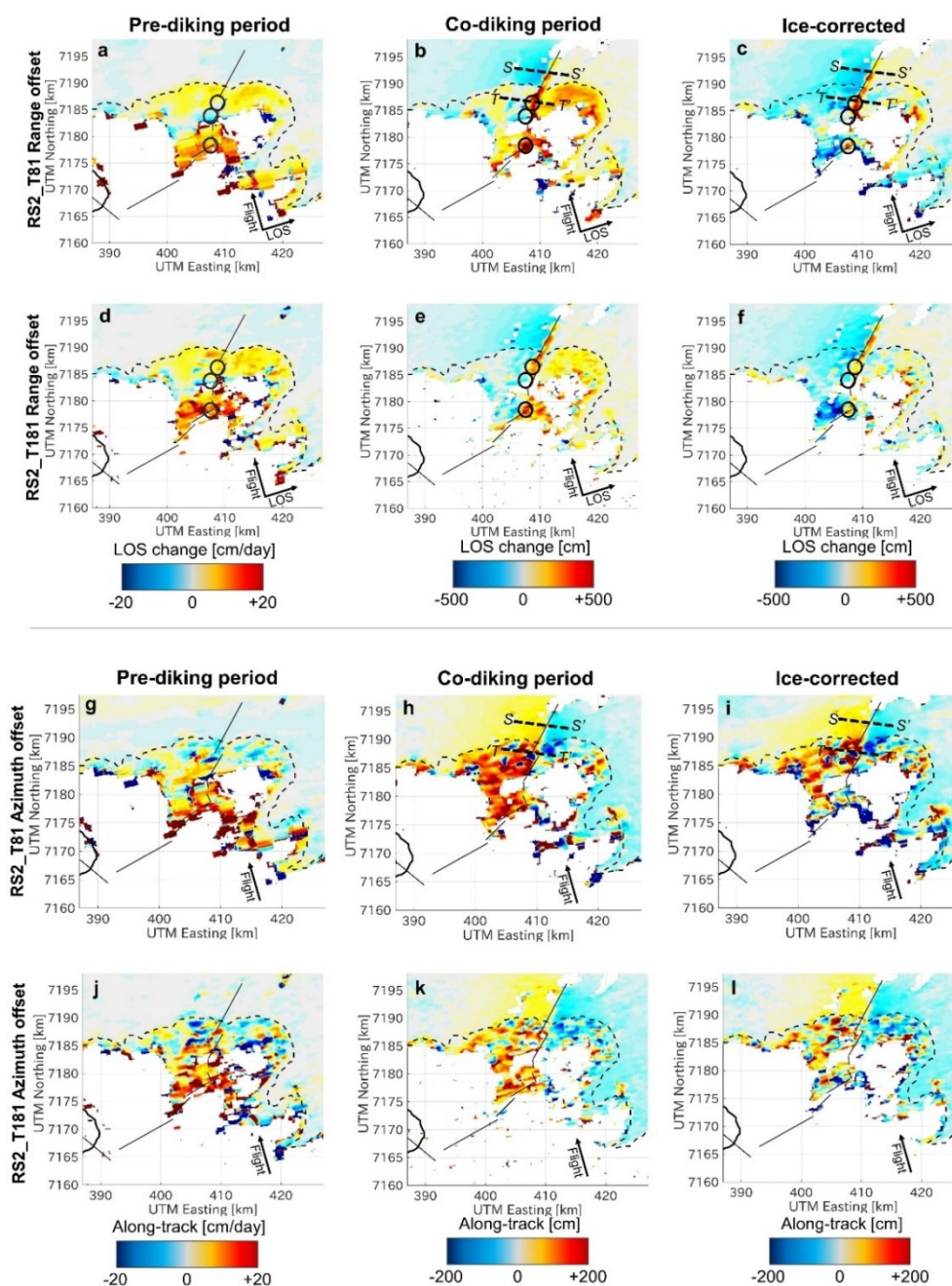


Figure 5-6. RADARSAT-2 (RS2) pixel tracking results during pre- and co-rifting period and ice-corrected signal. RS2 range offset (line-of-sight: LOS) from track 81 (a-c, pre-diking: 8 July 2014-1 August 2014, co-diking: 1 August 2014-18 September 2014, ice-corrected) and track 181 (d-f, pre-diking: 28 June 2014-8 August 2014, co-diking: 8 August 2014-1 September 2014, ice-corrected). RS2 azimuth offset (along-track) from track 81 (g-i) and track 181 (j-l). Dotted lines show the profiles of R-R', and S-S' in Figure 5-8. Dashed lines trace outline of the icecap. Solid black lines and circles are the locations of dike segments and ice cauldrons after Sigmundsson et al. (2015), respectively. Red triangle denotes the Holuhraun main eruption site during the episode. Black dots are selected points of time series of ice surface change in Figure 5-9. Black dots with capital letters (A-C) locate observation points for time-series of icecap surface changes (Figure 5-9). Coordinates are in UTM zone N28.

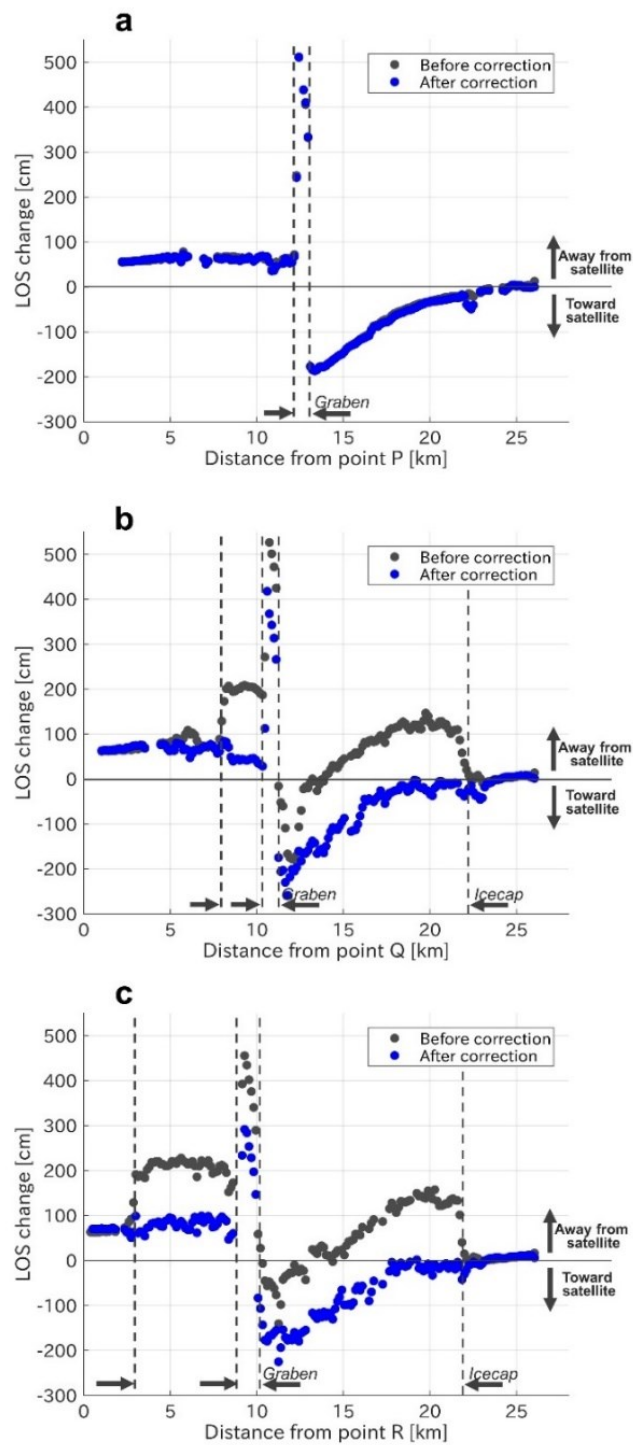


Figure 5-7. Cross sections of descending Cosmo-SkyMed (CSK) range offset during the co-diking signal (grey dots) and ice-corrected signal (blue dots). Profiles along P-P' (a), Q-Q' (b), and R-R' (c). Each location of cross section is shown in Figure 5-2. Unit vector of CSK descending range offset is $[\mathbf{e}_{\text{east}}, \mathbf{e}_{\text{west}}, \mathbf{e}_{\text{vertical}}] = (-0.443, 0.118, -0.889)$. Arrows indicate locations of icecap terminus along each cross section. Vertical dotted lines show the icecap edge and displacement discontinuities.

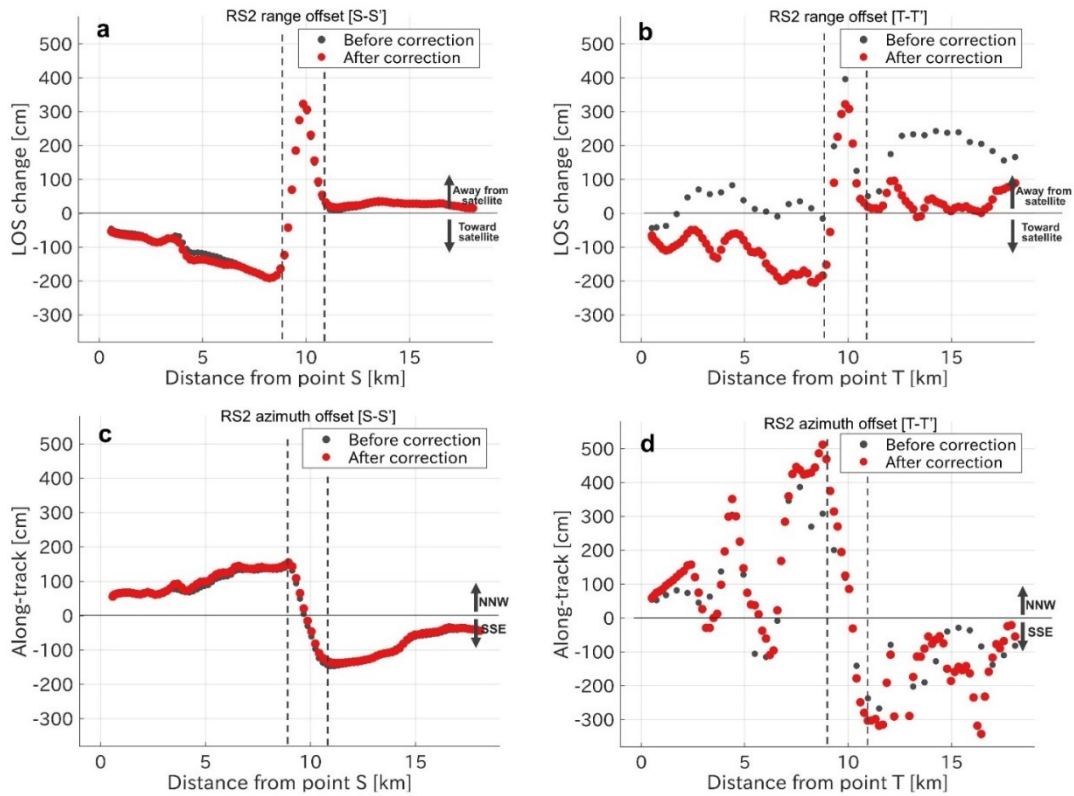


Figure 5-8. Profiles of RADARSAT-2 (RS2) range and azimuth offset in Track 81 during the co-diking signal (grey dots) and ice-corrected signal (red dots). (a) Profile S-S' and (b) profile T-T' of range offset. (c) Profile S-S' and (d) profile T-T' of azimuth offset. The locations of profile S-S' and T-T' are shown in Figure 5-6. Unit vector of RS2 range offset and azimuth offset is $[e_{\text{east}}, e_{\text{west}}, e_{\text{vertical}}] = (-0.443, 0.118, -0.889)$. Dotted lines show the location of displacement discontinuities.

Figures 5-6c and 6f show the RS2 ice-corrected signal, and the profiles along S-S' and T-T' show in Figure 5-8. Co-rifting RS2 range offsets also show the signal of both crustal deformation and icecap surface movement, the rectilinear positive signal in the corrected range offsets implies the graben subsidence beneath the icecap.

5.2.4 Temporal changes of icecap surface change

In order to study the temporal changes of icecap surface at the northernmost part of the icecap, we applied pixel tracking approach to both CSK and C-band Sentinel-1A data from 2014 July to end of 2016 (Figure 5-9, Appendix A). We set 256 by 256 pixels of window size for range and azimuth

direction, respectively. In this chapter, we used only range offset to evaluate the temporal variation of icecap surface movement. Because the incidence angles are slightly different between CSK and S1A dataset, we normalized LOS displacement by the cosine of the radar incidence angle as follow to correct the variation of observation geometry.

$$\Delta LOS = \frac{d_{LOS}}{\cos i}$$

ΔLOS is independent of vertical component of LOS displacement, d_{LOS} is the measured LOS displacement, and i is the radar off-nadir angle. The temporal variation shows the data within 500 by 500 m around the observation points A-C where the points are shown in Figure 2a-e. We discarded the cross correlations of below 0.05. No filtering functions in space and time domains were employed. Here we did not consider variations of microwave penetration depth through ice and snow depending on the radar wavelength and polarization (Rignot et al., 2001).

Figure 5-9 shows the temporal variation of vertical component of LOS of CSK and S1A data. The time-series of both ascending and descending tracks show positive peaks of vertical component of LOS change during summers, suggesting ice thinning due to ice melting. Maximum vertical component of LOS change is 5-8 cm/day at the observation points. The time of reaching maximum peak are slightly different from year to year between June and September, although maximum values of vertical component of LOS change are similar through 2014-2016. Only few centi-meters per day of positive or negative vertical component of LOS change were observed from autumn to spring, indicating relatively stable conditions.

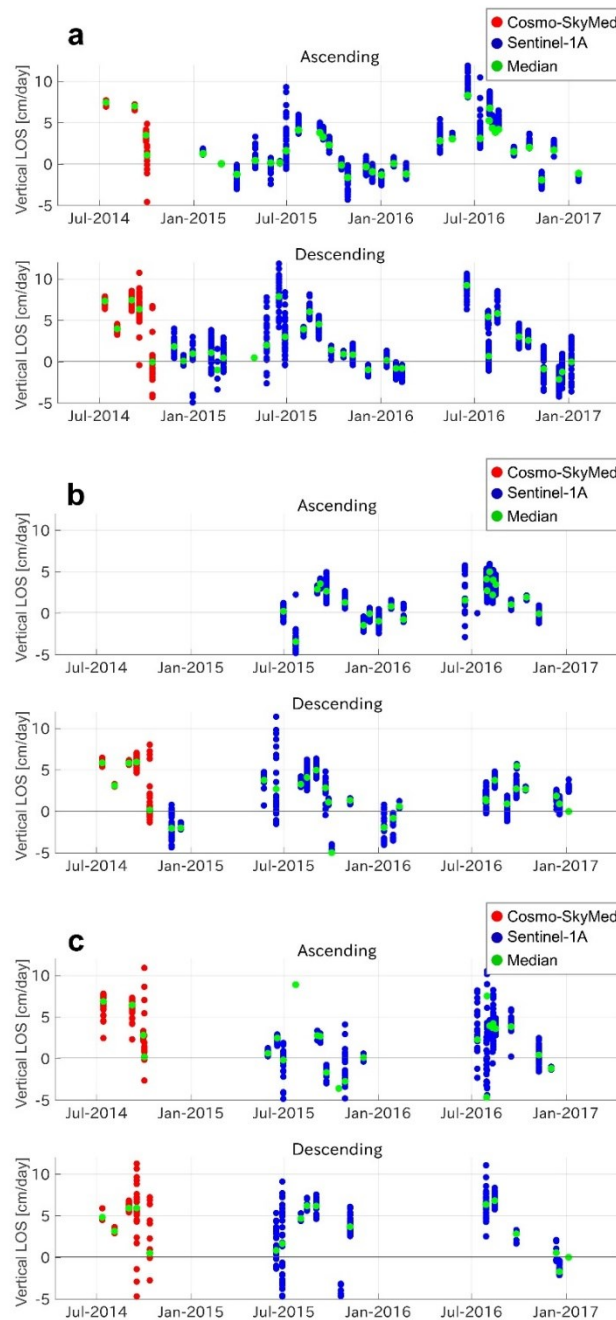


Figure 5-9. Time-series of vertical component of line-of-sight (LOS) change on the icecap from June 2014 to January 2017. The data are inferred from COSMO-SkyMed (CSK, Red dots) and Sentinel-1A (S1A, Blue dots) range offset within 500 by 500 m around points A (a), B (b), and C (c), where the locations of points A-C are shown in Figures 5-2 a-f. The vertical component of LOS change is decomposed by using cosine of off-nadir angle. Off-nadir angles for CSK and S1A data are 27.3 and 33.4 degrees, respectively.

5.3 Elastic modeling

5.3.1 Model setting and geometry

The ice-corrected signals provide us with the crustal deformation signals under the icecap due to the dike intrusion, extending the spatial coverage of observations. Crustal deformation is often interpreted by analytical solutions for rectangular dislocation (Okada, 1985, 1992) or triangular dislocation (Meade, 2007) in an elastic half-space and we follow that approach. Our model consists of a vertical dike and two graben bounding fault planes, in order to reproduce both near-graben and far-field displacement. Using the ice-corrected signals, we invert for the distributions of both dike opening and fault slip. We used analytical solutions for triangular dislocation elements in a homogeneous elastic half space from Meade (2007) to represent curved planar segments without gaps and/or overlaps. Each plane is constructed by triangular elements using Gmsh software (Geuzaine & Remacle, 2009). Patch size of the triangular elements varies from 800 m at shallowest part (0 m) to 2500 m at deepest part (8 km) because spatial resolution of opening/slip distributions at deeper part is worse than that at shallower part. The geometries of the fault segment are similar to the model in Ruch et al. (2015), but the dike segment is extended to further southward as we have more observational constraints on deformation under the icecap. Intersection of fault segment with the Earth surface can be inferred from the sharp displacement discontinuities in CSK and TSX pixel tracking data, indicating surface ruptures of the fault above the dike. Other parameters of each segment are determined by using trial-and-error approach so that we could minimize root mean square misfit and plausible opening/slip distributions (e.g., Furuya and Yasuda, 2011).

In our model, we allow only pure opening along the dike and normal faulting along the graben-bounding faults, because the co-diking 3D displacement reveals the rift-perpendicular horizontal displacement at the graben flanks. The opening/slip distributions were inferred from solving a weighted non-negative least square problems to minimize misfit residuals. A smoothing constraint

for the opening/slip distributions is imposed by using a Laplacian operator to reduce solution roughness and to obtain plausible opening/slip distributions (Simons et al., 2002; Wright et al., 2003).

In addition to the pixel tracking results, we also employed a RS2 InSAR and multiple aperture InSAR (MAI) data (Bechor & Zebker, 2006) (Table 5-2) in our inversion. Although both InSAR and MAI data are lacking data where displacement gradient is high, measurement accuracies of InSAR and MAI are better than that of pixel tracking data. Thus these data are expected to well constrain the far-field displacement. InSAR shows line-of-sight change inferred from phase difference between two coregistered satellite SAR data (Massonnet & Feigl, 1998). Multiple aperture interferograms (MAI) reveal along-track displacement inferred from forward- and backward-looking interferograms (Bechor & Zebker, 2006). Forward- and backward-looking interferograms are derived from two sub-band single look complex images by the azimuth split-beam method. Measurement accuracy of MAI is slightly worse than that of InSAR because of losing a part of band width for azimuth direction. Each standard deviation is shown in Table 5-2.

We applied InSAR and MAI method to RS2 data by using GAMMA software as well as the pixel tracking approach (Table 5-2). We employed an adaptive filter with a window size of 32 pixels to avoid phase unwrapping error (Goldstein & Werner, 1998). The InSAR and MAI were unwrapped phase by using branch cut algorithm (Goldstein et al., 1988). Topography-dependence signal in the InSAR was corrected by using the mosaiced 1-arc second digital elevation model (DEM) of TanDEM-X and EMISAR (Magnússon et al., 2005). We did not remove any long wavelength phase trend across the data.

The data are weighted by the inverse of diagonal covariance matrices from root mean square (RMS) at the non-deformed area (Table 5-2). The inverted data were subsampled by averaging

neighbor values in space (“multi-looking”) to reduce noise and to reduce number of data. Numbers of data are shown in Table 2. The CSK descending azimuth offsets (Figure 5-2j) and TSX pixel tracking (Figures 5-4a and 5-4b) at the icecap were masked, because strong residuals of icecap signal were left.

5.3.2 Distribution of dike opening and fault slip

Figure 5-9a shows the inferred distributions of opening along the dike and normal faulting along the two graben bounding faults. A peak in opening is located near the southern end of graben bounding faults at the shallowest depth of the dike segment, where the northernmost ice-cauldron formed. The maximum dike opening in our model is 6.1 m. The volume of dike opening inferred from our model is 0.4 km³, which is about 27 % of the predicted volume of magma ejection (Gudmundsson et al., 2016; Pedersen et al., 2017). The distribution of opening in our model is nearly consistent with the model in Sigmundsson et al. (2016), whereas the previous model presented bimodal peaks of pure opening. Our model has little opening at the southern end of the dike because our data does not constrain the opening distribution there. As previous models have demonstrated, the opening distribution concentrates at depths shallower than 5 km, which is clearly above the seismicity along the dike (Ágústsdóttir et al., 2016). The limited seismicity at the shallower depths of 5 km implies little brittle failure due to the low crust rigidity, where pure opening is distributed in our models. The 6 m of normal faulting along the graben-bounding faults can explain almost all of the 6 m of graben subsidence in the 3D displacements (Figures 5-3b and 5-4c). The standard deviations of opening/slip distributions are inferred from the 200-times iterative inversions with synthetic 2D correlated noises (Wright et al., 2003) (Figure 5-10b). The opening uncertainty at a shallow part of the dike segment with the graben-bounding faults is about 60 cm, while the maximum standard deviation of dike opening is 3.1 m at the southernmost of the dike. The estimated standard deviations of normal faulting are below 50 cm, which is significantly less than the inferred normal faulting distributions. The large opening error at the southernmost part of the dike originates from the fact that the displacement data

limited, although the far-field displacement estimated from InSAR and MAI data was expected to constrain the southernmost dike opening.

We evaluated if the ice-corrected signal at the icecap contributed to improve the elastic model. The opening/slip distributions in Figure 5-12 are inferred from the data that are masked above the icecap (“ice-masked model”). The model geometry and other parameters are the same as our best-fit model. Although about 1 m of dike opening was inferred at the southern part of dike, larger standard deviation was identified, indicating less reliability of dike opening. Also, the ice-masked model shows a large artificial implausible slip distribution and large standard deviations at the southern edge of faults. While the distribution patterns of opening/slip are slightly different at the ice-free region, standard deviation of ice-masked model is almost equal to that of our best-fit model at the ice-free region. We therefore conclude that the ice-corrected signal contributes to improve the modeled slip distributions.

Figure 5-11 compares subsampled observations with the calculations based on the inferred opening/slip distributions, and residuals for each data. Root mean square errors (RMSE) are reported at the right bottom of each residual panel. Overall, the synthetic range offsets could well reproduce the signal pattern of each observation. Our model can also reproduce two sharp offset discontinuities along the graben in the range offsets. Even though the weight of CSK descending range offset is larger than that of any other offsets, the misfits are still left in this data set, especially positive residuals at the western part of graben flank. The misfit may derive from a scaled decorrelation noise during the correcting the icecap signal (Figures 5-2d-f). Although the weights of azimuth offset for the inversion are relatively low, the RMSE of azimuth offset is similar level with that of range offset. Our model cannot retrieve well the rift-parallel displacement at the graben subsidence in the azimuth offsets. Regarding the southern half of RS2 data coverage, it is hard to assess whether our model could

reproduce the observations well or not because the observation offsets on the icecap are contaminated by decorrelation noise even if the data were subsampled coarsely. The broad signal patterns of both range and azimuth offset can be reproduced, although the predicted RS2 azimuth offset was significantly underestimated.

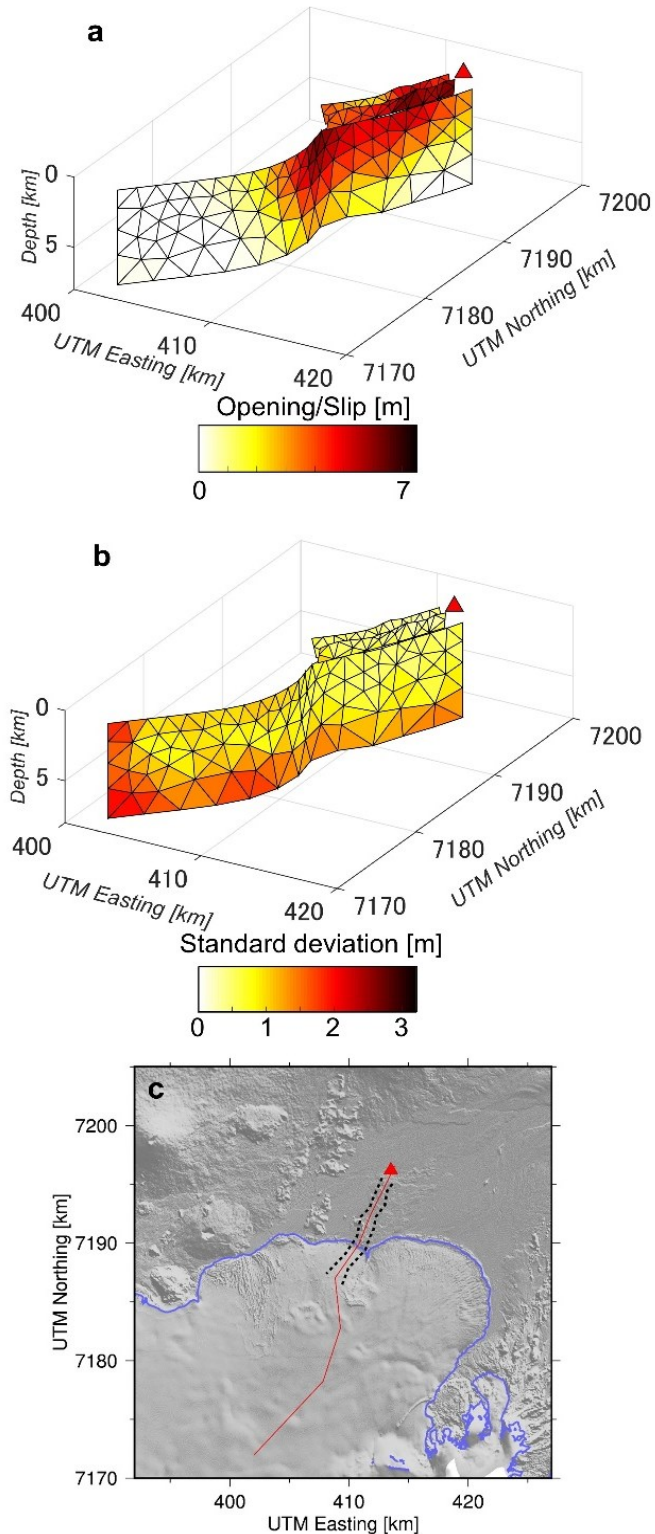
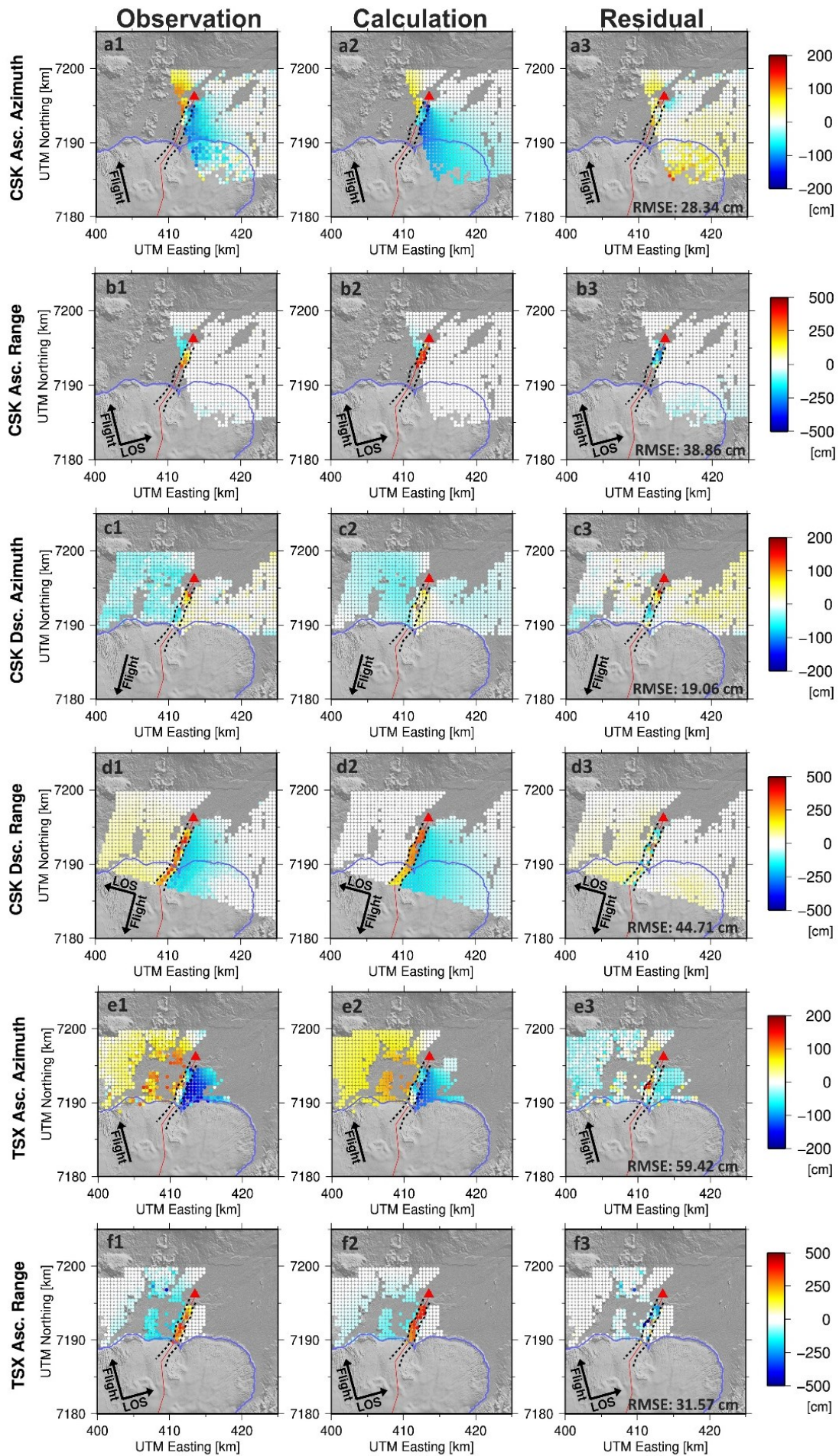


Figure 5-10. Our optimal elastic model and the model geometry. (a) Inferred dike opening and normal faulting along the graben-bounding faults. (b) Standard deviations are derived from 200-times iterative inversions with synthetic 2D random noise. The distributions are projected from NE. (c) Map showing the top location of dike and graben bounding faults, and outline of the icecap. Red triangles show the location of the Holuhraun main eruption site. Light blue line traces the outline of the Vatnajökull icecap. Black dashed lines show the top location of graben bounding faults. Coordinates are in UTM zone N28.



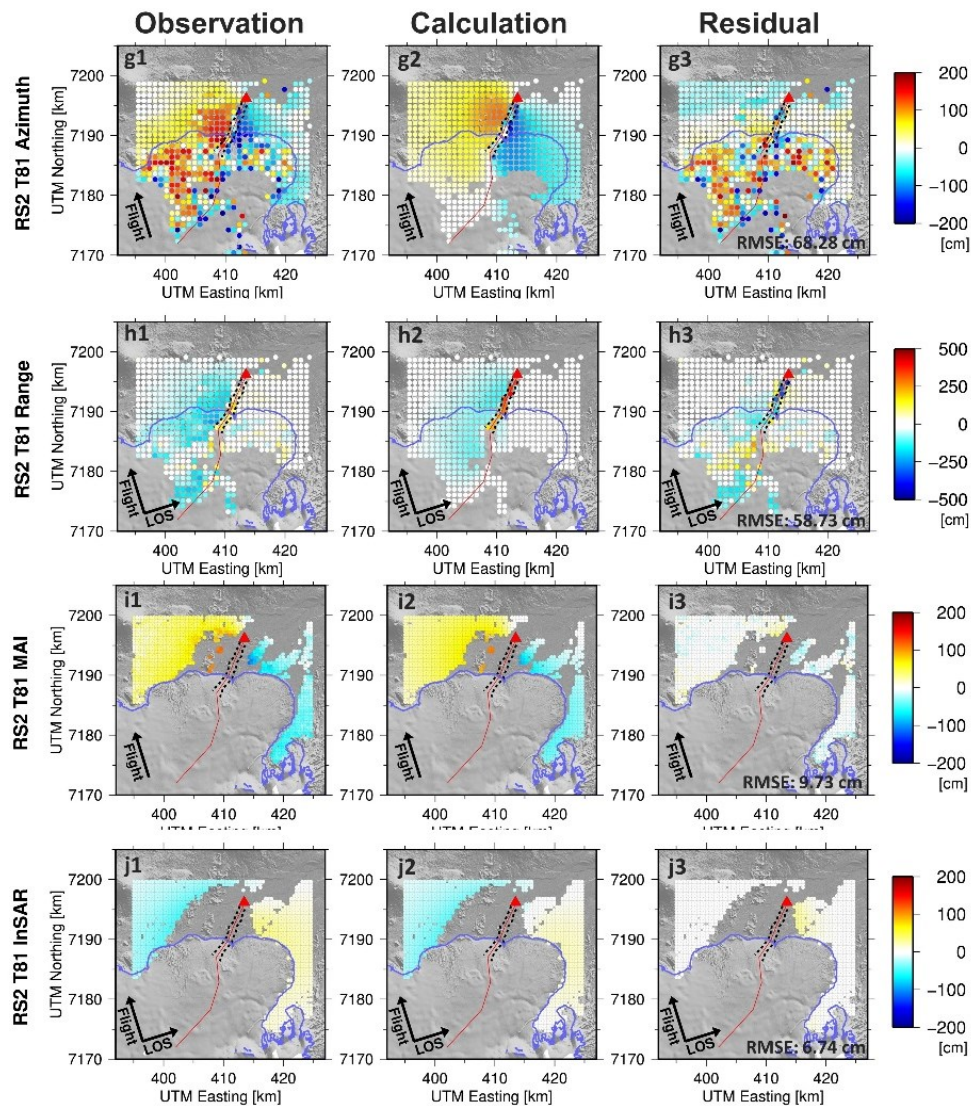


Figure 5-11. Comparison of observations, calculations derived from our model, and residuals. (a-j1) Subsampled observations, (a-j2) calculations inferred by the slip/opening distribution, and residuals (a-j3). (a1-3) Cosmo-SkyMed (CSK) ascending azimuth offset, (b1-3) CSK ascending range offset, (c1-3) CSK descending azimuth offset, (d1-3) CSK descending range offset, (e1-3) TerraSAR-X (TSX) ascending azimuth offset, (f1-3) TSX ascending range offset, (g1-3) track 81 (T81) RADARSAT-2 (RS2) azimuth offset, (h1-3) T81 RS2 range offset, (i1-3) T81 RS2 multiple aperture interferogram (MAI), (j1-3) T81 RS2 interferogram (InSAR). Positive signal of azimuth and range offset show horizontal displacement toward satellite flight direction and line-of-sight change away from satellite, respectively. Dashed black and solid red lines project top edges of graben-bounding faults and the dike segment in our model. Red triangles locate the Holuhraun main eruption. Arrows indicate the directions of satellite flight (“Flight”) and line-of-sight (“LOS”), respectively. Blue solid lines traced the outline of icecap.

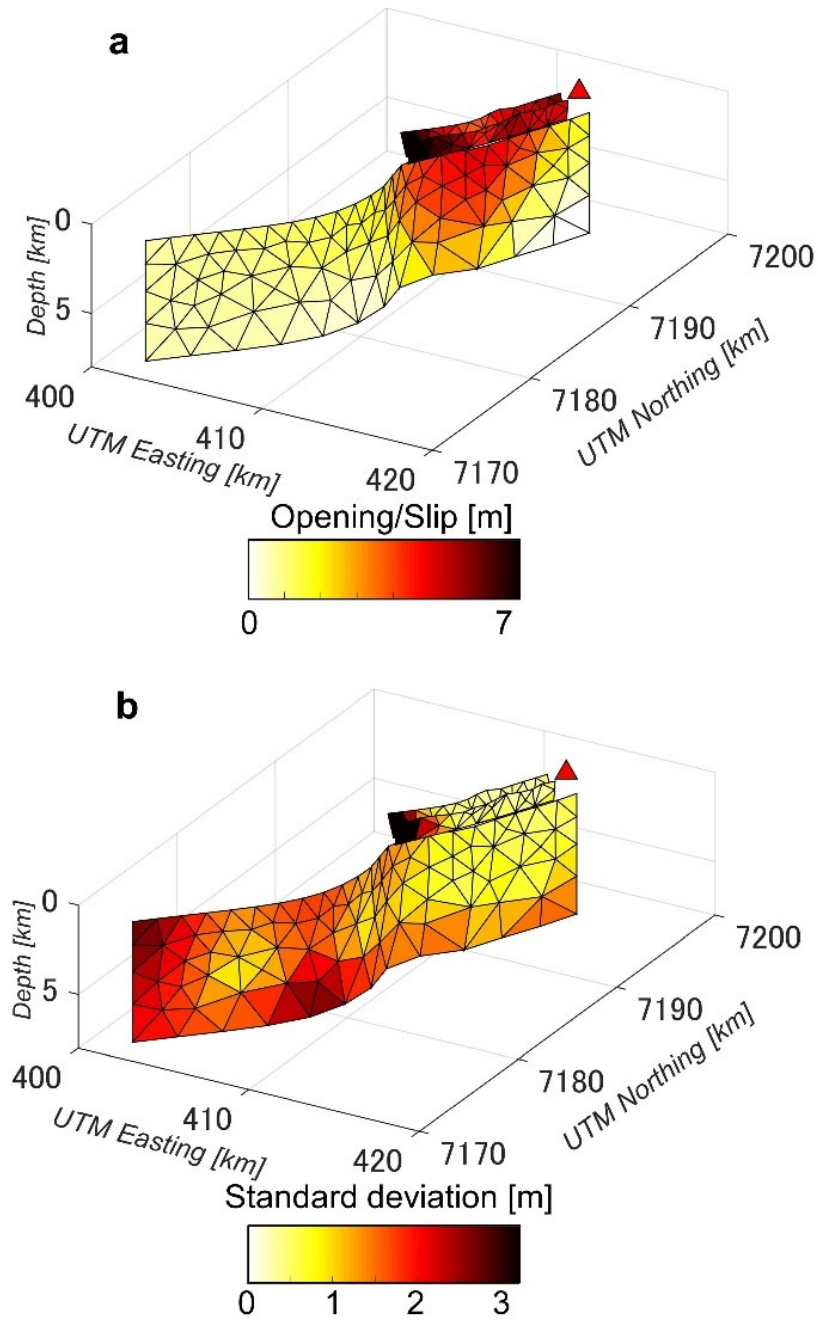


Figure 5-12. Dike opening and normal faulting distributions inferred from the observations which are masked above the icecap and its standard deviations. (a) Inferred dike opening and normal faulting along the graben-bounding faults. (b) Standard deviations are derived from 200-times iterative inversions with synthetic 2D random noise. The distributions are projected from NE. Details are same as Figure 5-10. Color scales are also same in Figure 5-10.

Table 5-2. Dataset for inferring elastic model

Satellite ^a	Orbit ^b	Data ^c	RMS [cm] ^d	Weight [%] ^e	Number of data ^f
Cosmo-SkyMed	Ascending	Range offset	9.3	7.6	3139
		Azimuth offset	10.8	6.6	3208
	Descending	Range offset	3.8	18.5	5137
		Azimuth offset	18.7	3.8	3577
TerraSAR-X	Ascending	Range offset	19.0	3.7	2002
		Azimuth offset	16.1	4.4	2413
RADARSAT-2	Ascending	Range offset	12.76	5.6	727
		Azimuth offset	16.1	4.4	772
		MAI	9.9	7.2	4102
		InSAR	1.9	38.2	2683

a Name of SAR satellite

b Satellite flight direction. Ascending means flight from SSE to NNW. Descending means flight from NNE to SSW.

c Input data for modeling.

d Root-mean-square at non-deformation area. RMS can be regard as measurement accuracy of the dataset.

e Relative weight for the inversion in Chapter 5.3. The weight is based on RMS.

f Number of input data for inversion in Chapter 5.3.

5.4 Discussion

We confirmed that the pixel tracking approach is suitable for isolating subglacial crustal deformation using the scaled pre-diking and co-diking signals. Although we detected the deformation signals above the icecap along northern half of the dike using the RS2 data, the RS2 pixel tracking data showed data lacking above the icecap around the Bárðarbunga caldera. Even though we processed RS2 dataset with shorter temporal baseline, we could not detect the signal there. First possibility is that there are few surface characteristics above the icecap. The pixel tracking approach finds the most similar characteristic within an arbitral window size using a cross-correlation function. The northern edge of the icecap surface where we revealed surface movement using the pixel tracking approach looks surface characteristics there due to steady-state of ice flow, however the icecap surface around the caldera looks smooth expect for the caldera outline. Because the approach cannot distinguish a region where we would like to find with an others region with smooth, we cannot reveal the surface Second possibility is that warm climate during the episode can change ice surface condition. Variation of the back-scatter intensity between two SAR images also induces the decorrelation problem. Even though the topographic height of the summit is about 2000 m and Iceland is one of the Arctic regions, we presume that the climate in summer makes it easier to melt and freeze which induces to vary ice surface condition. Third possibility is the carrier frequencies of radar microwave. The longer the wavelength of radar microwave is, the deeper penetration depths of microwave through ice is (Rignot et al., 2001). In general, the condition near ice surface is more sensitive to precipitation and temperature change comparing with that at the deeper part of ice. The scatter characteristics above ice can be more stable if we employ SAR data acquired by using longer-wavelength radar microwave such as L-band SAR data. We processed a pair of PALSAR-2 data to detect the icecap surface change during the event (Figure 5-13). Even though the data acquisition interval of the PALSAR-2 data we processed is 14 days, the PALSAR-2 interferogram revealed the signals of steady-state of icecap flow. We, however,

could not infer the icecap surface change due to the subglacial dike intrusion using PALSAR-2 dataset because the image did not cover the ice region above the dike. We also show the others CSK pixel tracking data with short intervals of image acquisition covering the Bárðarbunga caldera (Figures 5-14 and 5-15). The CSK pixel tracking data acquired from August to September indicate missing signals above both the Vatnajökull icecap and the ice at Tungnafellsjökull volcano even though the data acquisition interval was 1 day (Figures 5-14 and 5-15), while we revealed signals of the caldera subsidence in the CSK pixel tracking data during October. Thus we propose from these figures that second factor is supposed to be the strongest contributor for missing data in our pixel tracking data, although the others factors can also influence to contaminate our observation data.

In this chapter, the subglacial crustal deformation was inferred by subtracting the scaled pre-diking signal from the co-diking signal (Figures 5-2 and 5-6). Although the icecap signal was corrected well in the range offset, we cannot ignore significant residuals in the RS2 and CSK azimuth offsets. One possibility of the residuals is the difference of physical properties between crust and ice. Generally, crustal deformation can be described as elastic response. Instantaneous ice deformation can also be approximated as elastic deformation, because ice deformation can be described by a non-linear Burger's body viscoelastic model (Tsai et al., 2008). Assuming the co-diking displacement occurs within a short time, we can regard the icecap deformation due to the subglacial crustal deformation as elastic deformation. In order to evaluate the icecap movement due to the subglacial crustal deformation accurately, we may, however, need to consider about the difference of physical properties.

Simulated ice mass balance of the Vatnajökull icecap near Holuhraun during 1991-2006 shows that average mass loss during summer corresponds to 4-6 m of ice thinning (Björnsson & Pálsson, 2008). Our time-series results are broadly consistent with the numerical simulation if we

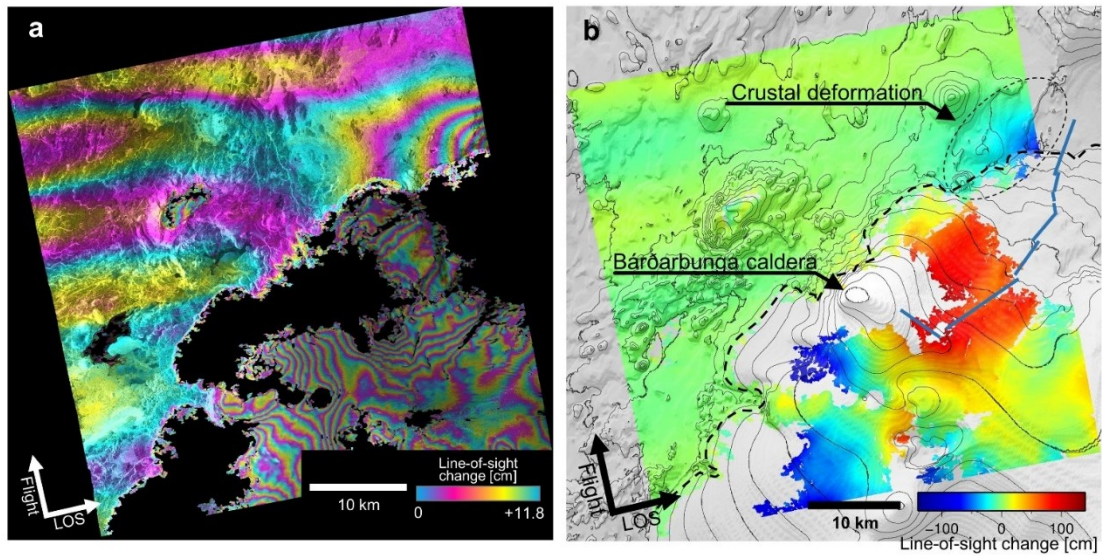


Figure 5-13. A PALSAR-2 interferogram across the Bárðarbunga caldera. a) Wrapped interferogram. Color cycle represents 11.8 cm of displacement along the line-of-sight direction. b) Unwrapped interferogram. Positive signal indicates line-of-sight displacement away from the satellite. Blue lines indicate the dike path inferred from migrated seismicity (Sigmundsson et al., 2015).

assume 5-7 cm/yr of vertical change for 90 days in summer time even if ice mass loss have been accelerating after the study by Björnsson & Pálsson (2008) was published. We note that maximum vertical component of LOS change rate in the summer of 2014 is similar to that in 2015 and 2016. Also, vertical component of LOS change rate during winter of 2014-2015, when the fissure eruption had been still ongoing, decreases to near zero, same as that in winter of 2015-2016 and 2016-2017. These findings suggest no significant regional basal melting anomaly due to the event.

Our optimal model involves both advantages and disadvantages comparing with previous models. Previous models allowed not only opening but also sinistral shearing along the dike based on their geodetic observations and the left-lateral strike-slip earthquakes (e.g., Sigmundsson et al., 2015; Ruch et al., 2016). The amount of shearing is less than 1 m to fit their observations. Our elastic model, however, allowed only pure opening along the dike because the retrieved 3D displacements show rift-

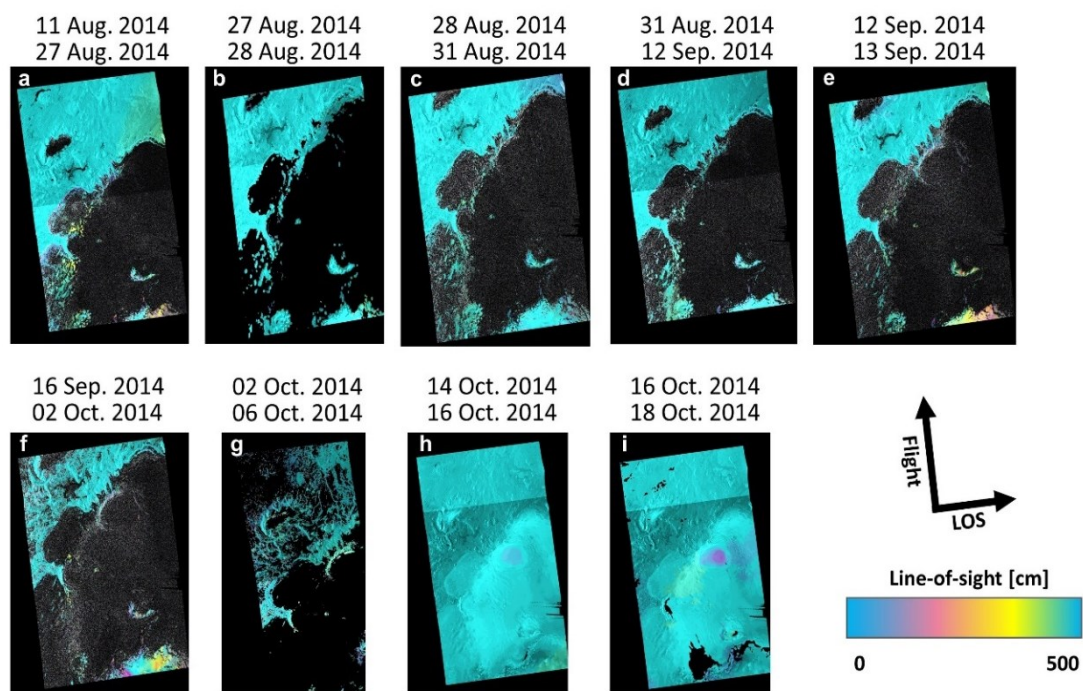


Figure 5-14. CSK pixel tracking data observed from ascending track across the Bárðarbunga caldera. Black color shows data lacking induced by decorrelation problems. Image acquisition date are presented above each figure and Appendix A. Black arrows show the satellite flight direction (Flight) and the beam illuminate direction (LOS), respectively.

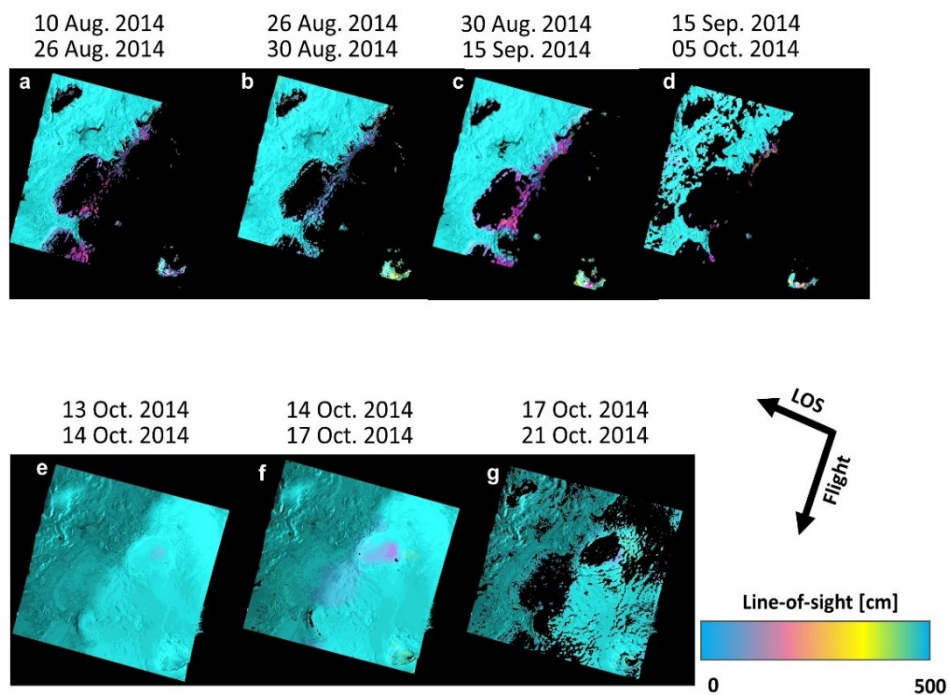


Figure 5-15. CSK pixel tracking data observed from descending track across the Bárðarbunga caldera. Details are same as Figure 5-14.

perpendicular horizontal displacements at the graben flanks with few left-lateral displacements (Figures 5-3b and 5-4c). We confirmed that our model could retrieve the pixel tracking observations well even at the inferred subglacial crustal deformation (Figures 5-11). Although we did not employ GNSS data for our inversion, the optimal model in this chapter has been constrained by the far-field displacement derived from RS2 InSAR and MAI data instead of GNSS observation (Figures 5-11i and 5-11j). The requirement of shearing for fitting the geodetic observations would need to be debated in detail. Another issue in our model is that our model did not consider the tectonic stress (Spaans & Hooper, 2018). Although previous GNSS measurements have revealed 18-19 mm/yr of extensional displacement toward WNW-ESE (DeMets et al., 2010), we ignored the tectonic stress because we focus on only the short-term displacement in this chapter.

5.5 Post-emplacment deformation of Holuhraun lava field

The Bárðarbunga dike intrusion episode accompanied fissure eruptions from September 2014 to February 2015 and 83 km² of the lava field formation at Holuhraun plain which is located to the north of Vatnajökull icecap (Gudmundsson et al., 2016; Pedersen et al., 2017; Sigmundsson et al., 2015). After ejected magma emplaced, the lava deforms, usually thinning, due to thermal contractions of lava, degassing and solidification (Caricchi et al., 2014). Post-emplacment deformations of lava fields observed by InSAR have been reported, such as at Hekla volcano, Iceland (Wittmann et al., 2017), Miyakejima volcano, Japan (Furuya, 2004). Regarding the Holuhraun lava field, a TanDEM-X DEM difference observation between September 2014 and February 2015 showed 42-45 m of the lava field height change due to the fissure eruption (Dirscherl & Rossi, 2018; Rossi et al., 2016). On the other hand, the post-emplacment deformation in the lava field has not been reported, to our knowledge. We provide preliminary results of the post-emplacment lava field deformation using L-band PALSAR-2 dataset as follows.

We applied the pixel tracking and the conventional stacking approaches to PALSAR-2 dataset for depicting the post-emplacement lava field deformations (Table 5-3). Analysis of PALSAR-2 data was computed by the GAMMA software. Topographic fringes were corrected by using 1arc-second ASTER GDEM, and long-wavelength fringes across the interferograms could be negligible. We adopted the minimum cost flow algorithm for the phase unwrapping (Costantini, 1998). We inferred the cumulative LOS changes by stacking interferograms of shortest temporal baseline in each track. Because the ascending PALSAR-2 InSAR spanning 2 February 2015 and 6 July 2015 was contaminated by phase unwrapping errors due to decorrelation problems, we employed the pixel tracking to depict LOS changes. The cumulative LOS change derived from the ascending PALSAR-2 dataset thus involves the pixel tracking and InSAR data. To correct observation geometries between the ascending and descending LOS changes, we normalized as vertical components of LOS change by dividing LOS change by cosine of each incidence angle. The equation for the correction is described in Chapter 5.2.4. We evaluate the temporal variation of lava field deformation at the maximum deformation site, and plotted signals within 500 m of the site. The variation from each median value can be considered as uncertainties of the observation.

Figure 5-16 shows the cumulative LOS changes derived from PALSAR-2 pixel tracking and InSAR and the temporal variation of vertical component of LOS change at the maximum displacement point which located slightly far from the eruption site. As we mentioned above, the ascending data involves both the pixel tracking and InSAR data, the descending data presented only InSAR data. Some InSAR showed decorrelation noises at outside regions of the lava field due to low signal-to-noise ratio (SNR). The low SNR could be caused by smooth surface characteristics where are few vegetations, covering/melting snow and covering volcanic ash. While the SNR above the lava

field was relatively high because the rough surface characteristics of the lava. The signal above the lava field therefore could be detected constantly. The deformation signals spread out from the eruption site toward northeastward direction as the topographic gradient is also sloping toward NE. The signal distributions are nearly consistent the lava flow through a channelized lava feeding system during the lava field formation (Pedersen et al., 2017). The maximum cumulative vertical component LOS changes in the ascending track depicted greater than 5 m of downward movements since February 2015. The temporal variation of decreasing deformation rate in the ascending data can be fitting by exponential and/or logarithmic functions rather than linear functions. For the descending data, the cumulative deformation amplitude is smaller than that of the ascending data. The reason is that the descending InSAR spanning 25 February 2015 to 8 April 2015 could also not show LOS changes correctly because of phase unwrapping errors. Although we applied the pixel tracking approach to the descending image pair, the procedure could not detect surface deformation signals because the descending PALSAR-2 data were acquired by using ScanSAR mode. Although applying the pixel tracking to the ScanSAR data is challenging for detecting signals due to worse spatial resolutions of SAR images, some papers have reported a glacier flow map of Greenland by applying the pixel tracking to Sentinel-1 interferometric wide (IW) swath mode, which depicts moderate spatial resolutions with wide coverages (e.g., Nagler et al., 2015). The PALSAR-2 ScanSAR could have detected the deformation signal if the research target area is wider and if the deformation is greater. Another pixel tracking spanning 24 November 2014 to 2 February 2015, indicating the co-eruptive period, depicted different signal trend, that is, greater 6m of negative signal with extending toward NE (Figure 5-17). Although negative signals from the ascending observation geometry propose eastward movements and/or uplifts, we expect that the negative signals in the pixel tracking indicate a combination of both eastward movements and uplift because of horizontal spreading and

accumulations of lava through channelized feeding systems. Lacking data region was inferred the newly lava covering area during the image acquisition interval.

Table 5-3. PALSAR-2 dataset for detecting the post-emplacment deformation.

Track	Orbit	Acquisition mode	Spatial resolution (Range, Azimuth [m])	Date [dd.mm.yyyy]	B_perp [m]
2	Ascending	Stripmap mode	4.3, 3.2	24.11.2014	0
				02.02.2015	225.40
				06.07.2015	224.63
				14.09.2015	65.63
				23.11.2015	193.58
				01.02.2016	173.76
				04.07.2016	106.53
				21.11.2016	129.67
				03.07.2017	167.39
11.09.2017	184.94				
113	Descending	ScanSAR mode (Swath No. 3)	19.0, 25.9	08.04.2015	0
				29.07.2015	-350.11
				02.12.2015	-190.00
				24.02.2016	-41.86

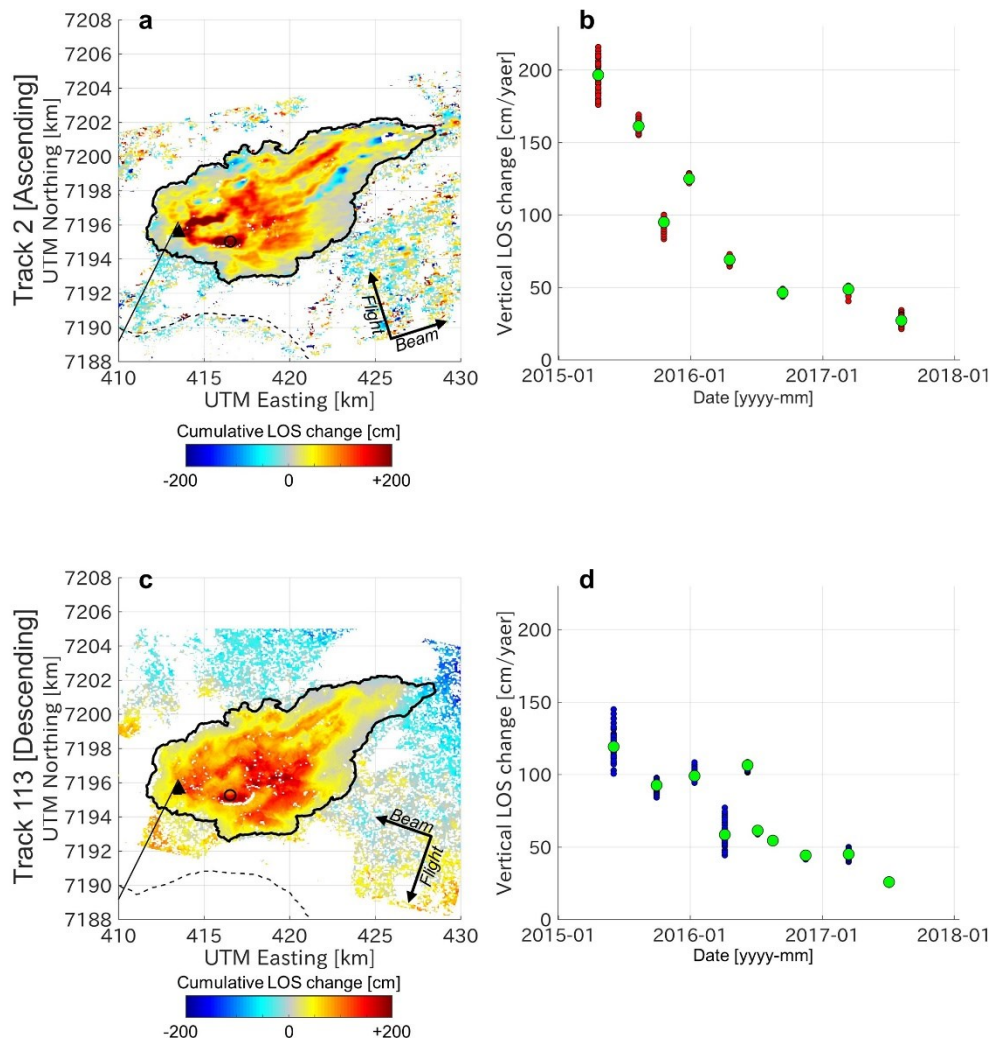


Figure 5-16. Lava field subsidence derived from stacked PALSAR-2 InSAR. (a, c) Cumulative vertical components of LOS change observed from the ascending (track 2) spanning 2 February 2015 to 11 September 2017 and the descending (track 113) PALSAR-2 data spanning 8 April 2015 to 23 August 2017, respectively. The vertical component LOS is normalized by divided LOS changes by their radar incidence angles for correcting observation geometries. Dashed line indicates the icecap outlines. Thin and thick solid lines are the dike path and the lava field outline, respectively. Black triangle located the fissure eruption site during the episode. Open circle indicates the point where the time-series of LOS change shows. Note that positive signals show LOS lengthening, approximating downward movement. b, d) Time-series of LOS changes of ascending and descending PALSAR-2 data, respectively. Green dots are median values of each dataset. Red and blue bots indicate the vertical component of LOS changes within 500 m of the observation point in the ascending and descending PALSAR-2 dataset, respectively.

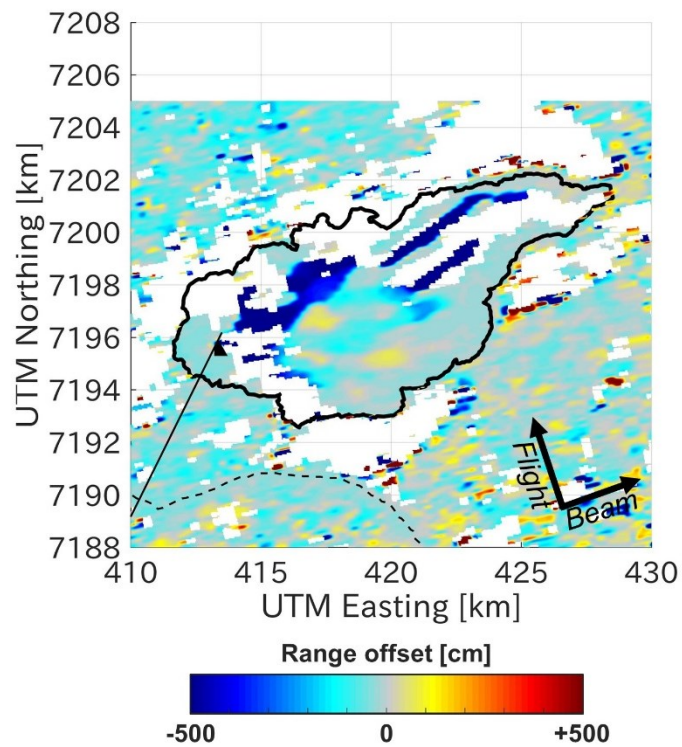


Figure 5-17. Range offset between 24 November 2014 and 2 February 2015. Negative signals indicate LOS shortening. Thick and thin lines trace the outline of the lava field and the dike, respectively. Dashed line presents the outline of the icecap.

Chapter 6

Dynamic Slip Partitioning Associated with the 2016 Kumamoto Earthquake Sequence, SW Japan

Main content in this chapter have been published in *Earth, Planets and Space*

Himematsu, Y., M. Furuya (2016) Fault source model for the 2016 Kumamoto earthquake sequence based on ALOS-2/PALSAR-2 pixel-offset data: evidence for dynamic slip partitioning, *Earth, Planets and Space*, 68:169, DOI 10.1186/s40623-016-0545-7

Chapter 6. Dynamic slip partitioning associated with the 2016 Kumamoto earthquake sequence, SW Japan

6.1 Introduction

Two $M_w > 6$ earthquakes hit Kumamoto prefecture on April 14, 2016 (M_w 6.2 [M_{JMA} 6.5] 12:26:41.1 UTC; M_w 6.0 [M_{JMA} 6.4], 15:03:50.6 UTC), followed by another shock (M_w 7.0 [M_{JMA} 7.3]) on the next day, 15 April (16:25:15.7 UTC) (Figure 6-1); the M_w is inferred by Japan Meteorological Agency (JMA) catalog (http://www.jma.go.jp/jma/en/2016_Kumamoto_Earthquake/2016_Kumamoto_Earthquake.html). After the main shock, the epicenters of aftershocks migrated from Kumamoto in NE and SW direction (Figure 6-1). According to the JMA focal mechanisms, right-lateral slip is the dominant component, whereas some focal mechanisms of the aftershocks indicate normal faulting. Moreover, not only the main shock but also the foreshocks and the aftershocks included significant non-double couple components (Figure 6-1), suggesting complex mechanisms of the Kumamoto earthquake sequence. Previous geological and geodetic observations pointed out the presence of Beppu-Shimabara rift system across the Kyushu island (Ehara, 1992; Matsumoto, 1979; Tada, 1993), along which the NE–SW trending seismicity of the 2016 Kumamoto earthquake sequence was distributed. The northeastern edge of the rift system is located at the most western part of the Median Tectonic Line that is the longest fault system in Japan (Ikeda et al., 2009). Meanwhile, the northernmost end of Okinawa trough reaches the southwestern edge of the rift system (Tada, 1984, 1985). The rift system contains geothermal area and active volcanic system including Kujyu, Aso and Unzen volcanoes. Based on geodetic observations by the first-order triangulation survey (Tada, 1984, 1985) and GPS network (Fukuda et al., 2000; Nishimura & Hashimoto, 2006), the central Kyushu region is inferred to be under N–S extension stress regime. Matsumoto et al. (2015) analyzed the focal mechanisms of shallow earthquakes in Kyushu from 1923 to 2013 and showed that Kyushu island was

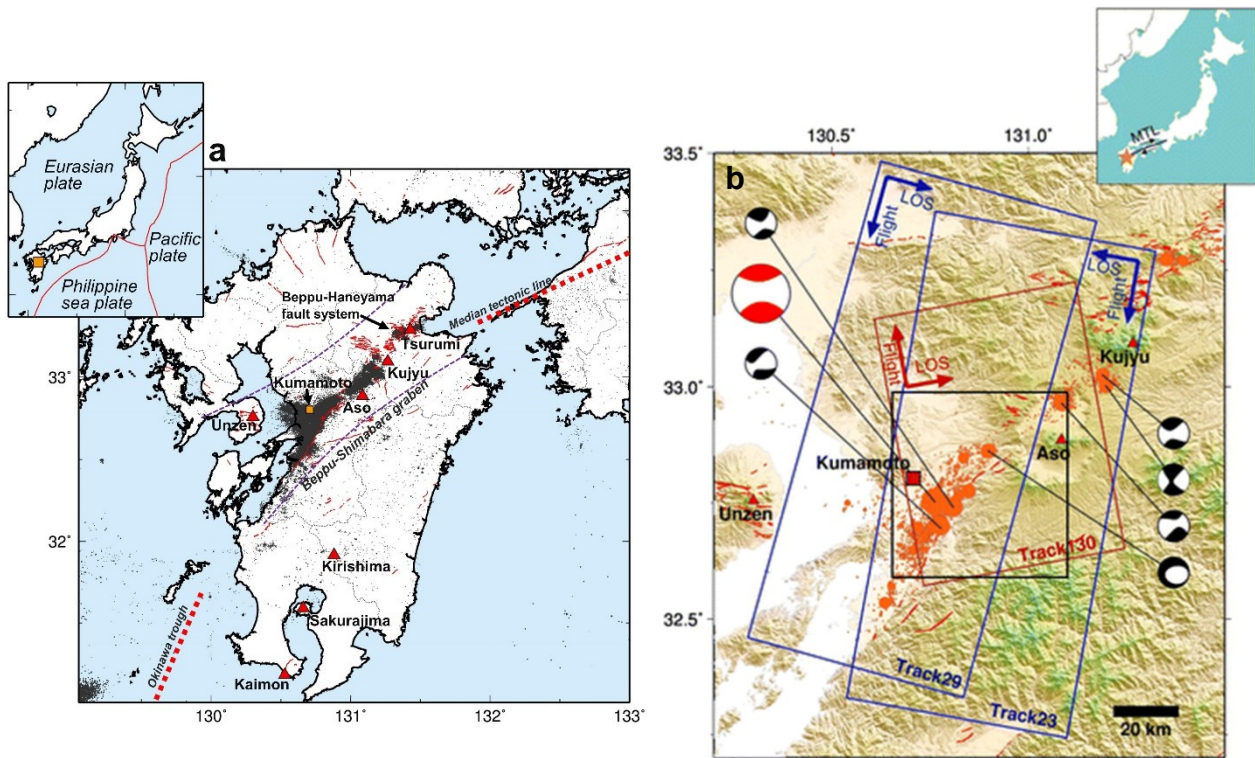


Figure 6-1. Study area in Chapter 6. (a) Japan islands with plate boundaries (red lines) in inset and Kyushu island with seismicity (grey dots) and active fault traces (red lines). Red triangles are active volcanoes across Kyushu island. (b) Orange circles indicate the locations of epicenter during 14-30 April 2014. Beachballs show each focal mechanism of earthquakes which are greater than M_w 5.5. The information of earthquake is derived from Japan Meteorological Agency (JMA) catalog.

Tectonic Line (MTL). In order to understand the mechanism of any seismic event, a variety of sources are available such as seismic wave, tsunami height, Global Navigation Satellite System (GNSS) network and SAR data. The focal mechanisms reported by JMA are based on seismological data that are acquired at distant stations from the hypocenter. Regarding the “main shock” of the Kumamoto earthquake sequences, however, it has been pointed out that another earthquake (M_{JMA} 5.7) occurred 32 s after the main shock at Yufu City, ~80 km to the NW from Kumamoto (JMA hypocenter catalog in Japanese [http://www.data.jma.go.jp/svd/eqev/data/daily_map/20160416.html]). Hence, the estimated mechanism solution based on the far-field and long-period seismic data could be biased due

to mixed-up wavelets. In contrast, co- and post-seismic displacements derived by geodetic techniques indicate permanent deformation signals in the near-field around the hypocenters, and thus, the estimated fault model could be less ambiguous, at least, in terms of the location and the geometry of these faults. Over the last two decades, a growing number of fault models have been derived from geodetic data such as GNSS and Interferometric SAR (InSAR). Regarding the 2016 Kumamoto earthquake sequences, Geospatial Information Authority of Japan (GSI) has shown first report of InSAR (Hanssen et al., 2001; Massonnet & Feigl, 1998) and Multiple Aperture Interferometry (MAI, Bechor & Zebker, 2006) observation results using the L-band ALOS-2/PALSAR-2 images (<http://www.gsi.go.jp/cais/topic160428-index-e.html>, last accessed on May 27, 2016).

In this chapter, we show the three-dimensional (3D) displacements associated with the Kumamoto earthquakes derived by applying pixel tracking technique to ALOS-2/PALSAR-2 data. Using the derived pixel tracking data, we develop a fault slip distribution model based on triangular dislocation elements in an elastic half-space and discuss its implication for the rupture processes of the 2016 Kumamoto earthquakes.

6.2 Methods and results

We processed ALOS-2/PALSAR-2 data (L-band, wavelength is 23.6 cm) acquired from stripmap mode with HH polarization at three tracks (Figure 6-1; Table 6-1), using GAMMA software (Wegmüller & Werner, 1997). Because the InSAR data were missing near the faults due to the problem in phase unwrapping, we applied pixel tracking technique to ALOS-2/PALSAR-2 data so that we could detect robust signals even if the displacement gradient was high (Kobayashi et al., 2009; Takada et al., 2009; Tobita et al., 2001). We set the window size of 32×64 pixels for range and azimuth with the sampling interval of 12×24 pixels for range and azimuth, respectively. The processing strategy in this

study is mostly the same as our previous studies (Furuya and Yasuda 2011; Abe et al. 2013). The technique originates in the precision matching of multiple images, and the local deviations from globally matched image indicate the displacements. Pixel tracking technique allows us to detect both range offset and azimuth offset. The range offset is a projection of the 3D displacements onto the local look vector from the surface to the satellite, whereas the azimuth offset is a projection of the 3D displacements along the satellite flight direction. Using the 3 pairs of ALOS-2/PALSAR-2 data (Table 1), we could obtain six displacement data projected onto six different directions (Figure 6-2). We can

Table 6-1. PALSAR-2 dataset in this chapter.

Pair No.	Track	Orbit	Date (dd.mm.yyyy)	B_perp [m]	Pixel spacing [Ran., Az. (m)]
1	23	D	03.07.2016	-122.43	1.4, 2.1
			18.04.2016		
2	130	A	03.12.2015	-147.36	2.8, 3.0
			21.04.2016		
3	29	D	14.01.2015	5.15	1.4, 1.8
			20.04.2016		

B_perp: Perpendicular component of baseline between master and slave image.

Orbit: Satellite flight direction from ascending (A) and descending (D) track.

Pixel spacing: Spatial resolution for range (Ran.) and azimuth (Az.) direction.

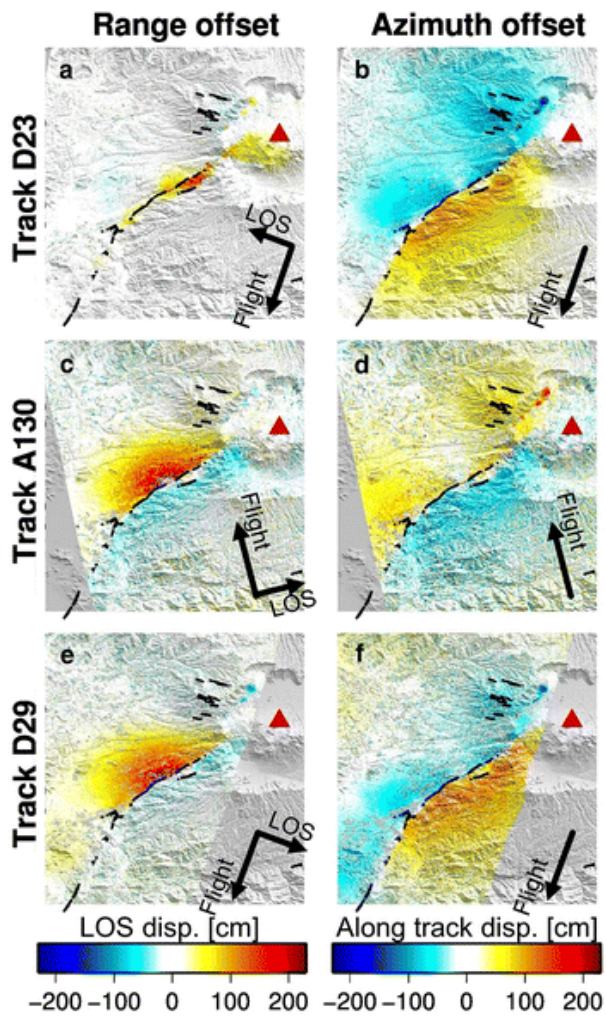


Figure 6-2. PALSAR-2 pixel tracking data which shows co-seismic displacement. (a, b) Track 23 observed from right-looking descending track. (c, d) Track 130 observed from right-looking ascending track. (e, f) Track 29 observed from left-looking descending track. Black arrows indicate each flight and line-of-sight (LOS) direction. Positive signals in range and azimuth offset show displacement along LOS away from the satellite and toward the satellite flight direction, respectively. Red triangles are the location of Mt. Aso. Black lines represent active fault traces derived from geological surveys (Nakata and Imaizumi, 2002).

identify three NE–SW trending signal discontinuities in the pixel tracking data (dotted curved lines in Figure 6-2), which we attribute to the surface faults due to the earthquake sequences and hereafter denote F1, F2 and F3, respectively. Geologically inferred fault traces by Nakata and Imaizumi (2002) are also shown in Figures 6-1 and 6-2. The longest discontinuity (NE–SW), F1, is located at a part of Futagawa fault system (Watanabe et al. 1979; Okubo and Shibuya 1993), extending from the northwestern area of the Aso caldera to Kumamoto City. Another signal discontinuity, F2, branches off from the southern part of the F1 toward SSW, which seems to be a part of Hinagu fault system (Watanabe et al. 1979). We can point out the other short signal discontinuity, F3, parallel to the F1 segment at the southwest flank of Aso caldera. The F3 segment is situated 2 km away from the longest F1 segment.

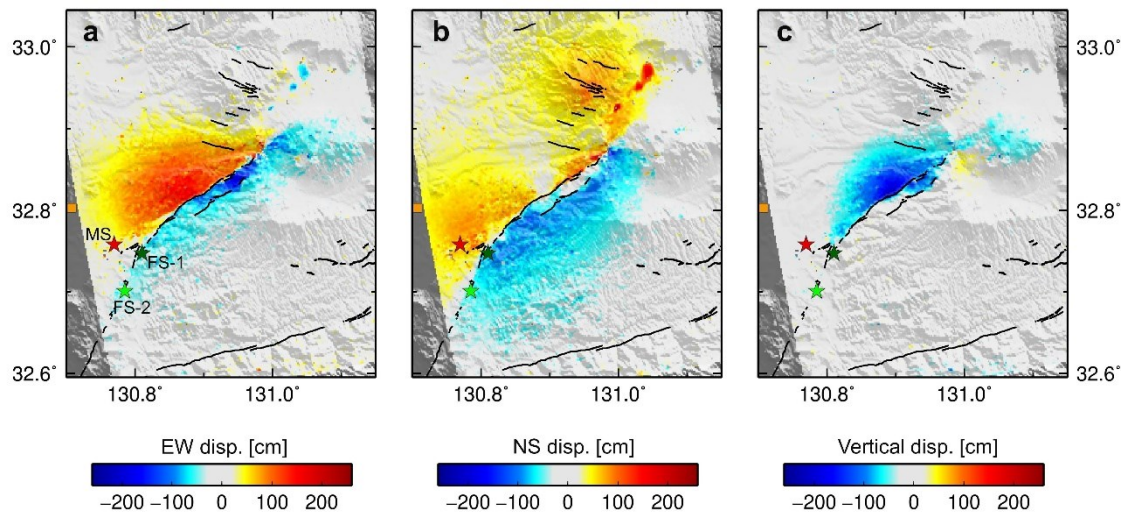


Figure 6-3. Cumulative 3D displacement inferred from our pixel tracking data of tracks 23 and 130. (a) East-west horizontal displacement, (b) North-south horizontal displacement, and (c) vertical displacement. Positive signals indicate eastward, northward, and uplift displacement, respectively. Black lines the Hinagu and Futagawa fault traces reported by Nakata and Imaizumi (2002). Black box shows the location of localized signal indicating NNE horizontal movement. Colored stars indicate the location of each centroid (Red: Mainshock, Strong and light green: Foreshocks (FS-1, FS-2)).

Based on these pixel tracking data, we derived the 3D displacement field from tracks 23 and 130 by solving an overdetermined least-squares problem without any weight functions (Figure 6-3). Although there are three available tracks, the data coverage becomes more limited when we use all the tracks (Figure 6-4), because we solved for the 3D displacement where the employed tracks are completely overlapped. Also, because the tracks 29 and 130 are viewing the surface from nearly the same look direction, we consider that the tracks 23 and 130 are the best combination to derive the 3D displacements. Considering the NE–SW striking of the F1 segment, the focal mechanism of the main shock (Mw 7.0) suggests mainly right-lateral motion with a near-vertical dip angle. Nonetheless, the northern side of the deformation area indicates significant subsidence by as much as ~200 cm (Figure 6-3). This subsidence signal can be explained by the normal faulting on NW-dipping segments, which would be plausible under the N–S extension stress field. In contrast, we could identify few uplift signals at the southern side. Besides the broadly distributed signals noted above, we can point out more

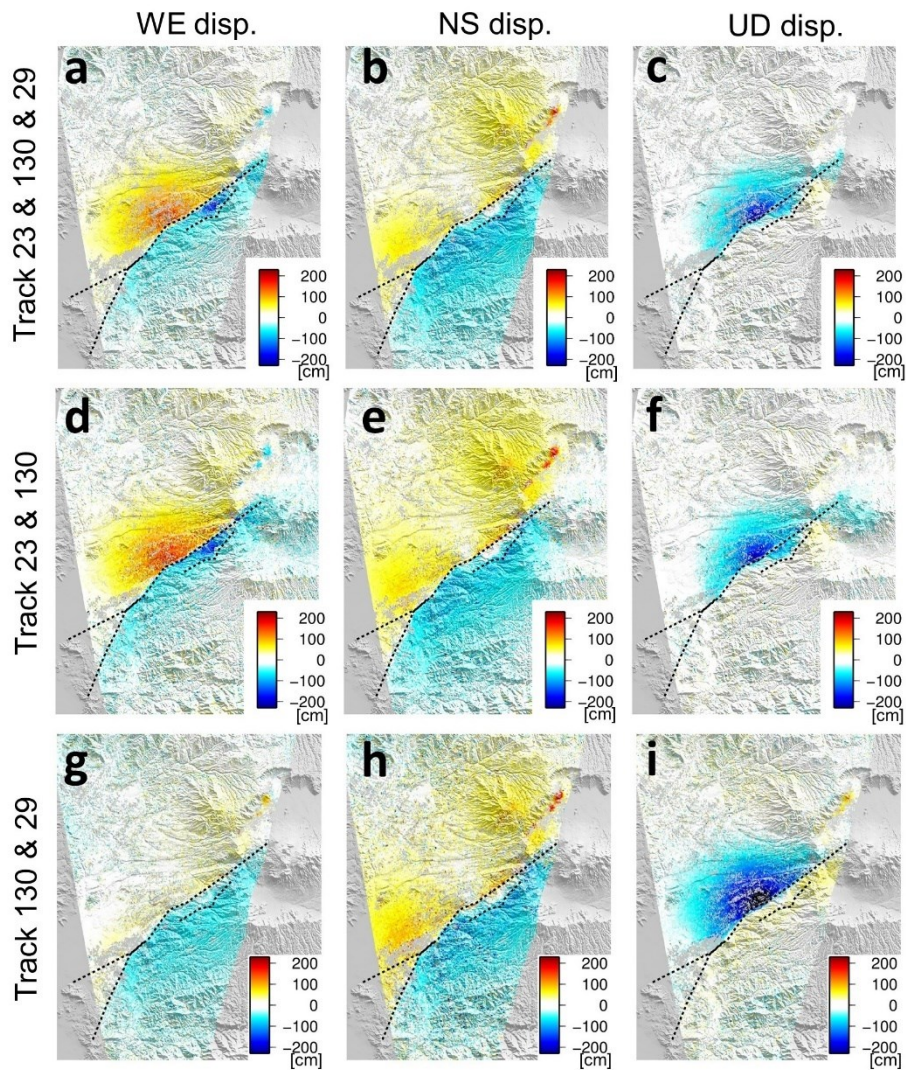


Figure 6-4. Comparison of cumulative 3D displacements inferred from three combination of PALSAR-2 pixel tracking data. The 3D displacement inferred from tracks 23, 130 and 29 (a-c), tracks 23 and 130 (d-f), and tracks 130 and 29 (g-i).

localized signals in places. We can identify the NE–SW trending patchy localized signals at the northern part of Aso caldera in the 3D displacement field (black boxes in Figure 6-3). These signals indicate ~200 cm of NNW movement with small vertical displacements. Moreover, the 3D displacements indicate subsidence signals by as much as 50 cm at the western part of Aso caldera, which is located at the eastern part of the deformation area. The detected subsidence signal significantly exceeds the empirical measurement error of pixel tracking which is 0.1 pixel in each image (e.g., Fialko et al. 2001). Moreover, the localized westward displacements can be found between

the two discontinuities (Figure 6-3a). These signals cannot be explained by the fault model below, and we provide our interpretations later on.

6.3 Fault source model

In this section, we present our fault model that can reproduce the pixel tracking data sets (Figure 6-2). Our model consists of three fault segments whose top positions trace the displacement discontinuities in the pixel tracking data (Figure 6-5). We also denote the three segments F1, F2 and F3, respectively. The bottom depths were set to be 20 km for F1 and F2 segments and 10 km for the F3 segment. Top depths of all segments are set to be surface. Each fault segment consists of triangular dislocation element, so that we can express the non-straight irregular fault trace as well as curved geometry; we use Gmsh software to construct triangular meshes (Geuzaine & Remacle, 2009). The actual parameterization of fault geometry was performed as follows: We firstly set the top locations of the faults by providing control points so that they can trace the displacement discontinuities in the observation data; shallowest part of the faults is thus non-planar. On the other hand, because of the lower resolution at greater depths, we assume that the deep part of these faults is essentially planar, and no control points for the fault plane at intermediate depths are given. The fault surface is derived by spline interpolation, based on the given control points on the top and the bottom. The location and depth of the bottom of the faults, i.e., dip angle, were derived by trial-and-error approach (Table 6-2; e.g., Furuya and Yasuda 2011; Abe et al. 2013). Based on the given location and geometry of the fault, we can solve the slip distributions as a linear problem with the constraints noted below. For the Green function, we use analytical solutions of surface displacements due to a triangular dislocation element in an elastic half-space (Meade, 2007). We assume Poisson ratio of 0.25 and crustal rigidity of 30 GPa.

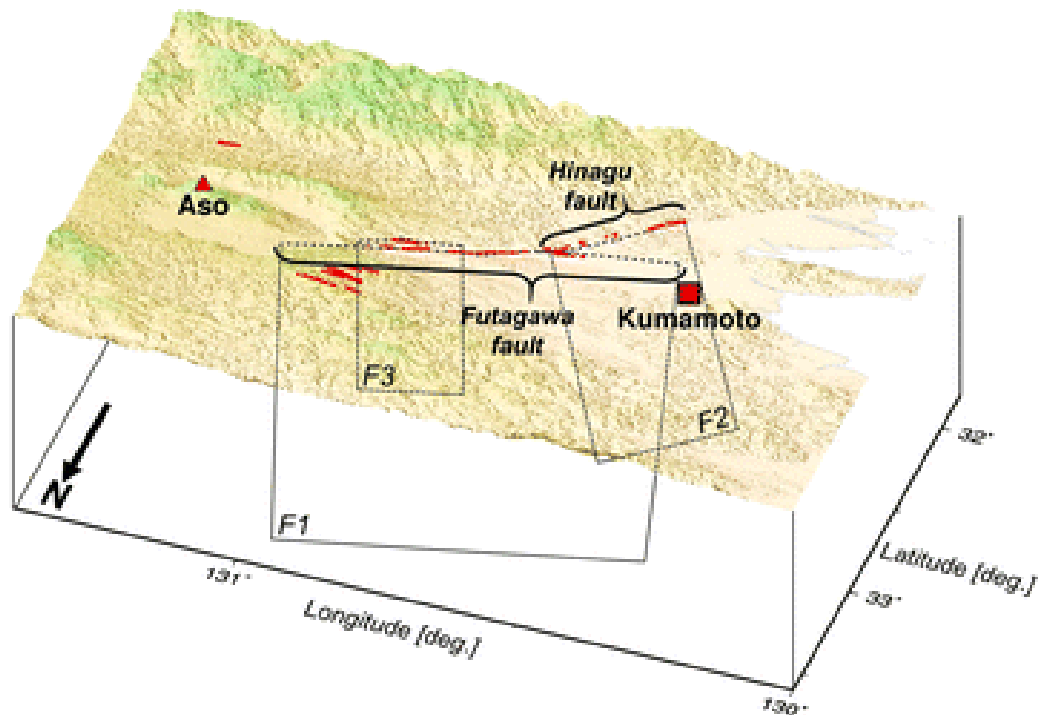


Figure 6-5. Schematic perspective of fault geometry of our inferred model viewing from NNE. Details of model parameter are shown in Table 2. Red lines indicate the traces of geological fault trace.

The size of a typical triangular mesh varies from the minimum (~1000 m) near the surface to the largest (~2000 m) toward the bottom of the segments because the resolution becomes worse at deeper depth. We applied median filter to the observed pixel tracking data to reduce noises. To invert for slip distributions on each segment that are physically plausible, we solve a non-negative least-squares problem that restricts the slip directions together with a constraint on the smoothness of the slip distributions (Furuya & Yasuda, 2011; Simons et al., 2002). Regarding the restrictions on the slip directions, whereas F1 was allowed to include both strike and normal slip, we further limited that F2 and F3 included only right-lateral and normal slip components, respectively. This is not only because we could reduce the number of degrees of freedom but also because the differences of the misfit residuals were insignificant even when we considered both slip components at F2 and F3. When F2 and F3 are allowed to include both slip components, the derived slip amplitude turned out to be less

than 15 cm. In deriving the slip distribution, we masked the before-mentioned patchy localized signals at the northern part of Aso caldera. Although the computed pixel tracking data from the estimated slip on the faults can mostly reproduce the observed displacement field, misfit residuals are still left around

Table 6-2. Parameters of our fault model

Segment No.	F1	F2	F3
Latitude [deg.]	32.82	32.77	32.82
Longitude [deg.]	130.87	130.81	130.93
Bottom [km]	20.0	20.0	10.0
Strike [deg.]	231.69	214.99	230.77
Dip [deg.]	78.69	86.51	65.61
Width [deg.]	20.0	20.0	
Length [km]	41.29	18.28	12.65
Slip constraint	Normal slip Right-lateral	Right-lateral	Normal slip
M_w (M₀ [Nm])	6.77 [1.80×10^{19}]	6.62 [1.05×10^{19}]	6.46 [0.61×10^{19}]

Latitude and Longitude present the center coordinates of top projection of faults. Slip indicates the direction of slip constraint on each fault segment. M_w is total geodetic moment release calculated by slip distribution. Top depth of all fault segments is located at surface [0 km].

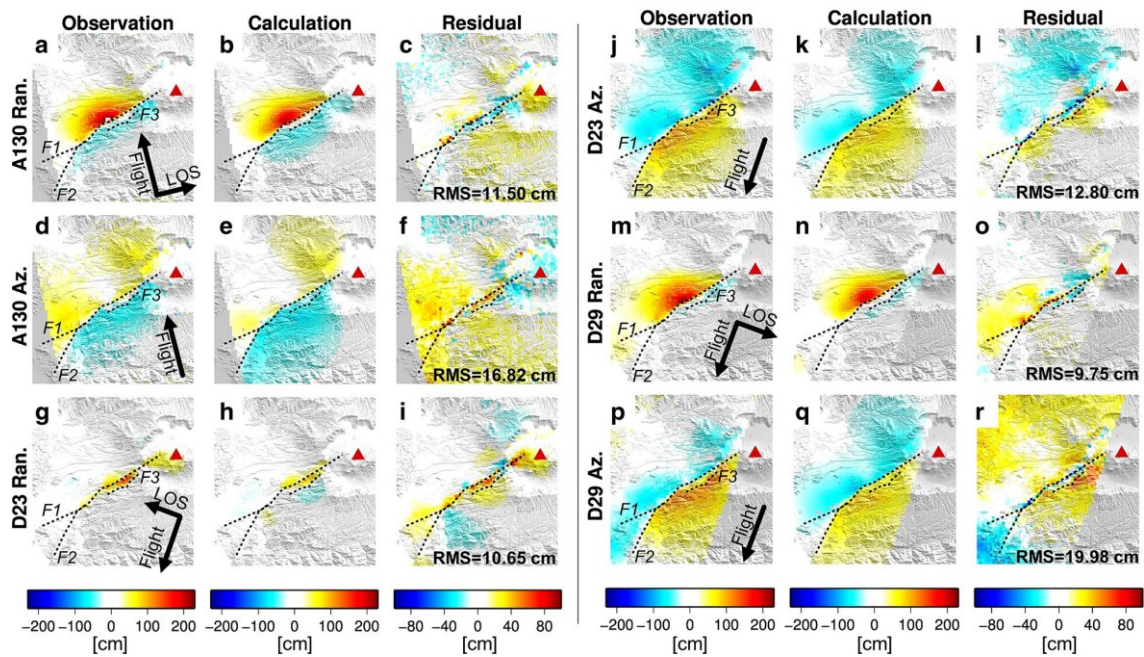


Figure 6-6. Comparison with observation of pixel-tracking data, calculation derived from our slip distribution and their residual. (a, d, g, j, m, p) Observations of pixel tracking data. (b, e, h, k, n, q) Calculated pixel tracking from our slip distribution on each segment. (c, f, i, l, o, r) Residual subtracted observation from calculation. Positive value in range offset and azimuth offset shows line-of-sight (LOS) increasing (moving away from satellite) and horizontal displacement moving toward the satellite flight direction, respectively. Color scales indicate displacement in centimeters. Red triangle marks location of Mt. Aso. Dashed lines trace the top location of the faults. Root mean square (RMS) are shown in each bottom right on residual framework.

the epicenter area, especially in the region between F1 and F3 (Figure 6-6); we discuss our interpretation later on. However, we do not further refine the fault model for now, because of the root-mean square (RMS) residual of each pixel tracking datum below 20 cm, which is largely comparable to the precisions of offset measurements (Kobayashi et al., 2009). Slip distributions in our model show the maximum right-lateral strike-slip of >5 m on F1 at a depth of 5 km and the maximum normal slip of 4.5 m on F3 at a depth of 6 km (Figure 6-7). Not only right-lateral slip but also normal slip (~2.5 m) is present on F1 segment. Because the depths of epicenters are located around 10 km according to JMA catalog, these slip distributions are nearly consistent with them. The 1-sigma uncertainties of slip distribution (Figure 6-8) were estimated from standard deviations of 200-times iterative inversions

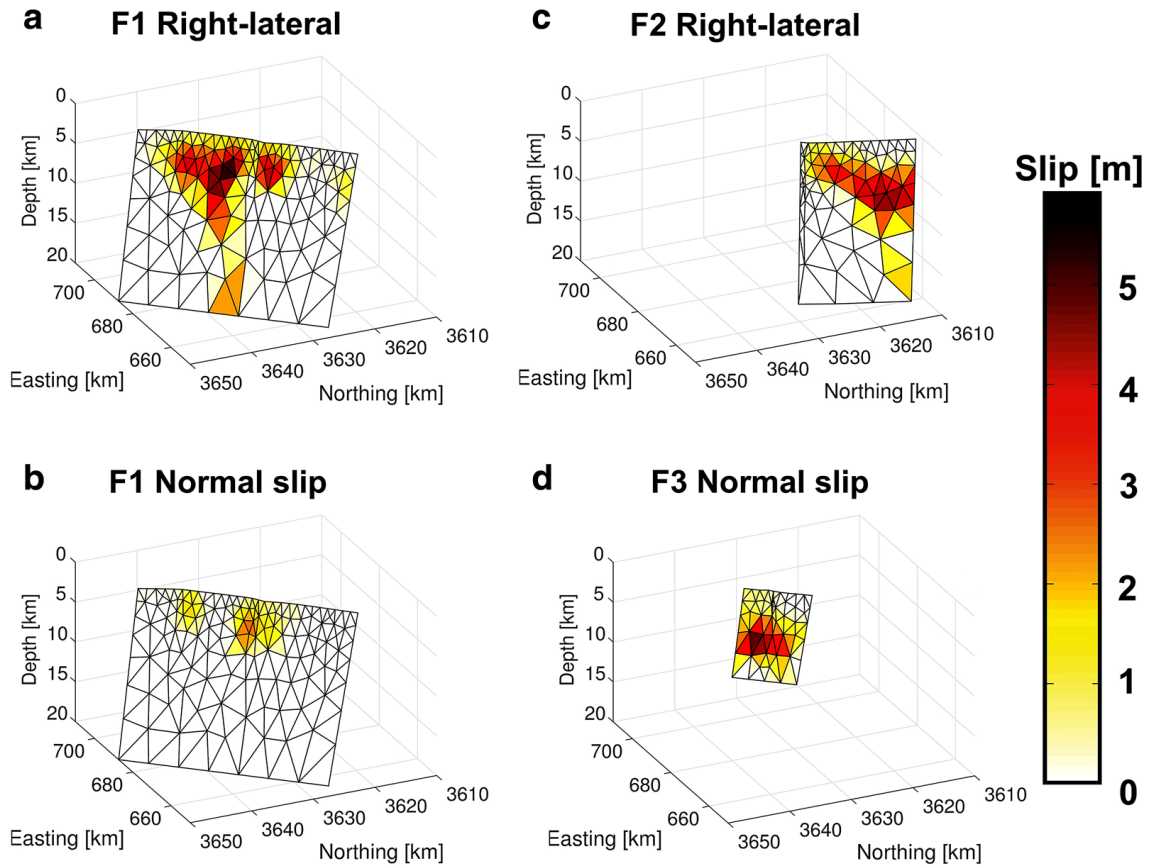


Figure 6-7. Slip distribution on each fault segment viewing from WNW. (a) Right-lateral slip on F1. (b) Normal slip on F1. (c) Right-lateral slip on F2. (d) Normal slip on F3. All figures are shown by same color scale in meters and are projected on same UTM (Universal Transverse Mercator) coordinate frame viewing from WNW (Zone 52).

with 2D correlated random noises (Furuya & Yasuda, 2011; Wright et al., 2003). Significant uncertainties are located at the lowest and side patches of fault elements, and the slip error is much less than the estimated slip amplitude. Total geodetic moment (GM) release in our fault model is 3.47×10^{19} Nm (Mw 6.96), whereas seismic moment (SM) of the main shock derived from JMA catalog is 4.06×10^{19} Nm (Mw 7.01) (Table 6-3). Although these moment release values seem to be nearly identical, we should note the differences in the details of each total moment (Table 6-3).

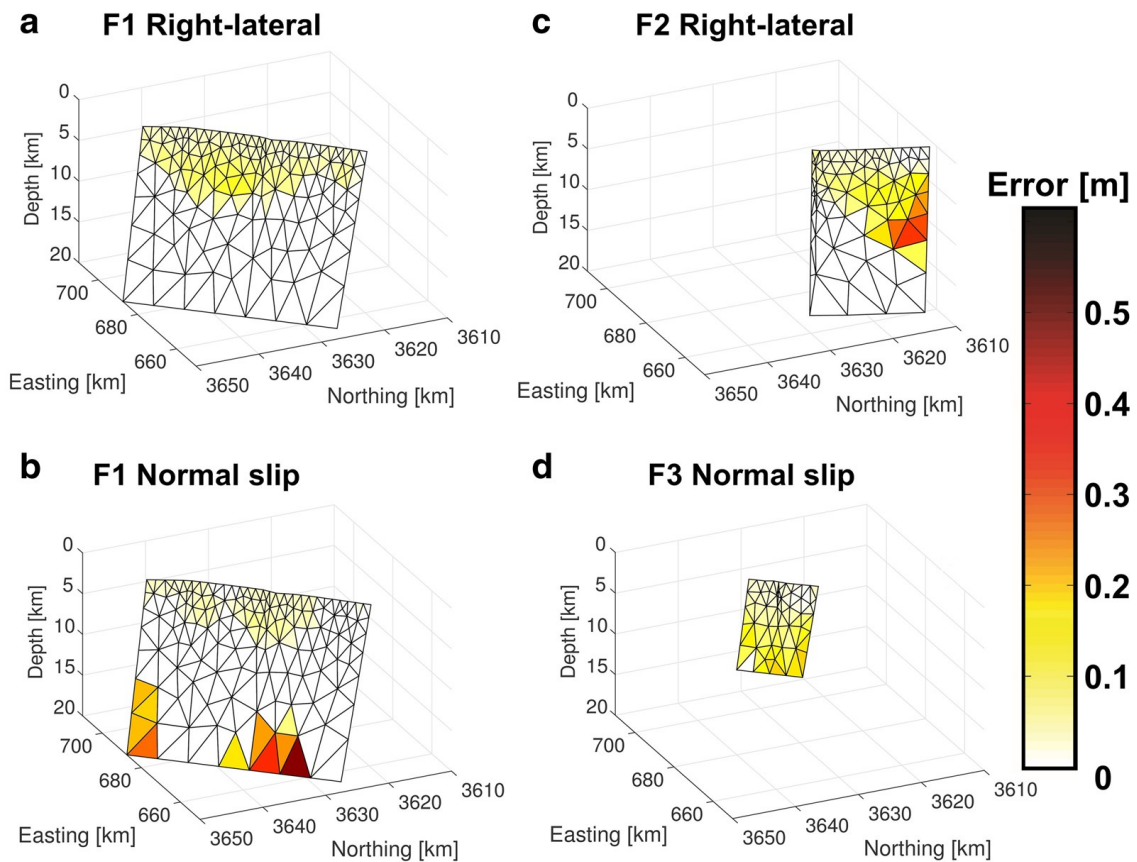


Figure 6-8. Slip 1-sigma uncertainties for each segment calculated by 200-times iteration of inversion with random noise. (a) Right-lateral slip on F1. (b) Normal slip on F1. (c) Right-lateral slip on F2. (d) Normal slip on F3. All figures are shown by same color scale in meters and are projected on same UTM coordinate frame (Zone 52).

6.4 Discussion

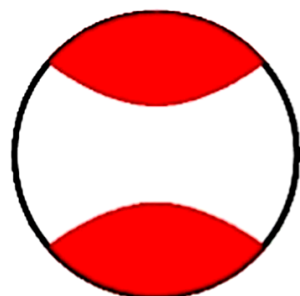
Remarkably, our fault model indicates that while the strike-slip dominates on F1 and F2, F3 is a pure normal slip fault (Figure 6-7; Table 6-3). The significant normal slip at F3 instead of at F1 could be derived, because the broad subsidence signals are located not only to the north of F1 but also between F1 and F3, and also because the deeper normal slip can explain the broader subsidence signals. Such a configuration of multiple faults is known as slip partitioning, which has been pointed out at active tectonic regions of oblique extension/compression stress regime (e.g., Bowman et al., 2003; Fitch, 1972). Our fault model thus suggests that the fault source regions are under oblique extension stress,

which is probably due to the combination of the shear stress by the western end of MTL and the extension stress associated with the backarc spreading of Okinawa trough (Nishimura and Hashimoto 2006; Ikeda et al. 2009; Matsumoto et al. 2015). Moreover, the deviation of a moment tensor from double couple, a so-called compensated linear vector dipole (CLVD) parameter ϵ , is 0.28 (JMA epicenter catalog); the ϵ could range from -0.5 to 0.5 and become zero for a perfect double couple. While a variety of interpretations on non-double couple components are possible (Julian et al., 1998), the moment tensor for the main shock by JMA provides us with such eigenvalues that can be decomposed into one normal faulting and one strike-slip earthquake on the assumption of no volume changes. Each moment release is shown in Table 6-3 as the SM, and the quoted moment by JMA is derived by $(\sigma_1 - \sigma_3)/2$, where σ_1 and σ_3 are the maximum and the minimum eigenvalues, respectively. Meanwhile, based on our slip distribution model, we computed the contribution from normal- and strike-slip faulting (Table 6-3) and the corresponding CLVD parameter (ϵ), and plotted the beach ball

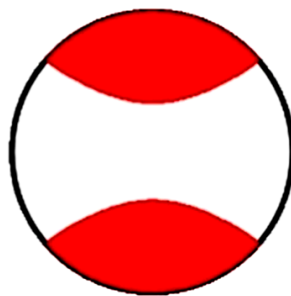
Table 6-3. Total moment release derived from the inferred fault model (GM) and JMA catalog (SM).

		Slip component	M_0 [10^{19} Nm]	M_w
GM	Total		3.47	6.96
	F1	Right-lateral	1.76	7.76
		Normal slip	0.36	6.30
	F2	Right-lateral	1.05	6.62
	F3	Normal slip	0.61	6.46
SM	Total		4.06	7.01
		Right-lateral	3.40	6.95
		Normal slip	1.32	6.68

on the assumption of simultaneous rupture events (Figure 6-9). The ε turns out to be 0.26, and the synthetic beach ball is remarkably consistent with that by JMA (Figure 6-9). Therefore, independently from the JMA's moment tensor, the slip distributions at distinct segments in our fault model suggest that both normal faulting and strike-slip earthquakes have simultaneously occurred in a single event (Kawakatsu 1991; Kikuchi et al. 1993) and that no source volume changes occurred; we may call it dynamic slip partitioning. While Kawakatsu (1991) interpreted the non-double couple components in earthquakes at ridge-transform faults as simultaneous occurrence of both normal and strike-slip at transform faults, our fault model would be the first geodetic evidence for the simultaneous rupture hypothesis of non-double couple component with no volume changes. One of the possible explanations for the differences in the moment values of each slip type could be the mix-up of the two seismic waveforms of the main shock (M_W 7.0) and another event (M_{JMA} 5.7) that occurred after 32 s at Yufu City (Kato et al., 2016). However, it is also likely due to the simple assumption of homogeneous elastic body in the estimated geodetic moment. The patchy localized signals of the NNW horizontal movements (black boxes in Figure 6-3), which were masked in the inversion, would not be explained by co-seismic landslides, because directions of the local slope and the horizontal displacements are opposite. We can speculate that these localized signals may suggest the presence of additional small faults, because some faults inside a volcanic caldera are likely to be masked by the thick volcanic ash deposits. Regarding the localized westward signals between F1 and F3, it is possible to attribute to the left-lateral slip on F3. However, the inferred left-lateral strike-slip on F3 turned out to be insignificant as mentioned before; this may be because we used pixel tracking data for the inversion. Some reports of field-based surface rupture observations indicated left-lateral offsets near the southern end of F3; the strike angles were $\sim N70W$ (e.g., http://www.ckcnet.co.jp/pdf/kumamoto_0427.pdf, in Japanese). Given these reports and the modeling results, if the westward signals have their origin in faults, they may suggest the left-lateral faults in

a Main shock (JMA)

$$\varepsilon=0.28$$

b Our model

$$\varepsilon=0.26$$

Figure 6-9. Focal mechanism of the mainshock during the episode derived from JMA catalog (a), and that derived from the inferred slip distribution (b). Both moment tensors are considered in arbitrary coordinates. Deviations of moment tensor (ε) are shown below each beachball.

between F1 and F3 which strike ~N70W in a conjugate fashion. Although, to our knowledge, there are no reports of such seismic focal mechanisms, they might have occurred at very shallow depth without generating seismic waves. Another possible interpretation would be a coseismic landslide; the local slope orientation seems to be consistent

with this scenario. Furthermore, the 3D displacement showed ~50 cm subsidence at the western part of Mt. Aso (Figure 6-3c), which cannot be explained by our fault model. One possible interpretation of the subsidence signal at Mt. Aso is a consequence by extension of the magma chamber due to the westward movement by the right-lateral earthquakes, which is analogous to the subsidence as reported over the volcanoes on the northeastern Honshu after 2011 Tohoku-oki earthquake (Takada & Fukushima, 2013). However, while an effusive volcanic eruption with gas emission was observed after the main shock of the 2016 Kumamoto earthquake sequence, the causal relationship still remains unclear.

6.5 Post-seismic deformation revealed by PALSAR-2 data

We also show additional results, the post-seismic deformation associated with the 2016 Kumamoto earthquake detected by PALSAR-2 interferograms (Figures 6-11 and 6-12). Post-seismic deformations associated with earthquakes detected by InSAR have reported by lots of papers (e.g., Moore et al.,

2017). Generally, the post-seismic deformations are driven by after-slips and viscoelastic relaxation, the temporal evolution of post-seismic deformation can be expressed by logarithmic and exponential functions. Some previous studies have reported the far-field post-seismic deformations across Kyushu island revealed by GEONET GPS network and Sentinel-1A InSAR data, and their observations were modeled by the contributions of after-slip and viscoelastic relaxation (Kato et al., 2016; Moore et al., 2017; Pollitz et al., 2017). The post-seismic deformation near the surface ruptures appeared during the earthquake sequence has not been reported. Kato et al. (2016) reported that a campaign-based GPS measurement revealed 2-3 cm of horizontal displacement, however the observation stopped on May 2016. Moore et al. (2017) also reported the velocity of LOS change detected by Sentinel-1A dataset, although their observation period finished June 2016. According to their GPS and SAR measurements, the velocity of vertical displacement was inferred of 40 mm/yr (Moore et al., 2017). As of writing this thesis, we are expecting to detect the post-seismic deformation using satellite SAR data because SAR images are accumulating for over 2 years.

Sentinel-1 satellites have been observed with shorter acquisition intervals than PALSAR-2, however shorter wavelength microwaves are easier to cause decorrelation problem. Because most part of Kyushu island is covering with dense vegetation, longer wavelength microwave, such as PALSAR-2, is suitable for observing crustal deformation by InSAR. PALSAR-2 dataset and their footprints for detecting post-seismic deformations are shown in Table 6-4. We employed the conventional stacking approach to detect small crustal deformation and to mitigate artificial signal derived from tropospheric effects (e.g., Wright et al., 2001). Although we applied multiple aperture radar interferometry (MAI) approach to PALSAR-2 dataset, we could not distinguish significant deformation signal from the decorrelation noise. After PALSAR-2 interferograms were stacked, we decomposed quasi-eastwest (QEW) and quasi-vertical (QUD) displacements using stacked PALSAR-2 interferograms

Table 6-4. PALSAR-2 dataset for detecting the post-seismic deformation

Track	Acquisition date [dd.mm.yyyy]	B_perp [m]
A130	21.04.2016	0
	05.05.2016	57.3
	11.08.2016	136.9
	13.07.2017	90.1
	05.10.2017	215.1
A131	26.04.2016	0
	10.05.2016	362.1
	19.07.2016	191.9
	06.12.2016	389.6
	14.03.2017	116.5
	13.02.2018	287.3
	03.07.2018	296.7
	28.08.2018	222.5
D20	17.04.2016	0
	01.05.2016	90.9
	09.07.2017	46.2
	17.09.2017	-81.4

Track	Acquisition date [dd.mm.yyyy]	B_perp [m]
D23	18.04.2016	0
	16.05.2016	246.1
	13.06.2016	-38.7
	11.07.2016	21.1
	08.08.2016	-5.7
	19.09.2016	-114.5
	14.11.2016	-160.6
	13.11.2017	2.7
	05.03.2018	336.8
	20.08.2018	-52.4
	15.10.2018	-126.1

Track indicates the identification orbit numbers. All images are acquired from a right-looking geometry. *B_perp* indicates the perpendicular component of spatial baseline between two SAR images. Each *B_perp* value is shown with a reference of a first image.

observed from ascending and descending tracks with assuming few north-southward sensitivity in InSAR (Fujiwara et al., 2000). We processed PALSAR-2 images acquired from two independent ascending tracks (Track 130 and 131) and two descending track (Track 23) by using GAMMA software. We employed an adaptive filter with a parameter of 0.6 and a window size of 32 pixels to avoid phase unwrapping error (Goldstein & Werner, 1998). The interferograms were unwrapped phase using minimum cost flow algorithm (Costantini, 1998). Topography-corrected signals were corrected by the 10 m digital elevation model (DEM) which is provided by the Geospatial Information Authority in Japan. Long wavelength phase changes across the data were corrected by fitting 2D polynomial functions.

Figure 6-11 shows cumulative LOS changes revealed by stacked PALSAR-2 interferogram

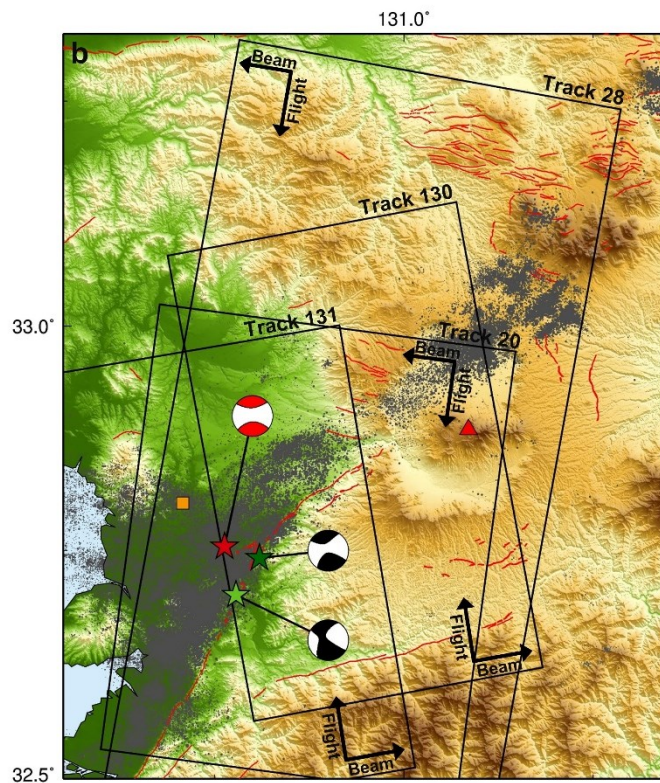


Figure 6-10. Study area and PALSAR-2 footprints for detecting post-seismic crustal deformation. Red lines mark active fault traces inferred by geological survey (Nakata and Imaizumi, 2002). Black boxes indicate coverages of PALSAR-2 image. Colored stars locate epicenters in the mainshock (red), and two foreshocks (green). Beach balls are focal mechanisms of each event. Grey dots represent a distribution of epicenters during 14-30 April 2014. Information of earthquake are derived from Japan Meteorological Agency catalog. Red triangle marks Aso volcano.

after the earthquake sequence for over one year. The cumulative LOS changes show signal discontinuities along the geological fault traces reported by Nakata and Imaizumi (2002) (Black lines in Figure 6-11). The descending interferogram shows +12 cm of maximum LOS change along the Futagawa fault where we set the top locations of F1 and F3 in our model, and the zonal positive signal is observed along the Futagawa fault toward SW (Figure 6-11b). Both outside of the zonal positive signal represents negative signal, although the signal sign changes across the surface rupture along the Futagawa fault. Another signal characteristic is that ~10 cm of positive signal broadly distributes across Aso caldera. The two-independent stacked-interferograms observed from ascending track show

similar signal characteristics, although the observation period in Track 130 is 10 months shorter than that in Track 131. We found significant a signal discontinuity along the Hinagu fault, and ~ 10 cm of negative signal near the northeastern part of Futagawa fault. To understand the detail description of the post-seismic deformation, we infer the QEW and QUD displacements, named the 2.5-dimensional analysis (Fujiwara et al., 2000). We inferred two independent QEW and QEW displacements using pairs of Track A130 and D23 (Figures 6-12a and 6-12b), and Track A131 and D23 (Figures 6-11c and 6-11d) for compensating sensitivity of LOS change, because each incidence angles are different. Same signal characteristics between each analysis data would be plausible, while differences of signal characteristics can be artificial error induced by residuals of correcting tropospheric artifacts and long wavelength signal. Above the Aso caldera, westward displacements with a NE-SW signal discontinuity at the northwest part of the Aso caldera and subsidence at the west part of the caldera were observed. The NE-SW signal discontinuity was also observed in the co-seismic displacement. Although the subsidence around the summit of Mt. Aso was also detected in the co-seismic deformation, we can find patch-shaped subsidence signals at the northwestern rim of the caldera in Figure 6-11b. The co-seismic deformation represented the similar distribution of horizontal displacement with few vertical displacements there (Figure 6-3c). At outside of the southwestern part of the Aso caldera, ~10 cm of uplift is distributed in the QUD displacement (Figures 6-12b and 6-12d). The co-seismic deformation detected few uplifts across the Futagawa fault and significant subsidence at the northern half of the displacement field. We also find that a zonal subsidence is extending toward southwest along the Futagawa fault and that a branch of zonal subsidence is distributed toward Kumamoto city. On the other hands, the QEW displacements show the similar trends of the co-seismic displacement, indicating eastward displacement at the north side across the fault trace and westward displacement at the detachment between Futagawa and Idenokuchi fault. We also find ENE-WSW discontinuity of westward movement at the southern part of the displacement field.

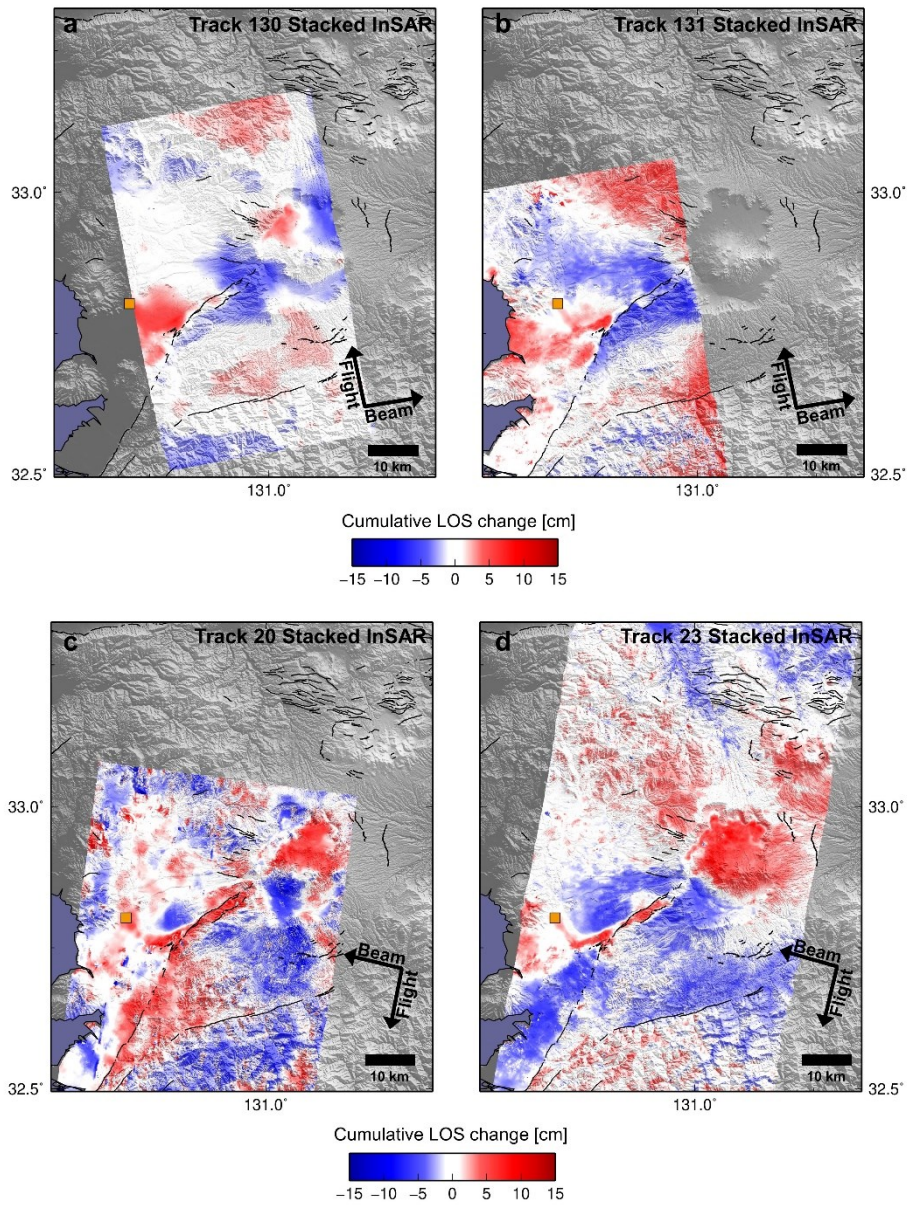


Figure 6-11. Stacked PALSAR-2 InSAR after the mainshock. Cumulative LOS changes derived from the conventional InSAR stacking approach in Track 20 (a), Track 23 (b), Track 130 (c), and Track 131 (d), respectively. Positive signal indicates LOS lengthening, indicating displacements away from the satellite. Black solid lines show geological traces of active faults reported by Nakata and Imaizumi (2002). Orange box is the location of Kumamoto city.

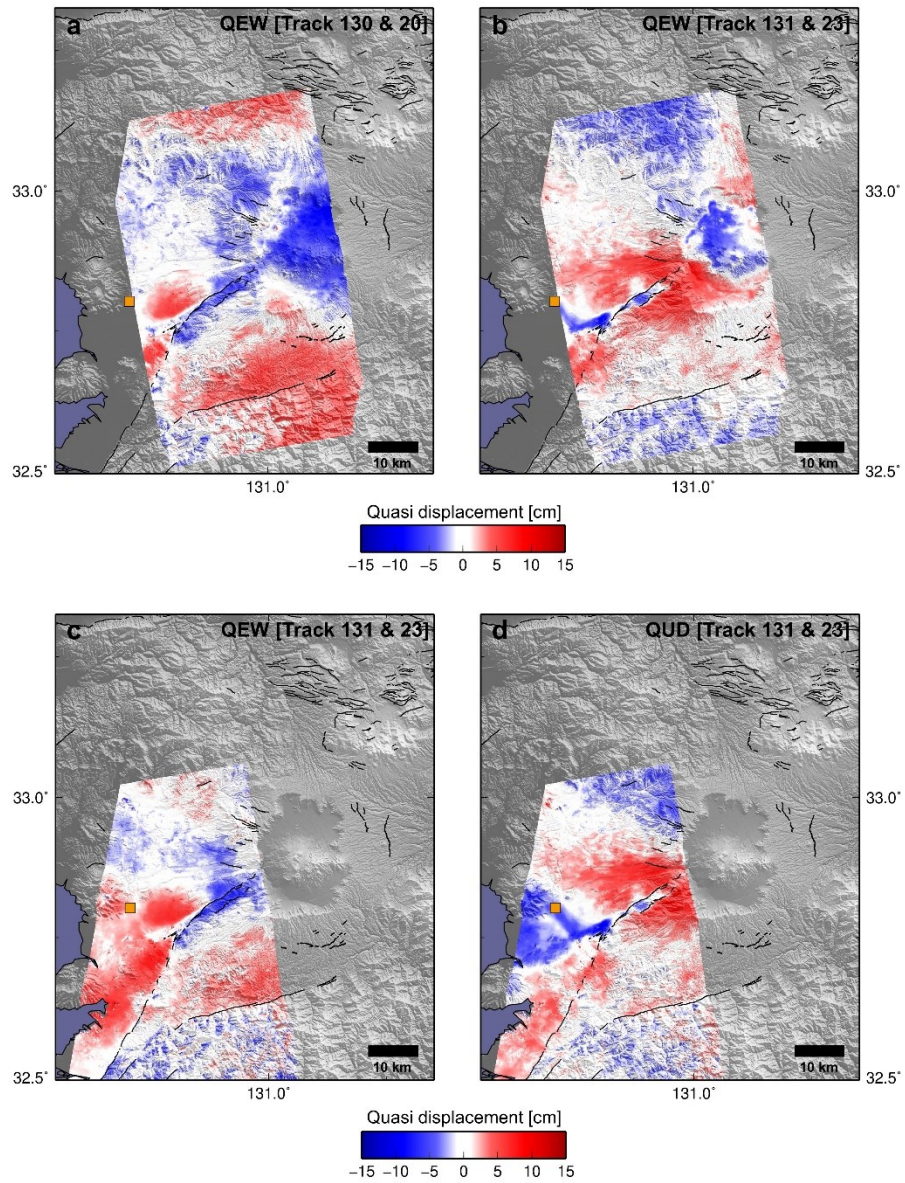


Figure 6-12. Cumulative quasi-displacements derived from the stacked PALSAR-2 interferograms. (a) Quasi-eastwest and (b) Quasi-vertical displacements inferred from the Track 20 and 130 InSAR. (c) Quasi-eastwest and (d) Quasi-vertical displacements inferred from Track 23 and 131 InSAR, respectively. Positive signals indicate quasi-eastward displacements and quasi-uplift displacements, respectively. Details are same in Figure 6-11.

Chapter 7

Thesis Findings and Conclusions

Chapter 7. Thesis findings and conclusions

This thesis has reported the crustal deformations revealed by satellite SAR data and their elastic models associated with three dike intrusions and one earthquake episode. It has been confirmed that most of the episodes considered in this thesis occurred along the subaerial rifts and at shallower depths of crust. The observed crustal deformations induced surface break formations, indicating dislocations at the shallowest part of faults. Although InSAR is the most well-known SAR analysis method for mapping crustal deformations with high measurement accuracy, revealing crustal deformations around surface ruptures derived from InSAR is currently challenging because of decorrelation problems. The decorrelation problems usually induce missing data around surface ruptures resulting in the loss of important information concerning crustal deformation associated with the episode. In this thesis, it was confirmed that the pixel tracking data depicted robust deformation signals associated with the 2005 Afar dike intrusion episode, the 2014-2015 Bárðarbunga dike intrusion episode, and the 2016 Kumamoto earthquake sequence through comparison with the InSAR data for each episode. Although the interferograms for each episode showed missing data around the surface ruptures due to decorrelation problems, the pixel tracking data revealed robust deformation signals with fewer missing data. Therefore, it can be concluded that the cross-correlation-based pixel tracking approach is suitable for detecting crustal deformation with fewer missing data. In case of the crustal deformation scale being greater than $1/10$ pixels of spatial resolution the SAR images contain significant surface ruptures. Clearly, the pixel tracking is not a comprehensive SAR analysis method for detecting surface movement even if the scale of surface movement is greater than one meter, an issue faced in Chapter 5. An attempt was made to infer the subglacial crustal deformation from icecap surface movements associated with the subglacial dike intrusion. The pixel tracking identified correlated signals only at the edge of icecap, not at the higher part of the icecap and around the Bárðarbunga caldera. This was

despite using various different parameters such as thresholds of cross-correlation and window size for identifying plausible signals. Because the method is usually used for estimating glacier flow velocity, it was initially anticipated that the signal would be detectable using pixel tracking. However, the signal could not be detected in this manner. The reasons are discussed in Chapter 5.

The concluding remarks for each episode are as follow.

In Chapter 3, the crustal deformation associated with the 2007 Natron dike intrusion episode in Tanzania was detected using PALSAR-1 data. In addition to the two-pass InSAR data from both ascending and descending paths, the azimuth offset data was derived that are sensitive to the displacements parallel to the satellite flight direction. Thus, the 3D displacement fields were demonstrated. In addition to the graben-like structure already highlighted in the previous studies, the 3D displacement fields indicate that the subsidence zone moved in a SSW direction. The fault source model used here consists of one tensile-opening fault, one east-dipping fault, and two west-dipping faults. One notable difference in the fault model with previous studies is the presence of a strike-slip component that turns to contribute to approximately 20% of the whole moment release. Because the focal mechanisms of the earthquakes during the 2007 swarm event represent nearly pure normal faulting, it was assumed that aseismic strike-slip on the faults is responsible for the horizontal movement of the subsidence zone.

In Chapter 4, the post-2007 PALSAR pixel-offset and MAI data detected block-like horizontal displacements parallel to the rift axis on the graben floor of as much as ~1 m during the 2005-2010 Afar rifting episode. The elastic fault model was able to reproduce the rift-parallel displacements by aseismic strike-slip on the graben-bounding faults. Stepping away from the elastic dislocation model and following the rheologically consistent numerical model of the plume-

lithosphere interaction, it may be speculated that the rift-parallel displacements in both Natron and Afar rifting episodes could be passive responses of the upper crust to the underlying horizontal sill-like flow of plume material.

In Chapter 5, the possibility of isolating subglacial crustal deformations due to the dike intrusion under an icecap using satellite SAR data was evaluated. The CSK, TSX, and RS2 pixel tracking results revealed the ice flow and crustal deformations associated with the Bárðarbunga dike intrusion episode in 2014. The subglacial crustal deformations were inferred by correcting the icecap signal, by subtracting the scaled pre-diking signals from the co-diking signals. The icecap signals were well-corrected in terms of the range offset, while some residuals remained in the azimuth offset. The optimal elastic model without shearing along the dike could not reproduce the ice-corrected signals at the southern part of the dike completely. However, comparison of models with and without input data above the icecap confirmed that the ice-corrected signals effectively improved the elastic model with dike opening and fault slip. The SAR pixel tracking depicts crustal deformations associated with subglacial eruptions and/or subglacial dike intrusions in the Polar regions (and/or at high altitude regions) where ice covers the ground.

In Chapter 6, the results of pixel tracking applied to ALOS-2/PALSAR-2 data indicated three displacement discontinuities that were considered as the surface traces of the main source faults associated with the 2016 Kumamoto earthquake sequence. Consequently, a fault slip distribution model was constructed containing three segments: F1 and F3 belonging to the Futagawa fault system, and F2 belonging to the Hinagu fault system. The inferred slip distributions at each segment indicate that while the strike-slip is dominant at the shallower depths of F1 and F2, only normal faulting is significant at the greater depth of F3. This suggests the occurrence of slip partitioning during the

earthquake sequence. Using the slip distribution, the focal mechanism and the CLVD parameter were computed, which was consistent with those derived from the seismic focal mechanism. Hence, it can be concluded that the significant non-double couple components in the reported seismic focal mechanisms were due to dynamic slip partitioning through by simultaneous occurrence of strike-slip and normal slip at the distinct segments. The post-seismic deformation until October 2018 revealed by the conventional stacking for PALSAR-2 interferograms is also reported.

Pixel tracking strongly depends on image spatial resolutions and had been found to have provided data with lower measurement accuracy than InSAR data. However, improvement in the measurement accuracy of the pixel tracking was expected because the spatial resolution of recent satellite SAR data is higher. The main focus in this thesis on the co-seismic and co-diking crustal deformations at the subaerial rifts. However, the time-series analysis can reveal long-lasting deformations after episodes due to the post-seismic and the post-diking processes, such as after-slip, viscoelastic relaxation, and aseismic magma intrusions. These processes are also helpful to understand strain fields and inhomogeneous structures at rift zones.

Bibliography

- Abe, T., Furuya M., Takada Y. (2013). Nonplanar fault source modeling of the 2008 Iwate-Miyagi inland earthquake (MW 6.9) in Northeast Japan. *Bulletin of the Seismological Society of America*, 103, 507-518.
- Ágústsdóttir, T., Woods, J., Greenfield, T., Green, R. G., White, R. S., Winder, T., et al. (2016). Strike-slip Faulting During the 2014 Bárðarbunga-Holuhraun Dike Intrusion, Central Iceland. *Geophysical Research Letters*, 43, 1–9.
- Albaric, J., Perrot, J., Déverchère, J., Deschamps, A., Le Gall, B., Ferdinand, R. W., et al. (2010). Contrasted seismogenic and rheological behaviours from shallow and deep earthquake sequences in the North Tanzanian Divergence, East Africa. *Journal of African Earth Sciences*, 58(5), 799–811.
- Albers, M., & Christensen, U. R. (2001). Channeling of plume flow beneath mid-ocean ridges. *Earth and Planetary Science Letters*, 187, 207–220.
- Amer, R., Mohamed, S., Robert, R., & John, E. (2012). Structural architecture for development of marginal extensional sub-basins in the Red Sea Active Rift Zone. *International Journal of Geoscience*, 2012(February), 133–152.
- Antonello, G., Casagli, N., Farina, P., Leva, D., Nico, G., Sieber, A. J., & Tarchi, D. (2004). Ground-based SAR interferometry for monitoring mass movements. *Landslides*, 1(1), 21–28.
- Aoki, Y. (1999). Imaging Magma Transport During the 1997 Seismic Swarm off the Izu Peninsula, Japan. *Science*, 286(5441), 927–930. Retrieved from
- Baer, G., & Hamiel, Y. (2010). Form and growth of an embryonic continental rift: InSAR observations and modelling of the 2009 western Arabia rifting episode. *Geophysical Journal International*, 182, 155–167. <https://doi.org/10.1111/j.1365-246X.2010.04627.x>
- Baer, G., Hamiel, Y., Shamir, G., & Nof, R. (2008). Evolution of a magma-driven earthquake swarm and triggering of the nearby Oldoinyo Lengai eruption, as resolved by InSAR, ground observations and elastic modeling, East African Rift, 2007. *Earth and Planetary Science Letters*, 272(1–2), 339–352.
- Baran, I., Stewart, M., & Claessens, S. (2005). A new functional model for determining minimum and maximum detectable deformation gradient resolved by satellite radar interferometry. *IEEE Transactions on Geoscience and Remote Sensing*, 43(4), 675–682.
- Bastow, I. D., Nyblade, A. A., Stuart, G. W., Rooney, T. O., & Benoit, M. H. (2008). Upper mantle seismic structure beneath the Ethiopian hot spot: Rifting at the edge of the African low-velocity anomaly. *Geochemistry, Geophysics, Geosystems*, 9(12).
- Bechor, N. B. D., & Zebker, H. A. (2006). Measuring two-dimensional movements using a single InSAR pair. *Geophysical Research Letters*, 33(16), L16311.
- Belachew, M., Ebinger, C., & Coté, D. (2013). Source mechanisms of dike-induced earthquakes in the dabbahu-Manda Hararo rift segment in Afar, Ethiopia: Implications for faulting above dikes.

-
- Geophysical Journal International*, 192(3), 907–917.
- Berardino, P., Fornaro, G., Lanari, R., & Sansosti, E. (2002). A new algorithm for surface deformation monitoring based on small baseline differential SAR interferograms. *IEEE Transactions on Geoscience and Remote Sensing*, 40(11), 2375–2383.
- Biggs, J., Amelung, F., Gourmelen, N., Dixon, T. H., & Kim, S. (2009). InSAR observations of 2007 Tanzania rifting episode reveal mixed fault and dyke extension in an immature continental rift. *Geophysical Journal International*, 179(1), 549–558.
- Bird, P., An updated digital model of plate boundaries, *Geochemistry Geophysics Geosystems*, 4(3), 1027, doi:10.1029/2001GC000252, 2003.
- Bjornsson, H., & Einarsson, P. (1990). Volcanoes beneath Vatnajokull, Iceland: Evidence from radio echo-sounding, earthquakes and jokulhlaups. *Jokull*, 40, 147–167.
- Bowman, D., King, G., & Tapponnier, P. (2003). Slip partitioning by elastoplastic propagation of oblique slip at depth. *Science*, 300(5622), 1121–1123.
- Brcic, R., Parizzi, A., Eineder, M., Bamler, R., & Meyer, F. (2010). Estimation and compensation of ionospheric delay for SAR interferometry. *International Geoscience and Remote Sensing Symposium (IGARSS)*, (3), 2908–2911.
- Calais, E., D’Oreye, N., Albaric, J., Deschamps, A., Delvaux, D., Déverchère, J., et al. (2008). Strain accommodation by slow slip and dyking in a youthful continental rift, East Africa. *Nature*, 456(7223), 783–788.
- Casu, F., & Manconi, A. (2016). Four-dimensional surface evolution of active rifting from spaceborne SAR data. *Geosphere*, 12(3), 697–705.
- Chorowicz, J. (2005). The East African rift system. *Journal of African Earth Sciences*, 43, 379–410.
- Commins, D., Gupta, S., & Cartwright, J. (2005). Deformed streams reveal growth and linkage of a normal fault array in the Canyonlands graben, Utah. *Geological Society of America*, 33(8), 645–648.
- Coffin, M.F., Gahagan, L.M., and Lawver, L.A., 1998, Present-day Plate Boundary Digital Data Compilation. University of Texas Institute for Geophysics Technical Report No. 174, pp. 5.
- Costantini, M. (1998). A novel phase unwrapping method based on network programming. *Geoscience and Remote Sensing, IEEE Transactions On*, 36(3), 813–821.
- Crider, J. G., & Pollard, D. D. (1998). Fault linkage: Three-dimensional mechanical interaction between echelon normal faults. *Journal of Geophysical Research*, 103(B10), 24373–24391.
- Delvaux, D., & Barth, A. (2010). African stress pattern from formal inversion of focal mechanism data. *Tectonophysics*, 482, 105–128.
- DeMets, C., Gordon, R. G., & Argus, D. F. (2010). Geologically current plate motions. *Geophysical Journal International*, 181(1), 1–80.
- Dieterich, J. H. (1979). Modeling of rock friction: 1. Experimental results and constitutive equations.

- Journal of Geophysical Research*, 84(9), 2161–2168.
- Drouin, V., Sigmundsson, F., Ófeigsson, B. G., Hreinsdóttir, S., Sturkell, E., & Einarsson, P. (2017). Deformation in the Northern Volcanic Zone of Iceland 2008–2014: An interplay of tectonic, magmatic, and glacial isostatic deformation. *Journal of Geophysical Research: Solid Earth*, 122(4), 3158–3178.
- Ebinger, C. (1989). Tectonic development of the western branch of the East African rift system. *Geological Society of America Bulletin*, (7).
- Ebinger, C., Ayele, A., Keir, D., Rowland, J., Yirgu, G., Wright, T., et al. (2010). Length and timescales of rift faulting and magma intrusion: the Afar Rifting Cycle from 2005 to present. *Annual Review of Earth and Planetary Sciences*, 38, 439–466.
- Ehara, S. (1992). Thermal structure beneath Kuju, central Kyushu, Japan. *Journal of Volcanology and Geothermal Research*, 54, 107–115.
- Eibl, E. P. S., Bean, C. J., Vogfjörð, K. S., Ying, Y., Lokmer, I., Möllhoff, M., & Pálsson, F. (2016). Silent Magma Flow Follows Tremor-rich shallow dyke formation: Bárðarbunga eruption, Iceland. *Nature Geoscience*, (April).
- Fahnestock, M., Scambos, T., Moon, T., Gardner, A., Haran, T., & Klinger, M. (2016). Rapid large-area mapping of ice flow using Landsat 8. *Remote Sensing of Environment*, 185, 84–94.
- Farr, T. G., Rosen, P., Caro, E., & Crippen, R. (2007). The shuttle radar topography mission. *Reviews of Geophysics*, 45(2004), 1–33.
- Ferretti, A., Prati, C., & Rocca, F. (2000). Nonlinear subsidence rate estimation using permanent scatterers in differential SAR interferometry. *IEEE Transactions on Geoscience and Remote Sensing*, 38(5), 2202–2212.
- Ferretti, A., Prati, C., & Rocca, F. (2001). Permanent scatterers in SAR interferometry. *IEEE Transactions on Geoscience and Remote Sensing*, 39(1), 8–20.
- Fialko, Y., Khazan, Y., & Simons, M. (2001). Deformation due to a pressurized horizontal circular crack in an elastic half-space, with applications to volcano geodesy. *Geophysical Journal International*, 146(1), 181–190.
- Fitch, T. J. (1972). Plate convergence, transcurrent faults, and internal deformation adjacent to Southeast Asia and the western Pacific. *Journal of Geophysical Research*, 77(23), 4432–4460.
- Fujiwara, S., Nishimura, T., Murakami, M., Nakagawa, H., Tobita, M., & Rosen, P. a. (2000). 2.5-D surface deformation of M6.1 earthquake near Mt Iwate detected by SAR interferometry. *Geophysical Research Letters*, 27(14), 2049–2052.
- Fukuda, Y., Itahara, M., Kusumoto, S., Higashi, T., Takemura, K., Mawatari, H., et al. (2000). Crustal movements around the Beppu Bay area, East-Central Kyushu, Japan, observed by GPS 1996–1998. *Earth, Planets and Space*, 52, 979–984.
- Fukushima, Y., Cayol, V., Durand, P., & Massonnet, D. (2010). Evolution of magma conduits during the

-
- 1998–2000 eruptions of Piton de la Fournaise volcano, Réunion Island. *Journal of Geophysical Research*, 115(B10), B10204.
- Furuya, M., & Yasuda, T. (2011). The 2008 Yutian normal faulting earthquake (Mw 7.1), NW Tibet: Non-planar fault modeling and implications for the Karakax Fault. *Tectonophysics*, 511(3–4), 125–133.
- Furuya, M., Suzuki, T., Maeda, J., & Heki, K. (2017). Midlatitude sporadic-E episodes viewed by L-band split-spectrum InSAR. *Earth, Planets and Space*, 69(1), 175.
- Galezcka, I., Sigurdsson, G., Eiriksdottir, E. S., Oelkers, E. H., & Gislason, S. R. (2016). The chemical composition of rivers and snow affected by the 2014/2015 Bárðarbunga eruption, Iceland. *Journal of Volcanology and Geothermal Research*, 316, 101–119.
- Geuzaine, C., & Remacle, J.-F. (2009). Gmsh: A 3-D finite element mesh generator with built-in pre- and post-processing facilities. *International Journal for Numerical Methods in Engineering*, 79(11), 1309–1331.
- Goldstein, R. M., & Werner, C. L. (1998). Radar interferogram filtering for geophysical applications. *Geophysical Research Letters*, 25(21), 4035.
- Goldstein, R. M., Zebker, H. a., & Werner, C. L. (1988). Satellite radar interferometry: Two-dimensional phase unwrapping. *Radio Science*, 23(4), 713–720.
- Gomba, G., Parizzi, A., De Zan, F., Eineder, M., & Bamler, R. (2016). Toward operational compensation of ionospheric effects in SAR interferograms: The split-spectrum method. *IEEE Transactions on Geoscience and Remote Sensing*, 54(3), 1446–1461.
- Grandin, R., Socquet, A., Binet, R., Klinger, Y., Jacques, E., De Chabalier, J. B., et al. (2009). September 2005 Manda hararo-dabbahu rifting event, Afar (Ethiopia): Constraints provided by geodetic data. *Journal of Geophysical Research*, 114, B08404.
- Grandin, R., Socquet, A., Jacques, E., Mazzoni, N., de Chabalier, J.-B., & King, G. C. P. (2010). Sequence of rifting in Afar, Manda-Hararo rift, Ethiopia, 2005–2009: Time-space evolution and interactions between dikes from interferometric synthetic aperture radar and static stress change modeling. *Journal of Geophysical Research*, 115, B10413.
- Grandin, R., Socquet, a., Doin, M. P., Jacques, E., De Chabalier, J. B., & King, G. C. P. (2010). Transient rift opening in response to multiple dike injections in the Manda Hararo rift (Afar, Ethiopia) imaged by time-dependent elastic inversion of interferometric synthetic aperture radar data. *Journal of Geophysical Research: Solid Earth*, 115(September 2005).
- Gray, A. L., Mattar, K. E., & Sofko, G. (2000). Influence of ionospheric electron density fluctuations on satellite radar interferometry. *Geophysical Research Letters*, 27(10), 1451–1454.
- Green, R. G., White, R. S., & Greenfield, T. (2014). Motion in the north Iceland volcanic rift zone accommodated by bookshelf faulting. *Nature Geoscience*, 7(1), 29–33.
- Gudmundsson, M. T., Sigmundsson, F., & Björnsson, H. (1997). Ice–volcano interaction of the 1996

- Gjálp subglacial eruption, Vatnajökull, Iceland. *Nature*, 389(October), 954–957.
- Gudmundsson, M. T., Jónsdóttir, K., Hooper, A., Holohan, E. P., Halldórsson, S. A., Ófeigsson, B. G., et al. (2016). Gradual caldera collapse at Bárðarbunga volcano, Iceland, regulated by lateral magma outflow. *Science*, 353(6296), aaf8988.
- Hamling, I. J., Ayele, A., Bennati, L., Calais, E., Ebinger, C. J., Keir, D., et al. (2009). Geodetic observations of the ongoing Dabbahu rifting episode: new dyke intrusions in 2006 and 2007. *Geophysical Journal International*, 178, 989–1003.
- Hamling, I. J., Wright, T. J., Calais, E., Bennati, L., & Lewi, E. (2010). Stress transfer between thirteen successive dyke intrusions in Ethiopia. *Nature Geoscience*, 3(10), 806–806.
- Hamling, I. J., Wright, T. J., Calais, E., Lewi, E., & Fukahata, Y. (2014). InSAR observations of post-rifting deformation around the Dabbahu rift segment, Afar, Ethiopia. *Geophysical Journal International*, 197(1), 33–49.
- Hammond, J. O. S., Kendall, J.-M., Stuart, G. W., Keir, D., Ebinger, C., Ayele, A., & Belachew, M. (2011). The nature of the crust beneath the Afar triple junction: Evidence from receiver functions. *Geochemistry, Geophysics, Geosystems*, 12(12), n/a-n/a.
- Hanssen, R. F., Feijt, A. J., & Klees, R. (2001). Comparison of precipitable water vapor observations by spaceborne radar interferometry and meteorological 6.7- μm radiometry. *Journal of Atmospheric and Oceanic Technology*, 18(5), 756–764.
- Heimisson, E. R., Hooper, A., & Sigmundsson, F. (2015). Forecasting the path of a laterally propagating dike. *Journal of Geophysical Research: Solid Earth*, 120(12), 8774–8792.
- Himematsu, Y., & Furuya, M. (2015). Aseismic strike–slip associated with the 2007 dike intrusion episode in Tanzania. *Tectonophysics*, 656, 52–60.
- Hjartardóttir, Á. R., Einarsson, P., Gudmundsson, M. T., & Högnadóttir, T. (2015). Fracture movements and graben subsidence during the 2014 Bárðarbunga dike intrusion in Iceland. *Journal of Volcanology and Geothermal Research*, 310, 242–252.
- Hooper, A., Zebker, H., Segall, P., & Kampes, B. (2004). A new method for measuring deformation on volcanoes and other natural terrains using InSAR persistent scatterers. *Geophysical Research Letters*, 31(23), 1–5.
- Ikeda, M., Toda, S., Kobayashi, S., Ohno, Y., Nishizaka, N., & Ohno, I. (2009). Tectonic model and fault segmentation of the Median Tectonic Line active fault system on Shikoku, Japan. *Tectonics*, 28(5), 1–22.
- Iken, A., & Bindenschadler, R. A. (1986). Combined measurements of subglacial water pressure and surface velocity of Findelengletscher, Switzerland: conclusions about drainage system and sliding mechanism. *Journal of Glaciology*, 32(110), 101–119.
- Intrieri, E., Di Traglia, F., Del Ventisette, C., Gigli, G., Mugnai, F., Luzi, G., & Casagli, N. (2013). Flank instability of Stromboli volcano (Aeolian Islands, Southern Italy): Integration of GB-InSAR and

-
- geomorphological observations. *Geomorphology*, 201(October 2012), 60–69.
- Jonsson, S., Zebker, H., Segall, P., & Amelung, F. (2002). Fault Slip Distribution of the 1999 Mw7.1 Hector Mine, California, Earthquake, Estimated from Satellite Radar and GPS Measurements. *Bulletin of the Seismological Society of America*, 92, 1377–1389.
- Jonsson, S., Segall, P., Pedersen, R., & Björnsson, G. (2003). Post-earthquake ground movements correlated to pore-pressure transients. *Nature*, 424, 179–183.
- Julian, B. R., Miller, A. D., & Foulger, G. R. (1998). Non-double-couple earthquakes 1. Theory. *Reviews of Geophysics*.
- Jung, H., Won, J., & Kim, S. (2009). An Improvement of the Performance of Multiple-Aperture SAR Interferometry (MAI). *IEEE Transactions on Geoscience and Remote Sensing*, 47(8), 2859–2869.
- Kato, A., Nakamura, K., & Hiyama, Y. (2016). The 2016 Kumamoto earthquake sequence. *Proceedings of the Japan Academy, Series B*, 92(8), 358–371.
- King, G. C. P., Stein, S., & Lin, J. (1994). Static Stress Changes and the Triggering of Earthquakes. *Bulletin of the Seismological Society of America*, 84(3), 935–953.
- Kinoshita, Y., Shimada, M., & Furuya, M. (2013). InSAR observation and numerical modeling of the water vapor signal during a heavy rain: A case study of the 2008 Seino event, central Japan. *Geophysical Research Letters*, 40(17), 4740–4744.
- Kobayashi, T., Takada, Y., Furuya, M., & Murakami, M. (2009). Locations and types of ruptures involved in the 2008 Sichuan earthquake inferred from SAR image matching. *Geophysical Research Letters*, 36(7), 1–5.
- Koptev, A., Calais, E., Burov, E., Leroy, S., & Gerya, T. (2015). Dual continental rift systems generated by plume–lithosphere interaction. *Nature Geoscience*, 8, 1–5.
- Kreemer, C., Holt, W. E., & Haines, a. J. (2003). An integrated global model of present-day plate motions and plate boundary deformation. *Geophysical Journal International*, 154(1), 8–34.
- Li, F. K., & Goldstein, R. M. (1990). Studies of Multibaseline Spaceborne Interferometric Synthetic Aperture Radars. *IEEE Transactions on Geoscience and Remote Sensing*, 28(1), 88–97.
- Li, Z. W., Xu, W. B., Feng, G. C., Hu, J., Wang, C. C., Ding, X. L., & Zhu, J. J. (2012). Correcting atmospheric effects on InSAR with MERIS water vapour data and elevation-dependent interpolation model. *Geophysical Journal International*, 189(2), 898–910.
- Lohman, R. B., & McGuire, J. J. (2007). Earthquake swarms driven by aseismic creep in the Salton Trough, California. *Journal of Geophysical Research*, 112(B4), B04405.
- Maeda, J., & Heki, K. (2014). Two-dimensional observations of midlatitude sporadic e irregularities with a dense GPS array in Japan. *Radio Science*, 49(1), 28–35.
- Maeda, J., Suzuki, T., Furuya, M., & Heki, K. (2016). Imaging the midlatitude sporadic E plasma patches with a coordinated observation of spaceborne InSAR and GPS total electron content. *Geophysical Research Letters*, 43(4), 1419–1425.

- Maerten, F., Resor, P., Pollard, D., & Maerten, L. (2005). Inverting for Slip on Three-Dimensional Fault Surfaces Using Angular Dislocations. *Bulletin of the Seismological Society of America*, 95(5), 1654–1665.
- Magnússon, E., Björnsson, H., Dall, J., & Pálsson, F. (2005). Volume changes of Vatnajökull ice cap, Iceland, due to surface mass balance, ice flow, and subglacial melting at geothermal areas. *Geophysical Research Letters*, 32(5), 1–4.
- Magnússon, E., Rott, H., Björnsson, H., & Pálsson, F. (2007). The impact of jökulhlaups on basal sliding observed by SAR interferometry on Vatnajökull, Iceland. *Journal of Glaciology*, 53(181), 232–240.
- Mandl, G. (1987). Tectonic deformation by rotating parallel faults: the “bookshelf” mechanism. *Tectonophysics*, 141, 277–316.
- Massonnet, D., & Feigl, K. L. (1998). Radar interferometry and its application to changes in the Earth’s surface. *Reviews of Geophysics*, 36, 441–500.
- Matsumoto Y. (1979). Some problems on volcanic activities and depression structures in Kyushu, Japan. The Memoir of the Geological Society of Japan, 16, 127-139 (in Japanese with English abstract)
- McKenzie, D., Davies, D., & Molnar, P. (1970). Plate tectonics of the Red Sea and East Africa. *Nature*, 226, 243–248.
- Meade, B. J. (2007). Algorithms for the calculation of exact displacements, strains, and stresses for triangular dislocation elements in a uniform elastic half space. *Computers & Geosciences*, 33(8), 1064–1075.
- Meyer, F. J. (2011). Performance requirements for ionospheric correction of low-frequency SAR data. *IEEE Transactions on Geoscience and Remote Sensing*, 49(10 PART 1), 3694–3702.
- Michel, R., Avouac, J. P., & Taboury, J. (1999). Measuring ground displacement from SAR amplitude images: application to the Landers earthquake. *Geophysical Research Letters*, 26(7), 875–878.
- Moore, J. D. P., Yu, H., Tang, C. H., Wang, T., Barbot, S., Peng, D., et al. (2017). Imaging the distribution of transient viscosity after the 2016 Mw7.1 Kumamoto earthquake. *Science*, 356(6334), 163–167.
- Moustafa, A. (2002). Controls on the geometry of transfer zones in the Suez rift and northwest Red Sea: Implications for the structural geometry of rift systems. *AAPG Bulletin*, 6(6), 979–1002.
- Nishimura, S., & Hashimoto, M. (2006). A model with rigid rotations and slip deficits for the GPS-derived velocity field in Southwest Japan. *Tectonophysics*, 421(3–4), 187–207.
- Nobile, A., Pagli, C., Keir, D., Wright, T. J., Ayele, A., Ruch, J., & Acocella, V. (2012). Dike-fault interaction during the 2004 Dallol intrusion at the northern edge of the Erta Ale Ridge (Afar, Ethiopia). *Geophysical Research Letters*, 39(19).
- Okada, Y. (1985). Surface deformation due to shear and tensile faults in a half-space. *Bulletin of the Seismological Society of America*, 75(4), 1135–1154.
- Okada, Y. (1992). Internal deformation due to shear and tensile faults in a half-space. *Bulletin of the*

Seismological Society of America, 82(2), 1018–1040.

- Okubo, Y., Shibuya, A. (1993). Thermal and crustal structure of the Aso volcano and surrounding regions constrained by gravity and magnetic data, Japan. *Journal of Volcanology and Geothermal Research*, 55, 337-350.
- Ozawa, S., Murakami, M., Fujiwara, S., & Tobita, M. (1997). Synthetic aperture radar interferogram of the 1995 Kobe earthquake and its geodetic inversion. *Geophysical Research Letters*, 24(18), 2327–2330.
- Pagli, C., Wang, H., Wright, T. J., Calais, E., & Lewi, E. (2014). Current plate boundary deformation of the Afar rift from a 3D velocity field inversion of InSAR and GPS. *Journal of Geophysical Research: Solid Earth*.
- Paquet, F., Dauteuil, O., Hallot, E., & Moreau, F. (2007). Tectonics and magma dynamics coupling in a dyke swarm of Iceland. *Journal of Structural Geology*, 29(9), 1477–1493.
- Parks, M. M., Heimisson, E. R., Sigmundsson, F., Hooper, A., Vogfjörð, K. S., Árnadóttir, T., et al. (2017). Evolution of deformation and stress changes during the caldera collapse and dyking at Bárðarbunga, 2014–2015: Implication for triggering of seismicity at nearby Tungnafellsjökull volcano. *Earth and Planetary Science Letters*, 462, 212–223.
- Pedersen, G. B. M., Höskuldsson, A., Dürig, T., Thordarson, T., Jónsdóttir, I., Riishuus, M. S., et al. (2017). Lava field evolution and emplacement dynamics of the 2014–2015 basaltic fissure eruption at Holuhraun, Iceland. *Journal of Volcanology and Geothermal Research*, 340, 155–169.
- Pollitz, F. F., Kobayashi, T., Yarai, H., Shibazaki, B., & Matsumoto, T. (2017). Viscoelastic lower crust and mantle relaxation following the 14–16 April 2016 Kumamoto, Japan, earthquake sequence. *Geophysical Research Letters*, 44(17), 8795–8803.
- Reynolds, H. I., Gudmundsson, M. T., Högnadóttir, T., Magnússon, E., & Pálsson, F. (2017). Subglacial volcanic activity above a lateral dyke path during the 2014–2015 Bárðarbunga-Holuhraun rifting episode, Iceland. *Bulletin of Volcanology*, 79(6), 1–13.
- Riel, B., Milillo, P., Simons, M., Lundgren, P., Kanamori, H., & Samsonov, S. (2015). The collapse of Bárðarbunga caldera, Iceland. *Geophysical Journal International*, 202, 446–453.
- Rignot, E., Echelmeyer, K., & Krabill, W. B. (2001). Penetration depth of interferometric synthetic aperture radar signals in snow and ice. *Geophysical Research Letters*, 28(18), 3501–3504.
- Rosen, P. A., Hensley, S., & Chen, C. (2010). Measurement and mitigation of the ionosphere in L-band Interferometric SAR data. *IEEE National Radar Conference - Proceedings*, 1459–1463.
- Rossi, C., Minet, C., Fritz, T., Eineder, M., & Bamler, R. (2016). Temporal monitoring of subglacial volcanoes with TanDEM-X - Application to the 2014-2015 eruption within the Bárðarbunga volcanic system, Iceland. *Remote Sensing of Environment*, 181, 186–197.
<https://doi.org/10.1016/j.rse.2016.04.003>
- Ruch, J., Wang, T., Xu, W., Hensch, M., & Jónsson, S. (2016). Oblique rift opening revealed by

- reoccurring magma injection in central Iceland. *Nature Communications*, 7, 12352.
- Ruina, A. (1983). Slip instability and state variable friction laws. *Journal of Geophysical Research*, 88(B12), 10359.
- Sandwell, D. T., Myer, D., Mellors, R., Shimada, M., Brooks, B., & Foster, J. (2008). Accuracy and resolution of ALOS interferometry: Vector deformation maps of the father's day intrusion at Kilauea. *IEEE Transactions on Geoscience and Remote Sensing*, 46(11), 3524–3534.
- Sansosti, E., Berardino, P., Manunta, M., Serafino, F., & Fornaro, G. (2006). Geometrical SAR image registration. *IEEE Transactions on Geoscience and Remote Sensing*, 44(10), 2861–2870.
- Saria, E., Calais, E., Stamps, D. S., Delvaux, D., & Hartnady, C. J. H. (2014). Present-day kinematics of the East African Rift. *Journal of Geophysical Research: Solid Earth*, 3584–3600.
- Schmidt, D. A., & Bürgmann, R. (2003). Time-dependent land uplift and subsidence in the Santa Clara valley, California, from a large interferometric synthetic aperture radar data set. *Journal of Geophysical Research: Solid Earth*, 108(B9), 1–13.
- Scholz, C. H., & Contreras, J. C. (1998). Mechanics of continental rift architecture. *Geology*, 26(11), 967–970.
- Serafino, F. (2006). SAR Image Coregistration Based on Isolated Point Scatterers. *IEEE Geoscience and Remote Sensing Letters*, 3(3), 354–358.
- Sigmundsson, F., Hooper, A., Hreinsdóttir, S., Vogfjörð, K. S., Ófeigsson, B. G., Heimisson, E. R., et al. (2015). Segmented lateral dyke growth in a rifting event at Bárðarbunga volcanic system, Iceland. *Nature*, 517.
- Simons, M., Fialko, Y., & Rivera, L. (2002). Coseismic deformation from the 1999 Mw 7.1 Hector Mine, California, earthquake as inferred from InSAR and GPS observations. *Bulletin of the Seismological Society of America*, 92(4), 1390–1402.
- Sleep, N. H. (1997). Lateral flow and ponding of starting plume material. *Journal of Geophysical Research-Solid Earth*, 102(B5), 10001–10012.
- Spaans, K., & Hooper, A. (2018). Insights Into the Stress Field Around Bárðarbunga Volcano From the 2014/2015 Holuhraun Rifting Event. *Journal of Geophysical Research: Solid Earth*.
- Stamps, D. S., Calais, E., Saria, E., Hartnady, C., Nocquet, J.-M., Ebinger, C. J., & Fernandes, R. M. (2008). A kinematic model for the East African Rift. *Geophysical Research Letters*, 35(5), L05304.
- Strozzi, T., Luckman, A., Murray, T., Wegmüller, U., & Werner, C. L. (2002). Glacier motion estimation using SAR offset-tracking procedures - White Rose Research Online. *IEEE Transactions on Geoscience and Remote Sensing*, 40(11), 2384–2391.
- Tada, T. (1984). Spreading of the Okinawa trough and its relation to the crustal deformation in Kyushu. *Jishin*, 37, 407-415. (in Japanese with English abstract)
- Tada, T. (1985). Spreading of the Okinawa trough and its relation to the crustal deformation in Kyushu (2). *Jishin*, 38, 1-15. (in Japanese with English abstract)

-
- Tada, T. (1993). Crustal deformation in central Kyushu, Japan and its tectonic implication—rifting and spreading of Beppu Shimabara Graben. *The Memoir of the Geological Society of Japan*, 41, 1-12. (in Japanese with English abstract)
- Takada, Y., & Fukushima, Y. (2013). Volcanic subsidence triggered by the 2011 Tohoku earthquake in Japan. *Nature Geoscience*, 6(8), 637–641.
- Takada, Y., & Furuya, M. (2010). Aseismic slip during the 1996 earthquake swarm in and around the Onikobe geothermal area, NE Japan. *Earth and Planetary Science Letters*, 290(3–4), 302–310.
- Takada, Y., Kobayashi, T., Furuya, M., & Murakami, M. (2009). Coseismic displacement due to the 2008 Iwate-Miyagi Nairiku earthquake detected by ALOS / PALSAR : preliminary results. *Natural History*, 9–12.
- Tapponnier, P., & Courtillot, V. (1990). Bookshelf faulting and horizontal block rotations between overlapping rifts in southern Afar. *Geophysical Research Letters*, 17(1), 1–4.
- Tarchi, D., Rudolf, H., Luzi, G., Chiarantini, L., Coppo, P., & Sieber, A. J. (1999). SAR interferometry for structural changes detection: a demonstration test on a dam. *IEEE 1999 International Geoscience and Remote Sensing Symposium. IGARSS'99 (Cat. No.99CH36293)*, 3, 1522–1524.
- Tesfaye, S., Rowan, M. G., Mueller, K., Trudgill, B. D., & Harding, D. J. (2008). Relay and accommodation zones in the Dobe and Hanle grabens, central Afar, Ethiopia and Djibouti. *Journal of the Geological Society*, 165(2), 535–547.
- Tobita, M., Murakami, M., Nakagawa, H., Yurai, H., Fujiwara, S., & Rosen, P. A. (2001). 3-D surface deformation of the 2000 Usu Eruption measured by matching of SAR images. *Geophysical Research Letters*, 28(22), 4291–4294.
- Toda, S., & Stein, R. (2002). Response of the San Andreas fault to the 1983 Coalinga-Nuñez earthquakes: An application of interaction-based probabilities for Parkfield. *Journal of Geophysical Research: Solid Earth*, 107.
- Toda, S., Stein, R. S., & Sagiya, T. (2002). Evidence from the AD 2000 Izu islands earthquake swarm that stressing rate governs seismicity. *Nature*, 419(6902), 58–61.
- Tsai, V. C., Rice, J. R., & Fahnstock, M. (2008). Possible mechanisms for glacial earthquakes. *Journal of Geophysical Research: Earth Surface*, 113(3), 1–17.
- Tsugawa, T., Saito, A., & Otsuka, Y. (2004). A statistical study of large-scale traveling ionospheric disturbances using the GPS network in Japan. *Journal of Geophysical Research: Space Physics*, 109(A6), 1–11.
- Urbani, S., Acocella, V., Rivalta, E., & Corbi, F. (2017). Propagation and arrest of dikes under topography: Models applied to the 2014 Bardarbunga (Iceland) rifting event. *Geophysical Research Letters*, 44(13), 6692–6701.
- Vidale, J. E., & Shearer, P. M. (2006). A survey of 71 earthquake bursts across southern California: Exploring the role of pore fluid pressure fluctuations and aseismic slip as drivers. *Journal of*

- Geophysical Research: Solid Earth*, 111(5), 1–12.
- Watanabe, K., Momikura, Y., Tsuruta, K. (1979). Active faults and parasitic eruption centers on the west flank of Aso caldera, Japan. *Quaternary Research*, 18, 89-101. (in Japanese with English abstract)
- Wegmüller, U., & Werner, C. L. (1997). Gamma SAR processor and interferometry software. *Proc. of the 3rd ERS Symposium, European Space Agency Special Publication*, (ESA SP-414), 1687–1692.
- Wicks, C., Thelen, W., Weaver, C., Gomberg, J., Rohay, A., & Bodin, P. (2011). InSAR observations of aseismic slip associated with an earthquake swarm in the Columbia River flood basalts. *Journal of Geophysical Research*, 116, B12304.
- Wright, T. J., Lu, Z., & Wicks, C. (2003). Source model for the Mw 6.7, 23 October 2002, Nenana Mountain Earthquake (Alaska) from InSAR. *Geophysical Research Letters*, 30(18), 30–33.
- Wright, T. J., Parsons, B. E., & Lu, Z. (2004). Toward mapping surface deformation in three dimensions using InSAR. *Geophysical Research Letters*, 31(1). <https://doi.org/10.1029/2003GL018827>
- Wright, T. J., Ebinger, C., Biggs, J., Ayele, A., Yirgu, G., Keir, D., & Stork, A. (2006). Magma-maintained rift segmentation at continental rupture in the 2005 Afar dyking episode. *Nature*, 442(7100), 291–294.
- Wright, T. J., Sigmundsson, F., Pagli, C., Belachew, M., Hamling, I. J., Brandsdóttir, B., et al. (2012). Geophysical constraints on the dynamics of spreading centres from rifting episodes on land. *Nature Geoscience*, 5(4), 242–250.
- Xu, S., Ángel Francisco, N.-S., Susana, A. A.-Á., & Luis, M. C.-M. (2011). Structural analysis of a relay ramp in the Querétaro graben, central Mexico: Implications for relay ramp development. *Revista Mexicana de Ciencias Geológicas*, 28(2), 275–289.
- De Zan, F. (2014). Accuracy of incoherent speckle tracking for circular gaussian signals. *IEEE Geoscience and Remote Sensing Letters*, 11(1), 264–267.
- Zebker, H. A., & Villasenor, J. (1992). Decorrelation in interferometric radar echoes. *IEEE Transactions on Geoscience and Remote Sensing*, 30(5), 950–959. <https://doi.org/10.1109/36.175330>
- Zebker, H. A., Rosen, P., Hensley, S., & Mouginiis-Mark, P. J. (1996). Analysis of active lava flows on Kilauea volcano, Hawaii, using SIR-C radar correlation measurements. *Geology*, 24(6), 495–498.
- Zebker, H. A., Rosen, P. A., & Hensley, S. (1997). Atmospheric effects in interferometric synthetic aperture radar surface deformation and topographic maps. *Journal of Geophysical Research: Solid Earth*, 102(B4), 7547–7563.

Appendix A. SAR Dataset in Chapter 5

Satellite	Track	Date	Purpose	Spatial resolution [m (Range, Az.)]
COSMO-SkyMed	2631 (A)	28 Jun. 2014	a, b	1.0, 2.3
		30 Jul. 2014	a, b	
		12 Sep. 2014	a, b	
		18 Oct. 2014	b	
		22 Oct. 2014	b	
	2761(A)	11 Aug. 2014	c	1.0, 2.3
		27 Aug. 2014	c	
		28 Aug. 2014	c	
		31 Aug. 2014	c	
		12 Sep. 2014	c	
		13 Sep. 2014	c	
		16 Sep. 2014	c	
		2 Oct. 2014	c	
		6 Oct. 2014	c	
		14 Oct. 2014	c	
		16 Oct. 2014	c	
		18 Oct. 2014	c	
		2632 (D)	26 Jun. 2014	
	28 Jul. 2014		a, b, d	
	13 Aug. 2014		a, b	
12 Sep. 2014	a, b			
23 Sep. 2014	a, b			
30 Sep. 2014	b			
6 Mar. 2015	d			
2762(D)	10 Aug. 2014	c	1.0, 2.1	
	26 Aug. 2014	c		
	30 Aug. 2014	c		
	15 Sep. 2014	c		
	5 Oct. 2014	c		

		13 Oct. 2014	c	
		14 Oct. 2014	c	
		17 Oct. 2014	c	
		21 Oct. 2014	c	
<hr/>				
TerraSAR-X	147 (A)	26 Jul. 2012	a, b	1.0, 1.7
		4 Sep. 2014	a, b	
		20 Nov. 2014	a, b	
<hr/>				
RADARSAT-2	81 (A)	8 Jul. 2014	a	4.7, 5.2
		1 Aug. 2014	a	
		18 Sep. 2014	a	
	181 (A)	21 Jun. 2014	a	4.7, 5.2
		8 Aug. 2014	a	
		1 Sep. 2014	a	
<hr/>				
Sentinel-1A	147 (A)	7 Jan. 2015	b	2.3, 13.9
		31 Jan. 2015	b	
		12 Feb. 2015	b	
		20 Mar. 2015	b	
		1 Apr. 2015	b	
		25 Apr. 2015	b	
		7 May 2015	b	
		19 May 2015	b	
		12 Jun. 2015	b	
		24 Jun. 2015	b	
		6 Jul. 2015	b	
		18 Jul. 2015	b	
		30 Jul. 2015	b	
		23 Aug. 2015	b	
		16 Sep. 2015	b	
		28 Sep. 2015	b	
		10 Oct. 2015	b	
		22 Oct. 2015	b	
		3 Nov. 2015	b	

	27 Nov. 2015	b	
	9 Dec. 2015	b	
	21 Dec. 2015	b	
	14 Jan. 2016	b	
	7 Feb. 2016	b	
	2 Mar. 2016	b	
	26 Mar. 2016	b	
	19 Apr. 2016	b	
	1 May 2016	b	
	6 Jun. 2016	b	
	30 Jun. 2016	b	
	12 Jul. 2016	b	
	24 Jul. 2016	b	
	17 Aug. 2016	b	
	5 Aug. 2016	b	
	17 Aug. 2016	b	
	29 Aug. 2016	b	
	4 Oct. 2016	b	
	28 Oct. 2016	b	
	21 Nov. 2016	b	
	15 Dec. 2016	b	
	8 Jan. 2017	b	
	1 Feb. 2017	b	
111(D)	18 Nov. 2014	b	2.3, 13.9
	30 Nov. 2014	b	
	24 Dec. 2014	b	
	5 Jan. 2015	b	
	17 Jan. 2015	b	
	10 Feb. 2015	b	
	22 Feb. 2015	b	
	6 Mar. 2015	b	
	18 Mar. 2015	b	
	30 Mar. 2015	b	
	11 Apr. 2015	b	
	23 Apr. 2015	b	

5 May 2015	b
17 May 2015	b
29 May 2015	b
10 Jun. 2015	b
22 Jun. 2015	b
4 Jul. 2015	b
16 Jul. 2015	b
9 Aug. 2015	b
21 Aug. 2015	b
14 Sep. 2015	b
26 Sep. 2015	b
8 Oct. 2015	b
1 Nov. 2015	b
13 Nov. 2015	b
31 Dec. 2015	b
24 Jan. 2016	b
5 Feb. 2016	b
29 Feb. 2016	b
24 Mar. 2016	b
5 Apr. 2016	b
23 May 2016	b
4 Jun. 2016	b
28 Jun. 2016	b
22 Jul. 2016	b
3 Aug. 2016	b
27 Aug. 2016	b
20 Sep. 2016	b
2 Oct. 2016	b
26 Oct. 2016	b
1 Dec. 2016	b
13 Dec. 2016	b
25 Dec. 2016	b
18 Jan. 2017	b

PALSAR-2	4_1290	28 Aug. 2014	a	4.3, 3.2
		11 Sep. 2014	a	

2_1300	24 Nov. 2014	e	4.3, 3.2
	2 Feb. 2015	e	
	6 Jul. 2015	e	
	14 Sep. 2015	e	
	23 Nov. 2015	e	
	1 Feb. 2016	e	
	4 Jul. 2016	e	
	21 Nov. 2016	e	
	3 Jul. 2017	e	
	11 Sep. 2017	e	
113_2300	8 Apr. 2015	e	19.0, 25.9
	29 Jul. 2015	e	
	2 Dec. 2015	e	
	24 Feb. 2016	e	
	18 May 2016	e	
	29 Jun. 2016	e	
	13 Jul. 2016	e	
	21 Sep. 2016	e	
	11 Jan. 2017	e	
	17 May 2017	e	
23 Aug. 2017	e		

^a Name of SAR satellite

^b Identification of track number. A: Ascending flight from SSE to NNW, D: Descending flight from NNW to SSE

^c Date of data observation.

^d Purpose of dataset. a) Crustal and icecap surface movement, b) Time-series of icecap surface change, c) Icecap deformation in Figures 5-14 and 5-15 and d) Tracing outline of lava field

^e Spatial resolution of the dataset